

UNIVERSITY OF OKLAHOMA

GRADUATE COLLEGE

FLAME SYNTHESIS OF TUNGSTEN/MOLYBDENUM OXIDE NANOSCALE  
HETEROSTRUCTURES WITH COMPLEX PHYSICAL MORPHOLOGIES

A DISSERTATION

SUBMITTED TO THE GRADUATE FACULTY

in partial fulfillment of the requirements for the

Degree of

DOCTOR OF PHILOSOPHY

By

WALMY CUELLO JIMENEZ

Norman, Oklahoma

2023

FLAME SYNTHESIS OF TUNGSTEN/MOLYBDENUM OXIDE NANOSCALE  
HETEROSTRUCTURES WITH COMPLEX PHYSICAL MORPHOLOGIES

A DISSERTATION APPROVED FOR THE  
SCHOOL OF AEROSPACE AND MECHANICAL ENGINEERING

BY THE COMMITTEE CONSISTING OF

Dr. Wilson Merchan-Merchan, Chair

Dr. Yingtao Liu

Dr. Li Song

Dr. Jivtesh Garg

Dr. Edgar A. O'Rear III

© Copyright by WALMY CUELLO JIMENEZ 2023

All Rights Reserved.

**AUTHORITY REPORT FORM** *for the* **DISSERTATION DEFENSE**

Date Released by Graduate College: **April 11, 2023**

Permission has been given to **Walmy Cuello Jimenez, 112-76-2127** (Aerospace and Mechanical Engineering), to appear for the dissertation defense **no later than April 28, 2023**.

This report, signed by all members of the committee, is due in the Graduate College within **3 working days** of the defense. If the defense is not held during this semester, the graduate liaison or committee chair must notify the Graduate College in writing as to why the defense was not held and this form must be returned marked Not Taken.

We, the committee members listed below, met on 04/19/2023 (Date) to examine the candidate, **Walmy Cuello Jimenez**, for the degree of **Doctor of Philosophy**, and we report the following result:

**SATISFACTORY**

Wilson Merchan-Merchan: Wilson Merchan Merchan

Edgar O Rear: Edgar Allen O'Rear, III, Ph.D.

Jivtesh Garg: Jivtesh Garg

Yingtao Liu: Yingtao Liu

Li Song: Li Song

*Dedicated to my brother Jhon Jairo Florez Jimenez, who sadly passed while I was completing the last chapters of this dissertation. He certainly personalized the quote “The people who are crazy enough to think they can change the world are the ones who do” by relentlessly working and preparing himself to fulfill his dream of creating a better future for those in need. His capacity to bring people together and inspire others was second to none. Thanks ‘manito’ for showing us that those who come from the bottom can also fight to achieve our dreams... we just need to act... the fight continues “Juntos Florecemos”.*

*Dedicado a mi hermano Jhon Jairo Florez Jimenez, quien tristemente falleció mientras completaba los últimos capítulos de esta disertación. Él ciertamente personalizó la cita, (traducida al español) "Las personas que están lo suficientemente locas como para pensar que pueden cambiar el mundo son las que lo logran", trabajando incansablemente y preparándose para cumplir su sueño de crear un futuro mejor para aquellos con necesidades. Su capacidad para unir a la gente e inspirar a otros fue insuperable. Gracias 'manito' por mostrarnos que aquellos que venimos desde abajo también podemos luchar para lograr nuestros sueños... solo necesitamos actuar... la lucha continúa "Juntos Florecemos".*

## ACKNOWLEDGEMENTS

I would like to express my deepest gratitude to my advisor Dr. Wilson Merchan-Merchan, who since I was an undergraduate student gave me the great opportunity of joining his research group, where I attained multiple skills as an academic researcher. I also want to thank Dr. Merchan-Merchan for his invaluable guidance, support, and encouragement throughout my doctoral research. His dedication to my research, commitment to excellence, and passion for scientific inquiry inspired me to strive for excellence in my work with clear attention to details. I am grateful for all the time Dr. Merchan-Merchan dedicated to mentoring me, reviewing my work, and providing constructive feedback that shaped my approach to research, technical writing and presentations. His steadfast support and encouragement gave me the confidence to pursue this program to pose and solve challenging research questions. Finally, I would like to express my gratitude to Dr. Merchan-Merchan for being an exceptional mentor, role model, and friend. Thanks a lot for everything.

I would like to extend special acknowledgement to Dr. A.V. Saveliev for his invaluable contributions to this collaborative study. His insightful discussions on the multiple approaches we evaluated helped shape the direction of several challenges we faced during the process.

I would also like to extend special thanks to Dr. Alan Nicholls from the UIC Research Resource Center for assistance in TEM studies and helpful discussions. Moreover, I would also like to express my sincere appreciation to Dr. Preston Larson and Dr. Scott Russell from the Samuel Roberts Noble Electron Microscopy Laboratory at the University of Oklahoma for their help with SEM evaluation and discussions thereof.

I would like to express my sincere appreciation to the members of my PhD committee for their invaluable guidance, support, and feedback throughout my doctoral research. They provided me with a wide range of expertise and perspectives, which enriched my research and contributed significantly to its quality. Furthermore, I am very thankful to the faculty members and the staff of the University of Oklahoma for their advices and support throughout my PhD program.

I would like to express my sincere gratitude to the Capstone Undergraduate Group, consisting of Nate A. McMillen, Hamza M. Jawabreh, and Mark A. Thul, for their hard work and collaboration on the development of smart window applications using TMO nanostructures. I would also like to express my gratitude to Mr. Billy Mays and Mr. Greg Williams from the AME Machine Shop for their invaluable support in building the experimental set up.

Finally, I would like to express my heartfelt appreciation to my family for their unwavering love, support, and encouragement throughout my different endeavors. They have been my constant source of inspiration, motivation, and guidance. Their belief in my abilities, their encouragement during difficult times, and their unwavering support have given me the strength and determination to pursue my academic and professional goals.

# TABLE OF CONTENT

ACKNOWLEDGEMENTS .....	vi
TABLE OF CONTENT .....	viii
LIST OF TABLES .....	xi
LIST OF FIGURES .....	xii
ABSTRACT .....	xvi
PREFACE .....	xxi
1. CHAPTER 1: INTRODUCTION TO TRANSITION METAL OXIDES (TMOs) ...	1
1.1 Motivation to Study TMOs .....	1
1.2 Properties and Applications of 1D and 3D TMO Nanostructures.....	4
1.2.1 Solar Panels.....	5
1.2.2 Electrochromic (EC) Devices .....	7
1.2.3 Lithium-ion Batteries (LIBs) .....	9
1.2.4 Capacitors .....	10
1.2.5 Gas Sensors.....	10
1.2.5.1 <i>Chemical Composition:</i> .....	11
1.2.5.2 <i>Physical Morphological Properties:</i> .....	12
1.2.6 Light Emitting Diodes.....	13
1.2.7 Catalysis.....	14
1.3 Outline/Organization of the Dissertation .....	16
2. CHAPTER 2—LITERATURE REVIEW .....	18
2.1 Synthesis and Methodologies to Form TMO Nanostructures: A Review and Analysis of Flame and Non-flame Synthesis Techniques.....	19
2.1.1 Chemical vapor deposition (CVD) .....	20
2.1.2 Sol-gel.....	21
2.1.3 Plasma.....	22
2.1.4 Flames.....	23
2.2 Flames as a Unique Fabrication Techniques to Produce TMO Nanoparticles.....	28
2.2.1 Flame synthesis of metal-oxide nanoparticles .....	28
2.2.1.1 <i>“Aerosol” and “spray pyrolysis” methods</i> .....	28
2.2.1.2 <i>Approaches used for controlled synthesis in “aerosol” and “FSP”</i> .....	31
2.2.2 Flame synthesis of multi-dimensional TMOs using the “Solid Support” method.....	35
2.2.3 Volumetric flame synthesis of 1D and 3D TMOs .....	40
2.2.3.1 <i>TMOs (1D) formed using “aerosol” and “spray pyrolysis”</i> .....	40
2.2.3.2 <i>Gas-phase flame synthesis of 1D and 3D TMOs</i> .....	42
2.3 Core-shell and Mixed Transition Metal Oxide Nanostructures (MTMOs).....	43
2.3.1 Flame synthesis of core-shell and MTMOs on solid substrates .....	45
2.3.2 Synthesis of MTMOs and related core-shell nanostructures using “flame spray pyrolysis” .....	47



2.3.3	Gas-phase synthesis of MTMOs.....	50
3.	CHAPTER 3—RESEARCH OBJECTIVES.....	51
3.1	Thesis Objectives .....	51
3.2	Research Impact .....	53
4.	CHAPTER 4—EXPERIMENTAL SETUP AND PROCEDURE.....	55
4.1	Experimental Setup of the Counterflow Reactor .....	55
4.1.1	Counter-flow reactor positioning system.....	58
4.2	Counter-flow Diffusion Flame Structure .....	59
4.2.1	Structural response of counter-flow diffusion flame to strain rate modifications.....	60
4.2.2	Structural response of counter-flow diffusion flame to oxygen concentration variations .....	62
4.2.3	Numerical predictions of temperature profile and chemical species distribution .....	66
4.3	Probe Insertion Mechanism into the Flame Environment.....	69
4.4	Sample Preparation and Characterization Techniques.....	70
5.	CHAPTER 5—FLAME SYNTHESIS OF TMOs ON A SINGLE METAL SUPPORT.....	72
5.1	Flame Synthesis of 1D, 2D, 3D and Hybrid Nanostructures .....	73
5.1.1	Characterization of the chemical composition of the 1D, 2D and 3D tungsten-oxide nanostructures .....	78
5.1.2	Synthesis of hybrid tungsten-oxide cores with carbon shells .....	80
5.1.3	Proposed growth mechanism of the 1D, 2D, 3D and hybrid nanostructures.....	82
6.	CHAPTER 6—GAS-PHASE SYNTHESIS OF TMO NANOSTRUCTURES BASED ON A SINGLE SUPPORT .....	89
6.1	Gas-phase Synthesis of TMO Nanoplatelets.....	89
6.2	Growth Mechanism of the TMO Octahedron Nanoplatelets .....	93
7.	CHAPTER 7—FLAME SYNTHESIS OF HYDRID AND COMPLEX TMOs HETEROSTRUCUTURES ON SOLID MULTI-METALS SUPPORT .....	95
7.1	Classes of Heterostructures .....	99
7.2	Flame Synthesis W/Mo-heterostructures of Hybrid and Complex Morphology	101
7.3	Simultaneous Dual-Metal Flame Insertion at Different Flame Zones to Fabricate Nanostructures with Complex Morphologies.....	104
7.3.1	Synthesis of complex nano and micron scaled structures with 30 sec of flame residence time .....	104
7.3.2	Synthesis of complex nano and micron scaled structures with 60 sec of flame residence time .....	106
7.3.3	Synthesis of complex nano and micron scaled structures with 150 sec of flame residence time .....	110
7.4	Variable Dual-Metal Flame Insertion at Different Flame Zones to Fabricate Nano and Micron Scaled Heterostructures .....	112

7.5	Simultaneous Dual-Metal Flame Insertion at the Same Flame Zone to Fabricate Nano and Micron Scaled Heterostructures.....	118
7.6	Characterization of the Formed Structures with Complex Morphologies .....	121
7.7	Growth Mechanism .....	125
8.	CHAPTER 8—CONCLUSIONS .....	129
8.1	Conclusions .....	130
8.2	Recommendations for Future Work.....	135
	REFERENCES .....	137
	APPENDIX.....	156
	Appendix A – Structural and Chemical Characterization of Synthesized Nanostructures by Various Techniques .....	156
A.1	Electron Microscopy .....	156
A.2	Transmission Electron Microscopy (TEM) .....	158
A.3	Scanning Electron Microscopy (SEM) .....	159
A.4	X-ray Photo-Electron Spectroscopy (XPS).....	160
A.5	Selected Area Electron Diffraction (SAED).....	160
	Appendix B – Curriculum Vitae.....	162

## LIST OF TABLES

<b>Table 1.</b> Properties and applications of metal oxides, adapted from [11].	4
<b>Table 2.</b> Methods used for the synthesis of TMOs nanomaterials.	24
<b>Table 3.</b> Flame configurations and generated spheroidal nanoparticles.	33
<b>Table 4.</b> Flame configuration and generated 1D and 3D TMO Nanostructures.	38
<b>Table 5.</b> “Gas-Phase” Burner configurations for flame synthesis of 1D and 3D TMO nanostructures.	41
<b>Table 7.</b> Measured flame geometry by varying the strain rate.	64
<b>Table 8.</b> Measured flame geometry by changing the oxygen content.	66
<b>Table 9.</b> Comparison of light vs. electron microscopes. Adopted from [233].	157

## LIST OF FIGURES

<b>Fig. 1.</b> Typical applications of nanostructures multi-dimensional TMOs: (a) solar panels; (b) electrochromic; (c) rechargeable batteries; (d) capacitors; (e) gas sensors; (f) light emitting diodes; and (g) catalyst. ....	6
<b>Fig. 2.</b> Schematics showing different approaches utilized in the flame synthesis of TMOs. (a) Evolution of metal oxide nanoparticles as the base materials is introduced into a reaction zone using “Aerosol Methods” and “FSP” techniques; (b) “Solid Support” synthesis of 1D/3D TMOs; (b1-b2) “Gas-phase” synthesis of TMOs and hybrid nanomaterials; (c) Synthesis of TMOs by direct oxidation of a TM in a post flame region. ....	27
<b>Fig. 3.</b> Schematic of the experimental facility. The gas flows are measured and regulated by mass flow controllers, then the fuel and oxidizer mixing process takes place in their respective mixing chambers. The fuel mixture is introduced from the top nozzle and the oxidizer mixture is supplied from the bottom nozzle. The photograph represents a regular counter-flow diffusion flame. ....	57
<b>Fig. 4.</b> Schematic of the cross-sectional view of the counter-flow combustion reactor. The inset represents a photograph of the actual combustion reactor and the counter-flow diffusion flame. ....	58
<b>Fig. 5.</b> Schematic of the 2-D stepping motor positioning system. The stepper motors are controlled through the control box by the personal computer. ....	59
<b>Fig. 6.</b> Counter-flow diffusion flame photographs with oxidizer concentration of 35% O <sub>2</sub> + 65% N <sub>2</sub> formed with various strain rates ranging from 10 s <sup>-1</sup> to 30 s <sup>-1</sup> . Increasing strain rates results in reduced flame zone thicknesses. ....	64
<b>Fig. 7.</b> Flame structure response to strain rate variations. Results show that both the characteristics zones of the flame and the flame thickness are reduced with increasing strain rates. ....	65
<b>Fig. 8.</b> Counter-flow diffusion flame photographs with strain rate of 20 s <sup>-1</sup> formed with various oxygen concentrations. As oxygen content is increased, both zones become more active. ....	65
<b>Fig. 9.</b> Flame structure response to oxygen content variations. Results show that blue zone thickness increased by increasing the oxygen content in the oxidizer stream. Conversely, the yellow zone and the overall flame thickness decrease with increasing oxygen content. ....	66
<b>Fig. 10.</b> Temperature and chemical species profiles along the Z axis. The location of the stagnation plane is indicated by the dashed line. Strong temperatures and chemical species gradients are shown in this simulation [227,228,]. ....	68
<b>Fig. 11.</b> Schematic of the TM probes and protective sleeve/flame interaction. Z represents the flame location, which is measured from the fuel nozzle. The fuel and oxidizer stream are also illustrated. ....	70
<b>Fig. 12.</b> Sample preparation methods for both SEM and TEM analyses. ....	71
<b>Fig. 13.</b> Evolution of tungsten-oxide nano-sized structures from 1D to 3D morphologies after a Mo probe is exposed into a counter-flow diffusion flame during 2 minutes process. SEM: (a) schematic of probe size and location within flame media, flame/oxidizer configuration, and deposits location for 1D structures, depicting the location of the fuel and oxidizer sides of the probe; (b) low resolution SEM (LR-SEM) image illustrating a high	

density layer of tungsten-oxide nanowires; (c) high resolution SEM (HR-SEM) image of the boxed area in (b); (d) schematic of probe size and location within flame media, flame/oxidizer configuration, and deposits location for 2D structures; (e) LR-SEM image of the W-probe indicating the deposition takes place on the probe sides; (f) SEM imaging of the boxed area in (e); (g) HR-SEM imaging of the fabricated ribbon-like structures along with the cylindrical 1D nanostructures; (h) schematic of probe size and location within flame media, flame/oxidizer configuration, and deposits location for 3D structures; (i) LR-SEM image of a tungsten-oxide nanostructures cluster; (j) depicts the various hollow and semi hollow large 3D structures (red arrows) along with the high aspect ratio solid cylindrical structures (yellow arrows). Note the boxed areas are not drawn to scale..... 74

**Fig. 14.** Chemical composition characterization of the synthesized 1D to 3D tungsten-oxide nanostructures: (a) LR-TEM image depicting the core-shell morphology of the formed 1D nanorods; (b) HR-TEM illustrating the morphology of the 1D core and shells and their elemental compositions (EDX inserts); (c) higher resolution TEM showing the lattice spacing of the formed 1D structures; (d) typical TEM image of a grown ribbon-like 2D structures; (e) higher resolution image of (d); (f) HR-TEM image of the boxed area in (e); (g) SEM image of the typical 3D structures; (f) XPS spectrum of the large 3D tungsten-oxide nanostructures. Note the boxed/circled areas are not drawn to scale..... 79

**Fig. 15.** TEM images of hybrid nanowires and tungsten-oxide nanorods formed on the surface of the 1 mm W-probe: (a) schematic indicating probe position at  $Z = 12$  mm and the lack of protective shield use; (b) TEM results illustrating the sole presence of tungsten-oxide on the formed 1D nanorods; (c) schematic indicating probe position at  $Z = 12$  mm and the protective shield with internal diameter  $D = 6$  mm; (d) TEM image depicting the tungsten-oxide nanorods covered with a thin layer of carbon shells; (e) schematic indicating probe position at  $Z = 12$  mm and the protective shield with internal diameter  $D = 8$  mm; (f) TEM image revealing the tungsten-oxide nanorods covered with a larger layer of carbon shells; (g) chart representing the C-shells thickness obtained with varying protective shield diameters during prove removal. Diameter of the probe/substrate, the protective shield and the size of the flame structure are not drawn to scale..... 81

**Fig. 16.** Growth mechanism of the synthesized 1D, 2D, 3D, and hybrid nanostructures: (a) schematic diagram of the recorded distribution of deposited materials suggests the transfer of material from the lower to the upper part of the probe,  $T_1 > T_2$ ; (b) SEM image collected on the deposits on the upper part of the probe show the layer to be composed of needle-like 1D nanostructures; (c) SEM image of the bottom surface of the probe depicting strong material erosion; (d) schematic diagram of the recorded distribution of deposited materials suggests the transfer of material from the lower to the sides of the probe,  $T_1 > T_2$ ; (e-f) SEM image of the synthesized 2D flat ribbon structures with the presence of 1D nanorods (e) and inserts depicting the computer generated 2D shapes; (g-j) schematic and SEM images of the 3D formed structures along with computer generated inserts; (k-m) schematic and TEM images of the fabricated tungsten-oxide core and carbon-shells hybrid nanostructures. .... 83

**Fig. 17.** Thermophoretic sampling technique used for collection of the gas-phase fabricated nanostructures. Adapted from [227] ..... 90

**Fig. 18.** Gas-phase synthesis of octahedral and elongated polygonal nanocrystals: (a) flame positions and respective temperature within the flame media; (b) schematic of the formed

structures evolution from tungsten-oxide vapors to well-defined elongated polygonal nanocrystals as structures flow toward the stagnation plane; (c-d) LR- and HR-TEM imaging of the high density discrete shapeless particles collected at  $Z = 13$  mm, where the probe and TEM grid are at placed at the same position in the flame; (e-f) LR- and HR-TEM images of polygonal structures accompanied by smaller discrete shapeless particles collected at the  $Z= 12$  mm; (g-h) LR- and HR-TEM images of high density of nanocrystals of large aspect ratios collected at  $Z= 11$  mm. .... 92

**Fig. 20.** Schematic representations comparing the essential steps needed for the preparation of MTMOs employing: (a) CVD; (b) Sol-Gel; and (c) flame methodologies..... 98

**Fig. 21.** Schematic of multiple configurations of MTMOs or complex heterostructures: (a) mixed compounds; (b) bi-layer films; (c) decorated; (d) core-shell; and (e) branch-like heterostructures. Adapted from [221]. .... 100

**Fig. 22.** (a1) Photograph of the flame formed by the counter-flow reactor (T1 and T2 are temperatures in the carbon- and oxygen-rich sections of the flame, respectively). (a2) schematic of the ceramic sample holder. (b) numerical predictions on temperature profile and major chemical species in the diffusion opposed-flow flame [227]. (c) sketch of the insertion of the metallic probes and the deposition behavior. (d) graphical representation of the deposition locations and nomenclature defined for discussion thereof. (e) Schematic of the morphology of the synthesized structures. .... 103

**Fig. 23.** 1D rod-like ‘backbone’ structures and polyhedral complex nanostructures fabricated after both probes being exposed to a flame residence time of 30sec. The Mo and W probes are introduced in the flame media at  $Z=11$ mm and  $Z=13$ mm, respectively. The metal probes are introduced into the flame simultaneously for a residence time of 30 seconds. (a1) schematic of a single metal probe inserted into the flame media; images collected on the oxidizer side of the Mo (a2) and W (a3) probes when exposed to the flame medium with no additional probe insertion; (b1) schematic of the dual insertion of Mo and W probes into the flame medium at flame positions of  $Z=11$ mm and  $Z=13$ mm, respectively, along with the location of the crystallization sites; (b-c) imaging of the 1D structures deposited at  $90^\circ$ ; and  $45^\circ$  crystallization sites on the Mo probe; (d-e) high density of “backbone” structures deposited at  $0^\circ$  and  $300^\circ$  sites; (f-g) imaging of structures synthesized at crystallization sited located at  $285^\circ$  and  $270^\circ$ . .... 106

**Fig. 24.** Nanotrees-like structures synthesized after both probes being exposed to a flame residence time of 60 sec. (a) schematic of the dual insertion of Mo and W probes into the flame medium at flame positions of  $Z=11$ mm and  $Z=13$ mm, respectively, along with the location of the crystallization sites and location of collected samples of the gas-phase formed crystals; (b1-b5) SEM images illustrating the randomly distributed nanotrees; (c1-c2) randomly oriented tree-like structures with 3D deposits with various facets; (d) high dense nanorod-like structures; (e1-e3) TEM images of tungsten-oxide structures generated in the gas-phase a location (1) depicted in (a); (f1) EDX of deposits at the tips (f2) of the end of the tree-like structures..... 109

**Fig. 25.** Synthesis of polyhedron and forest-like structures after both probes being introduced into the flame volume for a residence time of 150 sec. (a) schematic of the dual insertion of Mo and W probes into the flame medium at flame positions of  $Z=11$ mm and  $Z=13$ mm, respectively, along with the location of the crystallization sites; (b1-b3) SEM images of the polyhedral structures synthesized on the fuel side of the Mo-probe at the  $90^\circ$

site; (c1-c4) SEM images of flower-like complex structures deposited at the 25° crystallization site; (d1-d4) SEM images of the tree- and forest-like complex structures crystallized at the 335° site. .... 112

**Fig. 26.** Synthesis of heterostructures after varying the insertion and residence time of the metal probes. a) schematic of the variable insertion of Mo and W probes into the flame medium at flame positions of Z=11mm and Z=13mm, respectively, along with the location of the crystallization sites; (b1-b3) SEM imaging of the grass-like heterostructures with the Mo probe inserted first in the flame (Z= 11mm) for 90 sec by itself, followed by the introduction of the W probe (Z = 13 mm) for 30 sec while the Mo probe was maintained inside flame region; SEM imaging of the heterostructures formed when the Mo probe inserted first in the flame (Z= 11mm) for 90 sec by itself, followed by the introduction of the W probe (Z = 13 mm) for 60 sec while the Mo probe was maintained inside flame region (c1-c2) SEM imaging of polyhedron structures synthesized at 90° site; (d1-d2) polyhedral heterostructures deposited at the 45° crystallization site; imaging of tree-like structures with high (e1-e4) and low (f1-f3) density of cubical deposits on their 1D rod-like branches; (g) SEM imaging of deformed or irregular polyhedrons suspended on nanorods; and (h1-h5) TEM imaging and EDX elemental mapping of the collected materials. .... 117

**Fig. 27.** Synthesis of the complex and hybrid structures resulted from the single Mo and dual Mo/W probes insertion in the flame at Z = 13 mm.(a) Schematic of the single insertion of the Mo probe in the flame at Z = 13 mm; (a2-a3) SEM images of the rectangular molybdenum-oxide nanostructures resulted from the single insertion of the Mo probe in the flame medium; (b1) photograph of the counter-flow diffusion flame and the location of the Mo and W probes both inserted at Z = 13 mm; (b2) schematic of the dual metal probe insertion in the flame medium at the same location; (c1-c2) SEM images of the formed structures on the Mo probe surface resulted from the dual probe insertion in the flame; and (c3-c4) localized SEM-EDX results thereof; (d1-d2) SEM images of the formed structures on the W probe surface resulted from the dual probe insertion in the flame; and (d3-d4) localized SEM-EDX results thereof. Adapted from [217]. Note boxed area is not drawn to scale. .... 120

**Fig. 28.** TEM images of structures resulted from simultaneously inserted Mo and W probes into the flame media for a duration of 30 (a1-a3), 60 (b1-b3), and 150 sec (c1-c4). And TEM images of structures resulted from Mo and W probes inserted at different times/durations into the flame environment (d1-e5). .... 124

**Fig. 28.** Proposed growth mechanism of the various structures using the “solid support” single step method. (a1-a2) Mo probe inserted by itself in the flame medium; (b1-e3) Mo and W probes introduced simultaneously in the flame medium; (f1-h4) Mo and W probes are introduced in the flame volume at different times. .... 128

## ABSTRACT

The focus of this dissertation is to investigate the synthesis of crystalline transition metal oxide (TMO) structures in a counter-flow diffusion flame. This thesis examines the underlying mechanisms for the flame synthesis of 1D, 2D and 3D nano and micron scaled TMO structures on the solid support and in the flame gas-phase. The understanding of the growth mechanisms of the synthesis of single metal structures, along with hybrid and heterostructures with complex morphologies is essential to tailor the fabrication of TMO nanoscale structures. These new novel structures enable a multiplicity of applications in critical areas of today's world economics such as clean energy and sustainability (i.e. solar energy, batteries, smart buildings, gas sensors, etc.). The source material, solid supports of high purity transition metals, in the form of wires are introduced in the flame medium to trigger the synthesis of crystalline nanostructures. The insertion of single and dual solid supports in the oxygen-enriched diffusion flame is investigated along with the rapid formation of structures in the gas-phase. The solid support serves as, both, the material source and the site for disposition, allowing for crystallization of the formed structures at different locations around the surface of the metal probes. The study presented herein commenced with the fabrication of 1D and 3D tungsten-oxide nanostructures on the surface of a single solid support (i.e. W probe) inserted in the opposed-flow oxy-fuel flame. The unique 1D nature of the counter-flow diffusion flame, along with its high thermal and chemical species gradients favors the transformation of bulk transition metals into 1D, 2D, and 3D structures with complex morphologies. The physico-chemical properties of the transition metal probe (i.e. diameter and elemental composition) and flame composition (i.e. oxygen content in the oxidizer stream) were varied to investigate their influence on



the synthesized nanostructures. We hypothesize that the concentration rate of metal oxide vapors generated from the surface of the probe, once inserted in the oxygen-rich flame medium, along with flame residence time, flame oxidizer composition and precursor location in the flame volume are key parameter for controlling the morphology of the structures. All of the mentioned factors can influence flame temperature and composition of oxygen species, along with the rates of oxide generation, subsequent crystallization and morphologies of the structures formed. Moreover, the unique structure of the 1D flame geometry with one region rich in carbon species and the other in oxygen radicals can be leveraged for the synthesis of even more complex assemblies such as hybrid carbon-metal oxide structures.

The formation of triangular, rectangular, square, and cylindrical 3D channels with completely hollow or semi-hollow morphologies was achieved by varying the probe diameter from 1.0 to 0.5 mm. Whereas the increase of the O<sub>2</sub> content to 100% and the employment of a 1 mm high purity W probe resulted in the growth of 2D ribbon-like micron-sized structures. The lattice spacing of ~0.38 nm measured for the 1D tungsten-oxides closely matches that of monoclinic WO<sub>3</sub> structure. X-ray photoelectron spectroscopy analysis revealed that the larger 3D structures also consist of WO<sub>3</sub>, confirming that the chemical composition of the structures remains the same while tailoring both the probe and flame parameters. The flame geometry was used to synthesize hybrid C-metal oxide structures. This was achieved by inserting a high purity 1 mm diameter W probe into the oxygen rich flame environment (formed with an oxidizer composition of 50% O<sub>2</sub> + 50% N<sub>2</sub>) to form 1D tungsten-oxide structures. The newly formed structures were exposed to the carbon rich environment of the flame, using a sleeve, to coat their

surfaces with various layers of carbon shells, thus, forming 1D hybrid nanowires composed of tungsten-oxide cores covered with a uniform carbon sheath. The physical features of the grown structures on the solid support present lengths up to 50  $\mu\text{m}$  and diameters ranging from 20 to 50 nm. This study reveals the existence of a common generic mechanism consisting of tungsten-oxides/hydroxides layers being formed on the probe surface (fuel side) exposed to the high-temperature oxidative environment. These oxides/hydroxides layers are then evaporated/sublimated as the metal probe continues being exposed to the flame volume. The formed oxide vapors are then transported by the gas flow towards the stagnation plane and crystallizes in the form of 1D nanomaterials on the upper surface of the probe where the temperatures are lower. The proposed growth mechanism for the 3D structures consists of coalescing of 1D tungsten-oxide nanorods. The growth of the 3D channel hollowed structures is favored by material deposition from the gas-phase along the edges of early formed large cubical structures (Berg effect). Thereby, resulting in deposits of hollowed structures since solely a limited amount of materials can diffuse to the heart of the formed 3D structure. Regarding the hybrid nanowires, a two-step synthesis mechanism is proposed: (i) tungsten-oxide nanorods are formed in the oxygen-rich flame region; (ii) the rapid formation of carbon shells from hydrocarbon species attained from the carbon-rich zone of the flame during the probe removal process.

The gas-phase structure/particle synthesis sets the foundation for increase production of tungsten-oxide nanostructures. The synthesis of well-defined faceted octagonal prisms (octahedron nanoplatelets) and elongated structures of high aspect ratio in the form of rod-like nanocrystals is performed in the flame gas-phase employing a solid-fed precursor flame technique using a 99.9% purity 1 mm diameter W probe as the

precursor source. The growth mechanism of the formed nanoscale structures involves the oxidation of the surface of the metallic probe, evaporation of the newly formed oxide layer followed by transport of the metal oxide vapors toward the hydrocarbon-rich zone of the flame. As the transport takes place, the metal oxide vapors are crystallized into well-defined octahedron nanoplatelets and elongated rod-like nanocrystals. The lattice spacing of grown nanoplatelets and of the rod-like nanocrystals was measured to be  $\sim 0.38$  nm closely corresponding to the (002) plane of monoclinic  $\text{WO}_3$  structures.

The last part of this research consisted of studying the impact of dual solid support synthesis to aid the formation of hybrid and complex structures with a multiplicity of morphologies. W and Mo probes of 1 mm in diameter are inserted in an oxygen-rich zone at flame positions of  $Z = 13$  and  $Z = 11$  mm, respectively. Experiments consisted of simultaneous and varied probe insertion in the flame medium. Evidently, controlling flame position (temperature/radicals' concentration), residence time (rate of oxide vapors production), and probe insertion sequence results in the formation of highly complex structures with multiple morphologies (e.g., polyhedral-, tree-, flower-, forest-, and grass-like nanostructures). The growth of these unique structures is driven by the formation of 1D "backbone" structures that serves as precursors for the synthesis of the multiple structures with complex morphologies. HR-TEM/EDX/SAED analyses were used to characterize the formed structures. A proposed growth mechanism for the synthesis of these hybrid complex structures is also presented. It is interesting to note that tungsten-oxide structures with unique morphologies were grown not only on the solid support

surface but also in the flame gas-phase providing insightful knowledge regarding the mass production of these materials with a wider range of applications.

## PREFACE

This dissertation is based on and contained information and data from the published articles below. For which W. Cuello Jimenez is the main contributor:

- W. Merchan-Merchan, **W. Cuello Jimenez**, O. Rodriguez Coria, C. Wallis. Editor(s): Y. Beeran Pottathara, S. Thomas, N. Kalarikkal, et al., “Chapter 7 - Flame Synthesis of Nanostructured Transition Metal Oxides: Trends, Developments, and Recent Advances” In Micro and Nano Technologies, Nanomaterials Synthesis, Elsevier (2019) 201-263, ISBN 9780128157510.
- **W. Cuello Jimenez** and W. Merchan-Merchan, “Flame Synthesis Nanostructures with Complex Morphologies and Hybrid-nature” 11 U.S. National Combustion Meeting, Western States Section of the Combustion Institute, March 24–27, 2019, Pasadena, California.
- W. Merchan-Merchan, A.V. Saveliev, **W. Cuello Jimenez**, and G. Salkar, “Flame synthesis of hybrid nanowires with carbon shells and tungsten oxide cores”, Carbon 48 (2010) 4510-4518 (**Impact Factor = 11.31**).
- W. Merchan-Merchan, A.V. Saveliev, and **W. Cuello Jimenez**, “Solid support flame synthesis of 1-D and 3-D tungsten oxide nanostructures”, Proceedings of the Combustion Institute, 33 (2011) 1899-1908 (**Impact Factor = 6.53**).
- W. Merchan-Merchan, A.V. Saveliev, L. Kennedy and **W. Cuello Jimenez** “Combustion synthesis of carbon nanotubes and related nanostructures”, Progress in Energy and Combustion Science 36 (2010) 696-727 (**Impact Factor = 35.34**).
- W. Merchan-Merchan, A.V. Saveliev, and **W. Cuello Jimenez** “Novel flame-gradient method for synthesis of metal-oxide channels, nanowires and nanorods”, Journal of Experimental Nanoscience 5 (2010) 199-212 (**Impact Factor = 2.024**).
- W. Merchan-Merchan, A.V. Saveliev, and **W. Cuello Jimenez** “Solid support flame synthesis of 1-D and 3-D tungsten oxide nanostructures”, 33rd International Symposium on Combustion, August 1-6, 2010, Beijing, China.
- W. Merchan-Merchan, A.V. Saveliev, and **W. Cuello Jimenez**, “Counter-Flow Diffusion Flame Synthesis of Polygonal and Ribbons-Like Tungsten Oxide

Nanostructures”, 55th Annual Pentasectional Meeting of ACS, April 10- 2010, Norman, OK.

- W. Merchan-Merchan, **W. Cuello Jimenez**, and A.V. Saveliev, “Synthesis of 1-D and 3-D tungsten-oxide nanostructures on solid supports in an opposed flow oxy-fuel flame”, , CSSCI 2010 Technical Meeting, March 21-23, 2010, Champaign, IL.
- W. Merchan-Merchan, A.V. Saveliev, and **W. Cuello Jimenez**, “Flame gradient synthesis of transition metal oxide nanostructures in an opposed flow methane oxy-flame”, 6th U.S. National Combustion Meeting, May 19-2009, Ann Arbor, Michigan

**Much of the material in Chapters 1 and 2 of this dissertation is verbatim from a recently published Book Chapter. Co-authors have granted full authority for the reproduction of the material.**

W. Merchan-Merchan, W. Cuello Jimenez, O. Rodriguez Coria, C. Wallis, Chapter 7 – “**Flame Synthesis of Nanostructured Transition Metal Oxides: Trends, Developments, and Recent Advances**”, Editor(s): Yasir Beeran Pottathara, Sabu Thomas, Nandakumar Kalarikkal, Yves Grohens, Vanja Kokol, In Micro and Nano Technologies, Nanomaterials Synthesis, Elsevier (2019) 201-263.

# 1. CHAPTER 1: INTRODUCTION TO TRANSITION METAL OXIDES (TMOs)

---

Material scientists have focused significant attention to study metal oxides owing to their remarkable properties and multiplicity of structure morphologies that can be synthesized [1]. The conversion of some transition elements (TMs) to their equivalent oxide forms results in material with outstanding optical, electrical, magnetic, mechanical, and catalytic properties; thereby, making them materials of increasing scientific and technological interest. Millions of tons of TMOs with spherical morphology are being produced every year, typically employed in paints as pigments, as fluoresce for medical devices, petroleum refining, recording media, among other applications [2]. However, in recent years nano sized TMO structures involving 1D, 2D and 3D morphologies are highly sought after nanomaterials (NMs). The unique morphologies of TMOs (aspect ratios and shape) combined with their molecular structure yield NMs with remarkable properties and of a broad range of applications. Owing to the unique properties of these NMs they have found themselves as important components in various sectors including in healthcare (i.e. in drug delivery for tumor therapies), renewable and clean energy (i.e. increasing power output in solar panels and or increasing the performance in Li-ion batteries), as catalytic material (i.e. for hydrogen and green gasoline production), electrochromic materials (i.e. for smart building applications), and many other applications [3,4,5,6,7,8].

## 1.1 Motivation to Study TMOs

The largest group of elements of the periodic table is the so-called transition metals (TMs). This includes groups 3 to 12 (d-block) and the f-block. According to the

International Union of Pure and Applied Chemistry (IUPAC) a TM is any element with a partially filled *d* electron sub-shell. In TMs the valence electrons are present in more than one shell and often exhibit several common oxidation states [9,10]. The f-block elements (lanthanide and actinide) are referred to as “*inner transition metals*” or more commonly as “rare earths”. Despite many similarities, the TMs do vary considerably in certain properties. There is a general decrease in size of atomic radii from left to right for each of the series in the periodic table. There is a significant increase in atomic radius from 3d to 4d metals, although, the 4d and 5d metals have remarkably similar atomic radii. Within the 3d, 4d, and 5d block of the transition series all of these elements contain cubic and hexagonal crystal structure with the exception of Hg which contains rhombohedral structure. Some of these metals have very different melting points such as W with 3,410°C and Hg as a liquid at 25°C. TMs such as Mo, Fe, and Ti present high hardness, great strength, and make very useful structural materials; others such as Cu, Ag, and Au, are relatively soft and highly conductive.

The simple intercalation of a TM with oxygen to form a new material, transition metal oxide (TMO), can significantly improve the properties of the base metal. Experimental and theoretical studies have shown that by converting bulk material into minute structures (at the nano- and micron-sized range) a remarkable modification of their properties (i.e. chemical, catalytic, magnetic, electronic properties) relative to their bulk can take place (see **Table 1**). Additionally, the alteration of the elemental composition of the nano- and micron-sized structures (i.e. 1D and 3D) from its bulk material can significantly enhance the material properties providing many useful applications and this has generated a significant interest within the scientific and industrial communities.



Materials with such improved properties due to their transformation from bulk to nano-/micron-size and the modification of the elemental composition are TMOs. More recently, it has also been shown that the mixing of two transitional metals to form a mixed transition metal oxide (MTMO) structure can result in a structure that has superior properties. Different methods and techniques have been developed for the synthesis of various types of TMOs. The flame method represents a single-step process where the structures can be formed in a few minutes or even seconds. The underlying hypothesis of the flame synthesis is that coherent variations in temperature and chemical species can produce controlled growth conditions leading to controlled and highly selective formation of TMO nanostructures. The flexibility to introduce various synthesis parameters has yielded a wide-spectrum collection of TMO nanostructures with varying shape (i.e. spherical vs. 1D & 3D), structure (crystalline vs. amorphous), elemental composition (stoichiometric vs. nonstoichiometric), and mixing type (uniform vs. nonuniform or core-shell). Therefore, the focus of this chapter is to provide an insight into the many studies conducted in the application of flames for the synthesis of TMOs. Different approaches taken by several experts/researchers in this field used to control the variety of chemical and physical morphologies in the flame generated TMOs are presented in this chapter.

**Table 1.** Properties and applications of metal oxides, adapted from [11].

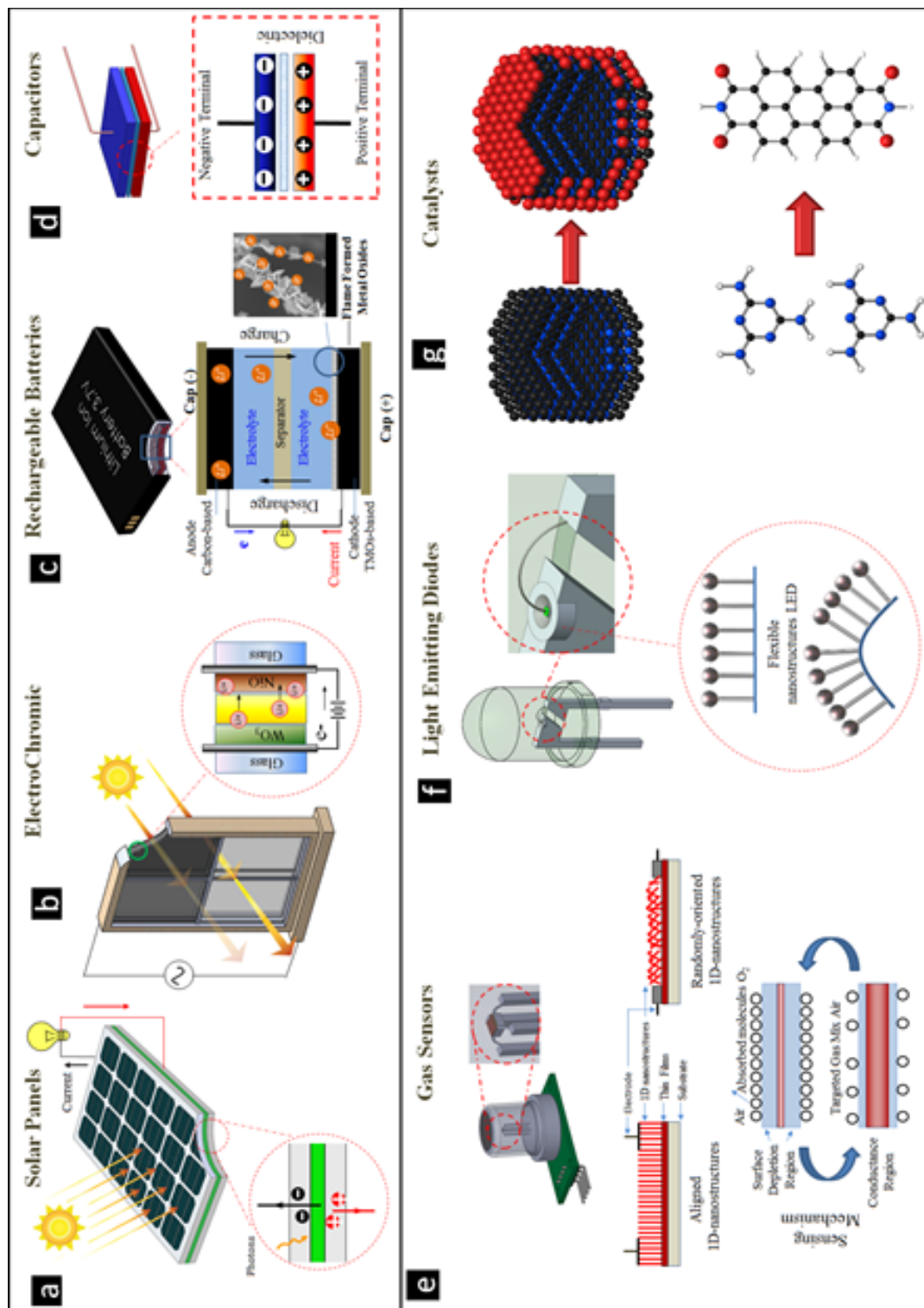
Metal Oxides	Properties	Applications
Fe <sub>3</sub> O <sub>4</sub>	Sorbent	Removal of arsenic III and IV from water
γ-Fe <sub>2</sub> O <sub>3</sub> , BaFe <sub>12</sub> O <sub>19</sub>	Super paramagnetic	Cancer detection and remediation, sensors, and memory devices
TiO <sub>2</sub> , Fe <sub>2</sub> O <sub>3</sub> , Cr <sub>2</sub> O <sub>3</sub>	Colors	Ceramic pigments
Al <sub>2</sub> O <sub>3</sub> , CeO <sub>2</sub>	Hardness	Abrasive
TiO <sub>2</sub> , CeO <sub>2</sub> , Fe <sub>2</sub> O <sub>3</sub>	Catalysts	Air and water purification
TiO <sub>2</sub> , ZnO	UV-Vis sunlight absorbing	Photocatalyst, sunscreen, and paint
	Color	Pigment in ceramics and paints
WO <sub>3</sub>	Electrochromic	Smart windows, information displays
	Gaschromic	Sensing of NH <sub>3</sub> , HS <sub>2</sub> , NO <sub>2</sub>
	Photochromic	Sunglasses, data storage
Al <sub>2</sub> O <sub>3</sub> , ZrO <sub>2</sub>	Refractory	Toughened ceramics
MTi/ZrO <sub>3</sub> (M = Ca, Sr, Ba, and Pb)	Dielectric	Sensors, MEMS
Y <sub>2</sub> O <sub>3</sub> -ZrO <sub>2</sub>	Electrolyte	Solid oxide fuel cell

## 1.2 Properties and Applications of 1D and 3D TMO Nanostructures

Owing to the unique properties of TMO NMs we have seen a significant increase in their application as important components in various sectors including in the fields of photocatalysts [12,13], luminescence [14,15], piezoelectric transducers and actuators [16-24], electrochromic displays [25,26], high-performance anodes in Li-ion batteries [27-30], gas sensing components [31,32], data storage media [33], optical absorption and emission [34], biosafety and biocompatibility [35], among others. Popular applications of TMOs in selected technologies are briefly described below (**Fig.1**).

### ***1.2.1 Solar Panels***

In the solar panel industry the use of photovoltaics allows for the conversion of sunlight (photons) into electricity (**Fig. 1a**). Si-based solar cells have been in development for over 50 years [36], however, efficiencies of only 5-15% are typically attained in commercially available cells as a result of the reduced utilization of photons by the Si-layer of the cell [37,38]. The uses of different types of photovoltaic materials, of unique morphological characteristics, and of nanostructured scales have become topics of study in recent years for increasing the power output of solar panels [39]. That is, electron transport in photoactive materials (regardless of its type) can be influenced depending on whether the material is in: i) bulk or micron sized compared to nanosize scales. Nanosized photoactive materials are reported to offer advantages in enhancing the efficiency of the cells by the increased surface-to-volume ratio. That is, nanosized NMs allow for a shorter diffusion path for charge carriers to the surface, additional adsorption sites for reactants, and more active sites for the catalytic reactions, in addition to the localized electronic states favoring charge transport and trapping near the surface. ii) Physical morphological properties of the photoactive materials (spherical vs. non-spherical, regardless of the type of material). Spherical particles have been employed for solar panel applications. However, they possess a key problem: coalescence of the fabricated atomic clusters, affecting the original physical and chemical interactions. However, 1D-nanostructures (nanowires, rods, tubes, cones, etc.) applied to photovoltaics favor the influence of both absorption and reflection due to light scattering between the nanostructures which increases the travel path for the photons.



**Fig. 1.** Typical applications of nanostructures multi-dimensional TMOs: (a) solar panels; (b) electrochromic; (c) rechargeable batteries; (d) capacitors; (e) gas sensors; (f) light emitting diodes; and (g) catalyst.

Moreover, 1D structures orthogonalize the direction of electron transport, which facilitates the absorption of light and the collection of charge carrier; whereas, 3D structures result in improved surface reaction rates, electrical transport, chemical stability, specific surface area which causes a dramatic enhancement in storage ability. The exceptional review of Anta et al. shows the intensive efforts by various research groups to study the efficiency of light harvesting devices based on nanostructured metal oxides [30]. One application of the metal oxide for solar cells relies on creating nanostructured films [40,41]. It has also been shown that thermal treatment (annealing) of the films can result in significantly higher external quantum efficiencies compared to the not-annealed solar cells [42,43]. For instance, Dittrich et al. showed that annealed thin absorber layers based on ZnO nanowires with length of 1.5  $\mu\text{m}$  coated with absorber materials of 25  $\mu\text{m}$  of  $\text{In}_2\text{S}_3$  and CuSCN resulted in higher efficiencies compared to those non-annealed layers [34]. Kuznetsov et al. [44] reported the use of TMO nanorods to coat Si-based solar cells to increase their power output to levels up to 5%. Thus, two different mechanisms can be proposed to enhance solar cell power output/efficiency: (1) replacing Si-films with other materials that require thin films, or (2) coating the Si-films with nanostructures to increase the film surface-to-volume ratio, and thus, its efficiency. Hybrid components can also result in enhancement of power conversion efficiency, for instance ZnO nanorod structures combined with poly-3-hexylthiophene polymer results in conversion efficiency of over four times greater than that of similar devices based on single nanoparticles [45].

### **1.2.2 Electrochromic (EC) Devices**

An application of electrochromic properties is shown in **Fig. 1b** using a “smart window” as a typical application. A smart window typically employs two EC films; one a

cathodic oxide and the other an anodic oxide. Upon an electrical stimulus, ion insertion/extraction will cause both films to undergo color-bleach cycles. Briefly, a generic EC device consists of several superimposed layers placed in between two transparent substrates (i.e. glass, polycarbonate, polyethylene terephthalate, etc.) [46]. The variation of the optical properties results from ion insertion/extraction via centrally positioned electrolytes from the EC films. Small ions are typically favored for such purposes (i.e. H<sup>+</sup>, Li<sup>+</sup>, etc.), **Fig. 1b**. Transparent liquid and/or polymeric-based electrolytes and ions carrying thin oxide films are typically employed [37]. The ion transfer can be triggered by applying an electrical field between the two EC films, a voltage of 1-2 V DC is typically required, which suggests that powering the systems is easily possible [47]. The movement of electrons can result in intervalence transition (i.e. yield polaron absorption), which is the main reason for optical absorption [38]. Films are commonly fabricated based on NMs with tailored nanoporosity and of TMOs based on two types of oxides. Cathodic EC film (coloring under ion insertion, i.e. Ti, Nb, Mo, W, Ta) and an anodic EC film (coloring under ion extraction, i.e. Cr, Mn, Fe, Co, Ni, Rh, Ir). A significant amount of effort has also been devoted to the development of superior EC films. For instance, the formation of V-based oxides which are hybrid in nature (anodic/cathodic) and the use of mixed transition metal oxides (MTMOs). Mixed TMOs can yield optimized properties with superior performance when compared to the individual oxides. For instance, W-Ti oxide results in enhanced electrochemical cycling durability as a result of the addition of Ti to the parent material [48]. Additional examples of W-based films hybrid oxide involve combinations with Ag [49], Pt [50], Au [51], Ta [52], Mo [53], Ru [54], Ni [55], V [56], etc.

### 1.2.3 *Lithium-ion Batteries (LIBs)*

Commercially available LIBs (**Fig. 1c**) employ films of spheroidal shaped transition metal oxide particles as cathodes. These are the most advanced among the rechargeable batteries available to date [57]. Recently, in order to improve the performance of rechargeable batteries, the use of a cathode having one of its surfaces coated with a layer of 1D and 3D TMO nanostructures instead of conventional bulk microcrystalline films has become a very attractive field of study [58-60]. Cathodes coated with bulk microcrystalline metal oxides generally suffer from poor kinetics and/or capacity fade with cycling. On the other hand, cathodes composed of 1D and 3D TMO nanostructures have recently been shown to improve the rate capabilities of solid-state electrodes because of the small diffusion lengths [61]. Typically, nanoparticles are not very stable and difficult to fabricate on large scales; which has driven research to focus on 1D nanostructures that can render electrochemical LIBs more versatile. Nonetheless, in order to obtain higher energy and charge densities, 3D nanostructures may be required, due to electrodes having higher surface areas, large surface to volume ratio, mass transport abilities along with favorable structure stability over 1D structures and nanoparticles. There are significant efforts aimed at developing novel electrodes to eliminate the dependence on carbon materials (carbon based electrode) and to further optimize their performance [62]. Much attention has been devoted to transition metal oxide (TMOs) nanostructures as candidates for LIBs electrodes since they can offer advantages of large and reversible capacities of 2 to 3 times greater than graphite, along with corrosion resistance, eco-friendliness, less volumetric expansion upon lithiation, better lithium intercalation process, and optimum cost-performance ratio [63].

#### **1.2.4 Capacitors**

TMO nanostructures (2 to 50 nm) have attracted much attention in energy storage applications not only due to their outstanding mechanical, electrical and structural properties, but also because of their high pseudocapacitance (capacitors) as a result to their multiple valence state changes typically not possible with carbon-based materials [64]. Moreover, their large specific surface area and suitable pore size distribution are also features that favor their use for capacitor applications [65] that result in high specific capacities due to effective contact between electrodes and electrolyte along with enhanced transportation of ions/electrons in both the electrode bulk and the electrode/electrolyte interface (**Fig. 1d**).  $\text{RuO}_2$  ( $720 \text{ F}\cdot\text{g}^{-1}$ ) and  $\text{IrO}_2$  ( $550 \text{ F}\cdot\text{g}^{-1}$ ) nanoparticles are recognized as the most promising candidates for capacitor applications due to their very large specific capacitance values. However, low specific surface area is one of their disadvantages. This shortcoming is addressed by employing 1D nanostructures that are capable of solving the issue of specific surface area, and thereby enhance the electrode active material utilization. 3D structures, however, improve the surface reaction rates, electrical transport and chemical stability along with optimized surface area, and facilitation of ion transfer in the system with improved storage capacity. Hybrid structures are reported to further improve the capacitance performance,  $\text{NiCo}_2\text{O}_4$  nanoneedles grown on 3D graphene-Ni foam resulted in capacitance of up to  $1588 \text{ F}\cdot\text{g}^{-1}$ .

#### **1.2.5 Gas Sensors**

It is now well-known that the electrical conductivity of metal-oxide semiconductors is very sensitive to the composition of the surrounding gases. This property can be utilized in the production of gas sensors. Oxygen vacancies on the surface of metal



oxide materials cause changes in electrical conductivity of the materials as a result of molecular adsorption. Consequent to the adsorption of some molecules, such as NO<sub>2</sub> or O<sub>2</sub> at the vacancy sites, conductivity is reduced. But the conductivity increases when molecules, such as CO and H<sub>2</sub>, are adsorbed at the vacancy sites on the surface. Most metal-oxide gas sensors operate based on this principle [66].

Similar to the above described applications, the sensing properties of NMs can be affected by several factors including its: i) chemical composition, ii) surface modification with other metals, and iii) morphology, among others. A gas sensor typically consists of a coated ceramic tube (i.e. metal oxide), where the coating corresponds to the sensing film with predefined thickness (**Fig. 1e**). The actual sensing mechanism consists of the nanostructures (i.e. TMOs) exposed to a targeted environment (i.e. gas mixed air). This results in O<sub>2</sub><sup>-</sup> ions (formed on the surface) by getting an electron from the conduction band, which results in electron depletion at the surface (**Fig. 1e**). Upon interactions with volatile compounds and/or chemical species through adsorption, chemical reactions, or charge transfer, the physico-chemical properties of the sensing film can be modified, thus generating an electrical signal [67]. However, both the chemical composition and the physical morphological properties play key roles in determining the performance metrics of these sensors.

#### *1.2.5.1 Chemical Composition:*

One of the key advantages of TMOs gas sensors refers to their ability to have reversible interactions between the sensing film and the gas, which is characteristic of conductometric semiconducting metal oxides [68]. Only TMOs with d0 and d10 electronic configurations are ideal for gas sensing applications. Moreover, the sensitivity of gases in

a gas sensor can be optimized when using core-shell TMOs of various elemental compositions [69]. Similarly, sensors formed from a combination of metal oxides have been shown to exhibit significantly higher sensitivity than sensors constructed solely from a binary composition [70,71]. A literature survey of different metal oxides employed for gas sensing applications suggests that ZnO and SnO<sub>2</sub> are the most extensively researched for sensing films in chemoresistive gas sensors [72]. However, it has been shown that a binary composite ZnO-SnO<sub>2</sub> sensor exhibits superior sensitivity to sensors constructed solely from zinc oxide or tin oxide under identical experimental conditions [C.L. Zhu et al. 61].

#### *1.2.5.2 Physical Morphological Properties:*

The specific shape of employed sensing materials can play a critical role on their performance owing to the fact that higher active surface areas result in higher sensitivity between the sensing materials and the targeted gas. For instance, Geng et al. [73] indicated that 14-faceted polyhedral ZnSnO<sub>3</sub> microcrystals resulted in higher sensitivity than octahedral components, mainly due to the increased active surface for interaction when exposed to multiple gases including H<sub>2</sub>S, C<sub>2</sub>H<sub>5</sub>OH, and HCHO. Moreover, gas sensors are frequently required to operate in very challenging environments (i.e. temperatures up to 600 °C [74]), which results in significant operational limitations as a result of the sensor's poor sensitivity at such conditions. However, metal oxides with nanoscale dimensions have been found ideal for such extreme environments. The nanoscale TMOs forming the sensing film enhance the adsorption of gases due to the significant increase of the surface area compared to their micro or bulk counterparts. The use of nanoscale TMOs increases the sensor's sensitivity and allows for expanding the operational regime of the devices.

Typically, nanostructure arrangements for gas sensing applications consist of aligned and randomly oriented 1D structures, as a result of their unique features associated with low dimensionality and lowest size making the fabrication of nano devices a reality. Binary TMOs such as  $\text{TiO}_2$  and  $\text{V}_2\text{O}_5$  represent the  $d^0$  configuration; whereas post-TMOs such as  $\text{ZnO}$  and  $\text{SnO}_2$ , represent the  $d^{10}$  configuration.

### ***1.2.6 Light Emitting Diodes***

Recent advances suggest the use of nanoengineering for fabricating flexible and high temperature resistance LEDs (**Fig. 1f**). Typically TMOs and hybrids thereof are employed for these applications, especially those composed of 1D heterostructures grown directly on top of flexible films which are ideal for optoelectronic devices with flexible, transferable and stretchable features [75]. In particular hybrid nanorods synthesized on graphene-based flexible films with very small contact areas favor great endurance under deformation [76]. Nanostructure morphology also plays a critical role in light output power, for instance, 3D cone-shaped nanostructures with side-wall angles of  $24.1^\circ$  resulted in light out power enhancement of 300% higher than flat surface conventional LEDs [77]. The ability of TMO nanostructures and/or nanoparticles to participate in redox and acid-based reactions makes them suitable for applications as catalysts for industrial applications [78,79]. In recent years, much effort has been devoted to the field of nanotechnology and nanoscience in regard to TMOs due to their relatively high chemical activity along with defined interactions [80-83]. TMO nanoparticles with increased surface area to volume ratios are highly efficient considering the oxidation reaction takes place at the surface oxygen.

### 1.2.7 Catalysis

In recent years, much effort has been devoted to the field of nanoscience in regard to TMOs due to their relatively high chemical activity along with defined interactions [71,84]. TMO with increased surface area to volume ratios are highly efficient considering the oxidation reactions that can take place at the surface, **Fig. 1g**. Their performance as catalytic NMs can be further optimized by placing the TMOs particles on a magnetic core, and thus allowing for collection and separation of the catalyst from the resulted mixture when exposed to a magnetic field. Furthermore, employing magnetic nanoparticles allow for recycling of the catalyst as a result of the ease of its recovery capabilities at the end of the reaction, along with the ability of turning off a reaction by applying a magnetic field [58]. Generally, the specific catalytic activity, per unit mass or per unit of surface area, increases with reduced particle size, however, decreasing particle sizes can also result in nanoparticle agglomeration as a result of lack of stability [85]. Though, this is typically resolved by immobilizing active species on solid supports. Although, Mn-oxide nanoparticles are known as efficient catalysts in the oxidation of olefins with epoxides as products [86], Rahaman et al. reported the preparation of Mn<sub>2</sub>O<sub>3</sub> 1D structures (i.e. nanorods) with enhanced catalytic activity and high selectivity for the direct synthesis of multiple aldehydes via oxidation of alcohols [87]. Furthermore, it is important to highlight the fact that the catalytic activity of nanoscale structures can result in 75% improvement in catalytic activity when compared to bulk components [88]. 1D structures have gained increased focus in photocatalyst applications as a result of their large surface-to-volume ratio and lower number of grain boundaries [89]. 3D mesoporous structures have been reported to yield high catalytic activity due to their ability to generate high light harvesting

ability along with the reduction of the recombination rate between photoelectrons and holes.

After describing the multiple applications, it is interesting to note that the capacity of some TMOs to exist in various oxidation states and with a large variety of crystal structures, and others with an ability to undergo phase transition configurations (physical and chemical), makes them unique. Depending on the type, some TMOs are essential in catalysis (large surface area for photocatalyst applications), photoelectrochemical (i.e. photochromism, in reference to the reversible change in color or optical properties of a material upon exposure to light), electroluminescence (i.e. light-emitting diode), electrochemical (i.e. Li-ion batteries), optical properties (i.e. in solar panels), among others. Some of these technologies will have far reaching practical application as TMOs with superior properties are being exploited for the development of many new technological applications as discussed above.

### **1.3 Outline/Organization of the Dissertation**

**Chapter 1** presents the motivation behind this research thesis on the flame synthesis of TMOs and outlines the need for this study. It describes the benefits of intercalating an oxygen molecule into a bulk transition metal to form metal oxide nanostructures. It discusses the importance of particle shape (spheroidal, 1D and 3D) and size (micron and nano) of TMOs to improve their properties and applications. Moreover, a detailed review of the multiple applications of selected TMOs that support the need for this research is also illustrated.

**Chapter 2** provides a comprehensive literature review containing significant insights in regard to multiple fabrication techniques of TMOs nanostructures. In this chapter typically used classic and conventional non-flame methods for the synthesis of TMOs are presented and compared with various flame methodologies. Interestingly, this chapter describes the benefits of employing flames as a flexible and inexpensive technique (when compared to its non-flame counterparts) for the synthesis of TMOs nanostructures with unique and complex morphologies.

**Chapter 3** contains the core research objectives of thesis along with the impact thereof. One of the main objectives of this thesis consists of gaining further insights into the underlying mechanism that a solid support (material source) exposed to a high temperature oxygen rich medium (oxygen flame) can result on the synthesis of hybrid and multi-dimensional structures with complex morphologies both on the solid support surface and in the gas-phase. This new knowledge can certainly aid in enhancing the solid support and the gas-phase synthesis of new complex TMOs with remarkable properties and hence enable novel applications.

**Chapter 4** describes the combustion reactor used in this research, along with key features of the counter-flow diffusion flame, numerical predictions of the major chemical species and the temperature profile distribution. Furthermore, the process of the metallic probes (i.e. bulk material sources) insertion into the flame medium and the sample preparation for both scanning electron microscopy (SEM) and transmission electron microscopy (TEM) analyses are also presented herein.

**Chapter 5** summarizes the result of the initial evaluation of the synthesis of TMOs on a single solid support employing a single metal precursor and the proposed growth mechanism of the fabricated structures. This part of the work sets the foundation for the solid support synthesis of TMOs with hybrid/complex/multi-dimensional nature.

**Chapter 6** introduces the concept of gas-phase combustion as a versatile and promising technique for synthesizing TMO nanostructures. Further insight as to how the material growth takes place within the flame volume serves to gain additional understanding on the overall synthesis of TMO nanostructures with well-defined atomic structure in (i) the gas-phase, on how the structures evolve from shapeless discrete particles to octahedral and elongated rod-like polygonal structures, and (ii) a single solid support.

**Chapter 7** focuses on the synthesis of complex heterostructures with a multiplicity of morphologies tailored based on substrates flame position, residence times, substrates insertion time, and azimuthal crystallization sites.

**Chapter 8** present the concluding remarks of the dissertation along with recommendations on future work.

## 2. CHAPTER 2—LITERATURE REVIEW

---

In this chapter, trends, developments, and recent advances in the various methods for the synthesis of transition metal oxides (TMOs) are explained by reviewing several scholarly works on this field. It includes non-flame and flame methodologies developed for the synthesis of TMOs. Detailed description of multiple studies where flames were employed to fabricate TMO structures of multiple morphologies (i.e. spherical, 1D and 3D) in both solid substrates and in the gas-phase. The flame methods are compared to other methods for the synthesis of TMOs including chemical vapor deposition (CVD), sol-gel, and plasma.

In relation to the flame synthesis of TMO nanostructures, it discusses various types of flames including normal and inverse diffusion, premixed, and partially premixed flames, along with the types of combustion-based burners employed for synthesis, i.e. counter-flow, flat flame, co-flow diffusion, and premixed burners. The various forms of introducing the source or bulk material into the flame media is discussed. Interestingly, most industrial flame synthesis techniques focus on spherical nanoparticles for mass production; however, recent advances on multi-dimensional structures (1D to 3D) with unique morphologies (i.e. grass, flower, tree, forest, polyhedral, etc.) have gained much attention for novel applications and devices, i.e. batteries, electrochromic windows, catalyst, drug delivery, etc. Furthermore, this chapter also discusses the flame synthesis of mixed transition metal oxides (MTMOs), where the combined physico-chemical nature and morphology of the resulting nanostructures are highly desired for optimal and tailored



performance. It is also emphasized that the flame synthesis method of TMO nanostructures includes both solid supports and gas-phase as the key to volumetric growth.

## **2.1 Synthesis and Methodologies to Form TMO Nanostructures: A Review and Analysis of Flame and Non-flame Synthesis Techniques**

Methods for the synthesis of these novel TMOs are to be robust, scalable, energy efficient and inexpensive in order to suffice the requirements of current and future applications. A variety of techniques have been proposed and developed for the synthesis of TMOs including aqueous chemistry [90-92], chemical vapor deposition [93-95], pulsed laser deposition [96-98], high temperature heating process in a restricted vacuum chamber [99], and metalorganic vapor phase epitaxy [100], combustion synthesis methods or self-propagating high-temperature synthesis [101], and flames, among others. All of these methods are based on the assembly of molecules through evaporation and deposition on a substrate through vapor-phase transport or chemical reactions. Through this method, highly pure crystalline and complex nanostructures (physically and/or chemically) can be produced. Although most of these methods are capable of producing TMOs, most are generally limited by the complexity of the process, scalability, and purity of its products. However, combustion/flame synthesis methods have emerged as highly flexible, rapid, relatively inexpensive, robust, and single-step process with a broad potential for high-volume commercial production of various nanoscale materials with controlled and complex morphologies compared to the other aforementioned techniques. Thus, flames have evolved into one of the most versatile and promising methodologies employed for high volume/commercial production of nano-scaled materials [102,103]. **Table 2** lists and

highlights specific methods and their combinations that have been employed to synthesize TMO nano/micro structures.

### ***2.1.1 Chemical vapor deposition (CVD)***

In this method, thin films of TMOs can be formed on a substrate through chemical reactions. Oxygen and/or non-reactive gases are fed into a furnace chamber and the gases react with the metal source and deposit on the substrate to form a thin film of metal oxide. A variety of CVD configurations have been established and examined for the synthesis of TMOs. The CVD configurations include plasma enhanced CVD, vapor trapping CVD, vertical furnace, and plasma enhanced CVD among others [104]. Generally, CVD synthesis mechanisms use temperature to trigger the gaseous precursors, however, the formed structures can differ significantly with respect to each other regarding their structure, composition, and properties due to multiple factors including temperature (i.e. deposition and sublimation), substrate, gas flow or vapor/gas ratio, pressure, growth time, cooling rate, etc., which all play a key role in the fabrication process [105,118]. Gesheva et al. [118] employed a low temperature CVD technique to fabricate W-, Mo-, and molybdenum/tungsten-oxide films for electrochromic applications for smart windows. Their process exposed the respective substrates to temperatures ranging from 150 – 200°C and vapour source temperatures of 90°C, resulting in growth rates of 6-10 nm/min. Zhou et al. [120] employed a plasma enhance CVD technique to synthesized MoO<sub>2</sub> nanowire arrays on silicon substrates. Substrate temperatures and experimental synthesis times of 1100°C and over 60 min were attained, respectively. Interestingly, based on the reported CVD techniques, the grow rate tends to increased with decreasing dimensionality and increasing crystallinity (i.e. from amorphous to crystal-based structures) of the structures

[118,120]. Generally, CVD methods allow for production of uniform and high-quality thin films. However, The resulting structures can exhibit significant variations in their structure, composition, and properties, depending on several factors such as temperature, substrate type, vapor/gas ratio, pressure, growth time, cooling rate, etc. These parameters play a critical role in the fabrication process, and slight changes can result in significant differences in the final structures. Moreover, this technique requires multiple steps and several hours in order to yield nanosutrcutres production, which represent disadvantages for large scale production of multidimensional structures.

### **2.1.2 Sol-gel**

The sol-gel method is based on the formation of an oxide network through reactions of a metal (source) in a solution. A sol is a stable dispersion of amorphous or crystalline particles in a solvent. And a gel encompasses a solution. In this method, the film of material is formed from agglomeration of the particles. Galatsis et al. [124] synthesized Mo-, W-, Ti-, Mo/Ti- and molybdenum/tungsten-oxide structures for gas sensors applications. Their process consists of: (i) mixing precursors in few minutes; (ii) place the sols materials in ultrasonic bath for 1 hour; (iii) settling and aging at room temperature for 24 hours; (iv) placing solutions on substrates and spun at 2500 rpm for 25 s.; (v) allow films to gel on substrates for 24 hours at room temperature; and (vi) annealing to 450 and 500°C for 4 hours. It is important to note that this synthesis mechanism typically requires over 50 hours for films or structure sysnthesis. Niederberger et al. [130] introduced the fabrication of molybdenum-oxide nanofibers using a sol-gel technique with production times of at least 5 days. From various of these studies, it is evident that regardless of the dimentionality (1D vs 2D) and the crystallinity of the structures, the frabrication times are in the range of 3-7

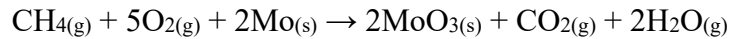
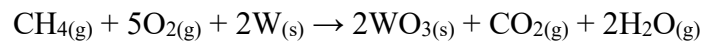
days [124,125,130]. Typically, sol-gel is a versatile technique for producing a variety of nanostructures, including thin films and powders. However, sol-gel requires multiple steps and long processing times to produce high-quality products and often results in agglomerated spherical structures, which can be a disadvantage for large-scale production of multidimensional nanostructures.

### **2.1.3 Plasma**

Most recent plasma reactors have been redesigned for the synthesis of TMOs. In the plasma method, two graphitic probes perform as the negative and positive electrodes. An electrical discharge is created as a result of a conducting path between the two electrodes. Similar to the CVD combinations, a variety of plasma configurations (sputtering, cathodic electrodeposition, and anodization, etc.) have been designed and tested for the formation of TMOs. Hu et al. [137] generated hollow crystalline tungsten-oxide fibers employing a plasma-like setup with currents of 40-55 A and substrate temperatures of 1300-1400°C during 1 hour. Depero et al. [106] reported the synthesis of W/Ti-oxide thin films using a reactive sputtering coupled with an annealing process at 600-800°C for approximately 12 hours. Mixed molybdenum/tungsten-oxide films were also produced via sputtering by Vomiero's group [135]. Despite the plasma technique being able to reach high temperatures rather quickly, it has been reported the additional annealing process, typically greater than 10 hours, is highly responsible for the morphological and compositional evolution of the formed films [135].

#### 2.1.4 *Flames*

Although the above-described classic conventional (non-flame) methods are capable of producing TMOs, some of them are generally limited by the complexity of the process (multi-step), scalability, and selectivity of its products. Most of these methods require several hours for the synthesis process, whereas flame synthesis can be achieved in a matter of minutes or seconds. Flame as a synthesis technology represents a method capable of producing nanoparticles and nanofibers at the scale of several million metric tons annually due to its simplicity [107,108]. For instance, flame generated materials include carbon blacks and of the highly ordered nanostructured carbon materials such as carbon nanotubes, fullerenes, fullerene derivatives, fumed silica, titanium dioxide or titania with and without pigmentary properties and optical fibers [109,110,111]. Every year, millions of tons of single metal oxide particles (such as TiO<sub>2</sub>, Al<sub>2</sub>O<sub>3</sub>, GeO<sub>2</sub>, PbO, V<sub>2</sub>O<sub>5</sub>, Fe<sub>2</sub>O<sub>3</sub>, SnO<sub>2</sub>, ZrO<sub>2</sub>, and ZnO) are produced through flame-based inexpensive, single step, and rapid synthesis method [97,112]. Typical theoretical reactions of methane flame with oxygen and transition metals to form TMOs nanostructures are described below:



**Table 2. Methods used for the synthesis of TMOs nanomaterials.**

Method	Experimental configuration	References
CVD and Related Processes		Nb-oxide [113,114] Zn-oxide [115,116,117] W-oxide [118-119] W/Mo-oxide [118] Mo-oxide [120]
Sol-gel and Related Processes		Nb-oxide [121, 122] Zn-oxide [123] Mo-oxide, Ti/W-oxides [124-125] Fe-oxide [126,127,128,129] Mo-oxide [124,130]
Plasma and Related Processes		Nb-oxide [131,132] Zn-oxide [133, 134] Mo/W-oxides [135,136,137] Fe-oxide [138]
Flames		[139]

Every year, millions of tons of  $\text{SiO}_2$ ,  $\text{TiO}_2$ ,  $\text{Al}_2\text{O}_3$  [97] and  $\text{ZnO}$  [140] are produced through this considerably rapid and inexpensive method. Various combustion-based processes and unique catalytic-fed methods have been employed for the synthesis of TMO nanopowders. Typical methods of precursor delivery into the flame medium for synthesis

of TMOs include “*aerosol*” and “*flame spray pyrolysis*” (FSP) (**Fig. 2a**). Typical advantages of flame synthesis of nanostructures involve the production of multidimensional structures with controlled size, morphology, and composition, making it a promising technique for a wide range of applications. The resulting nanostructures can have unique shapes, such as hollow, core-shell, or hybrid structures, which can be challenging to produce using other techniques. However, the growth mechanism of the complex and hybrid flame formed structures may not be very well understood to unlock its full potential.

Burner configurations are an important aspect of flame synthesis of nanostructures since it affects the temperature, chemical species, and stability of the flames. The typical burner configurations consist of the counter-flow, co-flow, and flat flame reactors:

- i.* Counter-flow burners are designed so that the fuel and oxidizer flow in opposite directions and impinging against each other to form a typically 1D counter-flow diffusion laminar flame suitable for studying soot, carbon nanotubes and TMO nanostructures. This configuration promotes efficient mixing and combustion due to the high shear forces between the two streams as well large temperature and chemical species gradients of the order of 2000 K/cm and hydrocarbon-rich to oxygen rich-distinctive zones, respectively [109].
- ii.* Co-flow burners are designed so that the fuel and oxidizer (or their mixtures) flow in the same direction, typically from the center of the burner to the outside. This configuration creates a longer flame, making co-flow burners ideal for applications where a long flame is required, such as in glass melting or steelmaking. This configuration can yield premixed or diffusion flames, with premixed reactor

representing the best efficiency and less unburnt fuel as a result allow for accurate temperature and emissions control. However, they are also the least safe as a result of potential for flashback [141]. Diffusion co-flow reactors offer added flexibility and safety compared to their premixed counterparts due to the ability to inject fuel and oxidizer either through the center and outer nozzles or vice versa, hence characterizing the flame location, soot oxidation rates, and size of the characteristic oxygen and hydrocarbon rich zones [142].

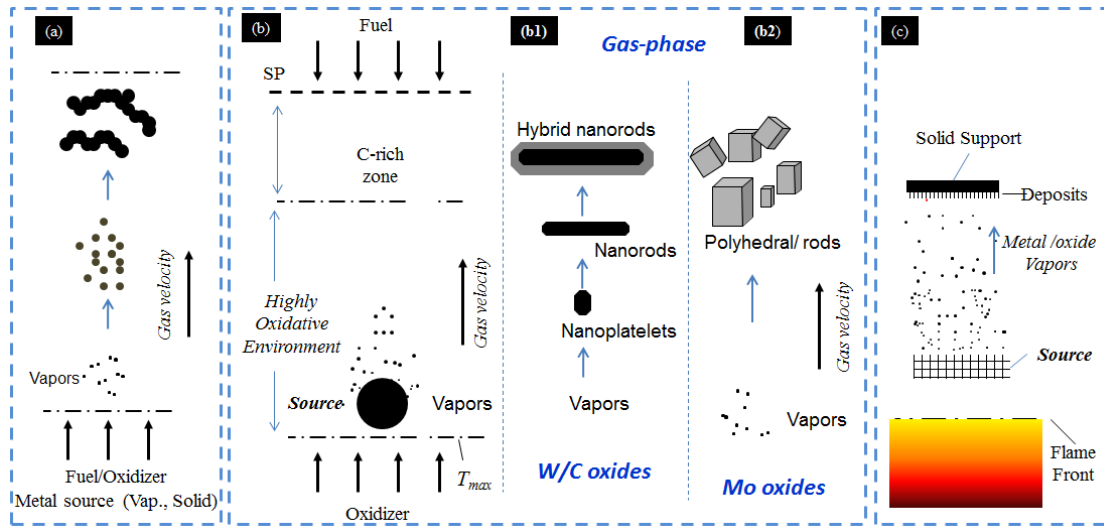
*iii.* Flat flame burners are designed to produce a flame that is flat and wide, rather than the typical cylindrical shape of counter-flow and co-flow flames. This configuration allows for a larger heat transfer area and can be useful in applications where the flame needs to cover a wide surface area, such as in industrial ovens or kilns. The flat geometry is achieved by either employing a perforated plate burner or a flat porous end plate [143]. This configuration has been commonly used to investigate the key features of premixed laminar flames for studying hydrocarbon pollutants [143] and most recently the evaluation of nanoscale materials synthesis [164].

Interestingly, all three main configurations have been used for the synthesis of nanoscale structures [139]. Furthermore, it is important to consider that some of these flame techniques could be impeded by the harvesting process of the grown structures, particularly they are grown directly in the gas-phase medium.

It has been shown that reacting mixing additives, introduction of electric fields, among other processes can be used to control morphology (primary particle size, agglomeration, shape, particle crystallinity, etc.) and composition in the flame synthesis of



TMOs. For the most part these methods of precursor delivery have resulted in the synthesis of metal-oxide products composed of aggregates formed of tightly bonded primary particles (mostly spheroidal). Powders composed of agglomerates are usually formed from the fumed aggregates during their final production.



**Fig. 2.** Schematics showing different approaches utilized in the flame synthesis of TMOs. (a) Evolution of metal oxide nanoparticles as the base materials is introduced into a reaction zone using “Aerosol Methods” and “FSP” techniques; (b) “Solid Support” synthesis of 1D/3D TMOs; (b1-b2) “Gas-phase” synthesis of TMOs and hybrid nanomaterials; (c) Synthesis of TMOs by direct oxidation of a TM in a post flame region.

It is anticipated that flames can also be used as an inexpensive viable alternative to produce complex nanostructured TMOs that are essential for the development of new technologies (i.e. 1D, 2D and 3D and of unique chemical structure). It has been shown that the “solid support” and “gas-phase” techniques can be used to directly generate multi-dimensional, hybrid and mixed TMOs in flames, **Fig. 2(b-c)**.

## 2.2 Flames as a Unique Fabrication Techniques to Produce TMO Nanoparticles

What makes flames attractive for the synthesis of NMs is the relatively inexpensive and single-step process. The rapid succession of heating and cooling during combustion creates materials with rich physical morphologies and composition.

### 2.2.1 *Flame synthesis of metal-oxide nanoparticles*

An important controlling parameter in the flame synthesis of TMOs is the manner in which a raw material (source or precursors) can be delivered into a flame environment. The products synthesized using flames can exhibit significantly different morphologies and, at times, varying chemical compositions from those of the introduced source or precursors.

#### 2.2.1.1 *“Aerosol” and “spray pyrolysis” methods*

**Table 3** highlights some works for the synthesis of TMOs in flames by introducing the source material into the reaction zone using “*aerosol*” and “*flame spray pyrolysis*” (FSP). The “*aerosol method*” is a gaseous delivery process where the precursor is vaporized in a bubbler or evaporator before being introduced into a flame medium, while in the FSP the raw material is introduced into the flame as a form of fine spray. Burner configuration and corresponding flame structure, type of fuel used, type of catalytic/source materials and method of delivery of the source material is evident in **Table 3**. A schematic of the representative “*morphology*” of the formed powders is also presented. It is interesting to note that these methods of precursor/source delivery have resulted in TMO powders composed mostly of spherical-like primary particles and their aggregates. The general conclusion is that some of the important parameters for determining the

morphological structure of the produced powders are: i) the concentration of precursor introduced into the flame. Not only can this parameter affect the flame structure itself, but frequency of particle collisions during synthesis can increase with an overloading of precursor vapor leading to a higher rate of agglomeration (usually undesirable); ii) the combined influence of residence time of the particles and the flame temperature. Flame temperature (directly influenced by fuel type and oxygen content) can affect the flame synthesis of the TMOs since fuel type and oxygen concentration can affect flame structure as well [144]. For instance, Jensen et al. [145] reported on the flame synthesis of both ZnO and Al<sub>2</sub>O<sub>3</sub> powders composed of nanoparticles using a premixed methane-air flame at atmospheric pressure. High purity zinc and aluminum precursors were introduced to the flame environment by employing an “*aerosol*” technique with nitrogen flow. The synthesized ZnO and Al<sub>2</sub>O<sub>3</sub> particles had diameters in the range of 25-40 nm and 7.1-8.8 nm producing surface areas of 27-43 m<sup>2</sup>/g and 184-229 m<sup>2</sup>/g, respectively. The particle diameter range was achieved by adjusting the flame temperature and precursor vapor pressure parameters. Stark et al. [146] also used the “*aerosol*” method in a methane-fueled co-flow diffusion flame for the synthesis of vanadia-titania oxide nanoparticles. The as-synthesized particles had diameters ranging from 10 to 50 nm and specific areas of 23-120 m<sup>2</sup>/g. Stark and co-authors have observed that an increase of the oxygen flow rate resulted in larger diameters and smaller specific areas. During the last decade extensive research efforts have been devoted to the synthesis of TMOs in flames via the “*flame spray pyrolysis*” method. Typical nano-powders created with this method are titania, MgAl<sub>2</sub>O<sub>4</sub>, gamma-Fe<sub>2</sub>O<sub>3</sub>, alumina, manganese oxide, and zirconia. For instance, Tani et al. [147] reported on the use of the “*flame spray pyrolysis*” method for synthesis of ZnO

nanoparticles using a co-flow premixed flame. The average particle diameter was controlled between 10 nm and 20 nm by the solution feed rate, and the particles exhibited highly crystalline wurtzite (hexagonal) structure. Zinc acrylate was dissolved in methanol to create the precursor solution, and methane and oxygen were used as the fuel and oxidizer, respectively. By increasing the precursor feed rate, the flame location was increased resulting in greater surface growth and larger diameter particles. Similarly, Qin et al. [148], reported the production of europium-doped yttrium silicate ( $\text{Y}_2\text{SiO}_5:\text{Eu}^{3+}$ ) nanophosphors. The experimental combustion system consisted of a co-flow methane/oxygen diffusion flame and an ultrasonic spray generator. As with other metal-oxide flame synthesis studies, the diameter of the particles increased as the precursor loading increased. Fennell et al. [149] utilized a fuel-lean, premixed, laminar flat-flame burner to synthesize highly crystalline MgO nanoparticles with narrow diameter distributions. The flame was formed by acetylene ( $\text{C}_2\text{H}_2$ ) and nitrogen/oxygen compositions. An aqueous solution of  $\text{MgCl}_2$  was nebulized as a fine spray and mixed with the fuel/oxidizer stream before combustion with a magnesium concentration of approximately 13 ppm. Memon et al. [150] study the growth of titanium oxide nanoparticles that are synthesized using a multi-element diffusion flame burner (MEDB). Argon and hydrogen or ethylene are used as the precursor carrier gas and oxygen and argon are used as the oxidizer in the MEDB. The tetraisopropyl titanate (TTIP) precursor, injected through a syringe pump, is heated to nearly  $180^\circ\text{C}$  to prevent condensation of the TTIP. The nanomaterials were collected on an aluminum plate, maintained at  $100^\circ\text{C}$ , downstream of the burner. When using the hydrogen/argon mix and the ethylene/argon mix as the carrier gas, the team reported the growth of pure anatase  $\text{TiO}_2$  nanoparticles and carbon-

coated TiO<sub>2</sub> nanoparticles, respectively. Height et al. [151] synthesized zinc oxide (ZnO) nanorods using a premixed flame formed with methane and oxygen, and by inserting the precursors using FSP method. The solvent precursor is fed through the nozzle using a syringe pump as oxygen sheath gas was concentrically introduced around the nozzle. Zinc naphthenate and toluene were combined to form the liquid precursor solution. With the help of a vacuum pump, the nanomaterials were collected on a water cooled glass fiber filter. The group reported that ZnO, displayed single-phase wurtzite structure when doped with indium, tin, and lithium.

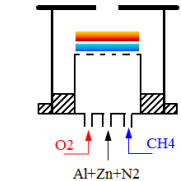

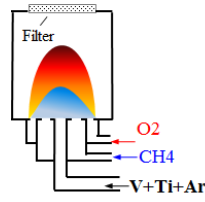

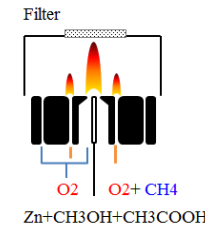

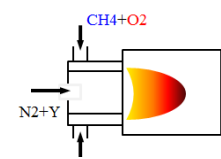

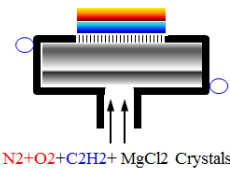

#### *2.2.1.2 Approaches used for controlled synthesis in “aerosol” and “FSP”*

As discussed earlier, conventional methods (i.e. CVD and plasma) can be combined to form a hybrid or combined system (plasma-enhanced CVD) to design or form novel types of TMOs. Similarly, in the application of flames for the synthesis of TMO nanoparticles some innovative processes (besides the popular precursor feed rate parameter) have been introduced as a means to control their formation. The ability to easily introduce many variables to fine tune/manipulate controlled synthesis makes flames a powerful method compared to the conventional methods. Some introduced variables include unique burner configurations, the simultaneous combination of two flame volumes, and the introduction of external forces such as electric fields, among others (**Table 3**). One interesting and frequently explored variable is the introduction of electric fields (EFs). This may be due to the successful early works of pioneers in this field revealing the effect of the change in flame geometry, velocity of flame gases, heat transfer rate, control of the particulate matter (flame luminosity) upon the introduction EFs [152- 156]. Therefore, those early EF flame works have provided unique tools for researchers in flame synthesis.

The very recent work of Li et al. presents an excellent review on the various techniques employed for controlling the flame synthesis of metal-oxide nanopowders to form structured films [157]. The Li et al. work presents a review of the flame aerosol deposition to form the TMO films and discusses the various deposition mechanisms for their formation. The introduction of external EFs in the flame synthesis of ceramics and TMOs has allowed for high precision control of the primary particle size, degree of the particle agglomeration (powder morphology) and crystallinity [158,159]. EFs formed using electrodes of various geometrical shapes (i.e. plate vs. needle shapes placed across the flame) and of various strengths have been tested in flames (diffusion and premixed) and have been revealed to be an excellent control variable in the manufacture of ceramics and TMOs [160,161]. EFs can be used to either increase or decrease the size of the primary particle [162,163]. As the particles are forming in the flame, they are charged by the EF and repel each other to prevent coagulation. Zhao et al. [164] studied the effect of EFs on controlling the nanoparticle size and level of agglomeration on titania nanoparticles. A flat-flame burner geometry was used with the fuel source (hydrogen), the oxidizer (oxygen), and the precursor vapor and carrier gas all being delivered as a premixed blend. The nanoparticles were collected thermophoretically on a cooled substrate downstream from the flame. The EF was established between the burner itself and the cooled substrate by a dual-polarity, high-voltage power source. Applying the EF allowed for the decrease of particle size from 40 nm to 18 nm without affecting any other material properties (e.g. crystallinity). Another innovative and creative approach is to introduce “*multi-nozzle*” flames that deal with the merging of flame volumes which has been proposed and developed in the flame synthesis of TMOs using the “*aerosol*” and “*flame spray pyrolysis*”

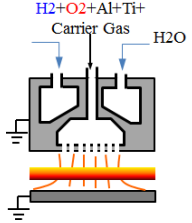

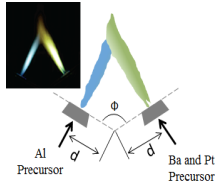

methods. For instance, Strobel et al. used a two-nozzle FSP for the single step preparation of Pt/Ba/Al<sub>2</sub>O<sub>3</sub> NMs [165]. In one of the flames, Al precursors were introduced while in the other barium/platinum was introduced resulting in individual crystalline Al<sub>2</sub>O<sub>3</sub> and BaCO<sub>3</sub> nanoparticles.

**Table 3.** Flame configurations and generated spheroidal nanoparticles.

Author	Burner Configuration	Flame Type	Fuel/Oxidizer	Reagent/Carrier Material and Delivery Method	TMO Structures
Jensen et al. [145]		Pre-mixed	CH <sub>4</sub> /O <sub>2</sub>	Zinc and aluminum acetyl-acetonates Aerosol - Nitrogen gas	 ZnO and Al <sub>2</sub> O <sub>3</sub> nanoparticles
Stark et al. [146]		Co-flow diffusion	CH <sub>4</sub> /O <sub>2</sub>	Vanadium and titanium alkoxides Aerosol - argon	 V <sub>2</sub> O <sub>5</sub> -TiO <sub>2</sub> nanoparticles
Tani et al. [147]		FSP pre-mixed	CH <sub>4</sub> /O <sub>2</sub>	Zinc acrylate FSP - 94% methanol + 6% acetic acid	 ZnO nanoparticles
Qin et al. [148]		Co-flow nano-premixed	CH <sub>4</sub> /O <sub>2</sub>	Tetraethyl orthosilicate, yttrium and europium nitrates FSP - Ethyl alcohol and nitrogen gas	 Y <sub>2</sub> SiO <sub>5</sub> :Eu <sup>3+</sup> nanophosphors
Fennell et al. [149]		Flat laminar pre-mixed	CH <sub>4</sub> /O <sub>2</sub> /N <sub>2</sub>	MgCl <sub>2</sub> aqueous solution FSP - nitrogen gas	 MgO nanoparticles

Wang et al. [170]		Premixed	$\text{CH}_4/\text{O}_2 + \text{N}_2$	Titanium tetraisopropoxide (TTIP)	 TiO <sub>2</sub> nanopowders
Chiang et al. [166]		Premixed	$\text{CH}_4/\text{O}_2 + \text{N}_2$	Copper nitrate, aqueous solution FSP method	 CuO nanoparticles
Ng et al. [167]		Premixed	$\text{CH}_4/\text{O}_2$	Vanadium Oxytriopropoxide FSP method	 V <sub>2</sub> O <sub>5</sub> nanoparticles
Pratsinis et al. [168]		Premixed	$\text{CH}_4/\text{O}_2$	Titanium tetraisopropoxide (TTIP) FSP/Aerosol	 TiOxide nanopowders
Kumfer et al. [169]		Inverse co-flow diffusion	$\text{C}_2\text{H}_4$ or $\text{CH}_4/\text{Ar} + \text{O}_2$	Iron Pentacarbonyl Aerosol	 FeO nanoparticles
Memon et al. [150]		Co-flow diffusion	$\text{H}_2$ or $\text{C}_2\text{H}_4/\text{Ar} + \text{O}_2$	Titanium tetraisopropoxide (TTIP) Aerosol	 TiO nanoparticles
Height et al. [151]		Premixed	$\text{CH}_4/\text{O}_2$	Zinc naphthenate FSP Method	 ZnOxide nanoparticles



Zhao et al. [164]		Axisymmetric flat pre-mixed	$H_2/O_2$	Titanium tetra-isopropoxide and aluminum tri-sec-butoxide FSP - fuel/oxidizer gas mixture	 TiO <sub>2</sub> nanoparticles
Strobel et al. [165]		Flame-spray pyrolysis	$CH_4/O_2$	Premixed co-flow flames	 Pt/Ba/Al <sub>2</sub> O <sub>3</sub> nanoparticles

It is reported that the inter-nozzle distance can be used as a variable to control the products in the two-nozzle synthesis. It is concluded that if the two flames come into contact later (tips region only) mixing of the two types of particles only agglomerate and do not sinter into a single particle as lower temperature prevails late in the flame [151]. The introduction of a swirler device inside a burner to tune/manipulate the flow dynamics and deposition of TMOs on a substrate is another interesting approach that was introduced by Wang et al. [170].

### 2.2.2 Flame synthesis of multi-dimensional TMOs using the “Solid Support” method

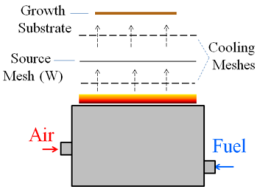

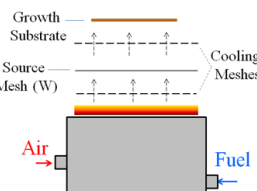

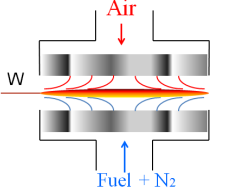

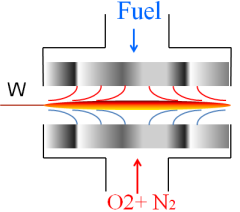
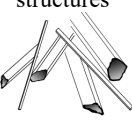
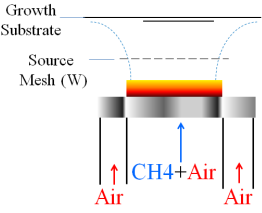
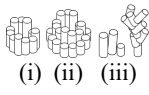
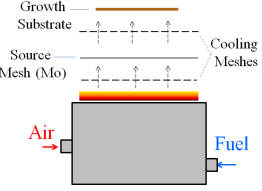
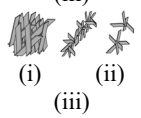
The introduction of the raw material in the highly oxidative environment of a flame in the form of high purity wires or meshes can yield TMOs of higher dimensional shapes. This method does not involve the introduction of catalysts or dopant vapors, but instead the raw material is introduced in the form of a solid substrate and we refer to it here as the “solid-support”. The wire/meshes can also serve as supporting surfaces, where structures are grown or recrystallized. The “solid support” method has been applied to the synthesis of various TMOs including Mo, W, Fe, Zn, and others as the base metals (**Table 4**). This method works very well for the synthesis of multi-dimensional shapes TMOs on solid

supports or directly in the flame medium [171- 183]. It is well understood now that the interaction of a transition metal wire (source material) with a highly oxidative environment containing O and OH radicals results in the rapid oxidation of the wire with the formation of metal oxides in high oxidation states in the form of layers on the surface of the probe (**Fig. 2b**). The layers are typically formed on one side of the probe, most likely the side exposed to the highly oxidative region of the flame. This is followed by the formation of metal oxide precursors originating from the oxide layers upon their vaporization or sublimation. The metal oxide precursors are transferred by the gas flow along the wire surface for their crystallization in colder regions in and/or out of the flame (on the same probe or other designed surfaces).

Some of the most popular parameters for selective design of the TMO morphology with multidimensional shapes in the “*solid support*” method are the geometry of the reactor used to form the flame medium, diameter size of probe, the ratio of introduced fuel to oxidizer, oxygen content in the oxidizer stream ( $O_2/N_2$ ), among others. **Table 4** presents a list of works on the flame synthesis of multi-dimensional TMOs using the “*solid support*” in a variety of flame configurations. The underlying growth mechanism of the TMO structures using the “*solid support*” in flames appears to be composed of multi and interrelated sub-mechanisms that occur continuously and nearly simultaneously. The first sub-mechanism is responsible for the conversion of the metal to metal oxide layers on the surface of the “*solid support*” upon its exposure to the flame volume. The second sub-mechanism is responsible for the melting/sublimation of the newly formed metal oxide layers into vapors or precursors. The third sub-mechanism is of a molecular level that deals with the nucleation and crystallization for the growth of the TMOs.

In “*solid support*” synthesis of multiple TMO nanostructures, multiple parameters are reported to impact the morphology and composition of the formed structures. Those parameters include: size of the solid metal source, residence time of the solid metal source in flame media, substrate position in flame media, oxygen concentration in flame environment, and source material (i.e. substrate). Similarly, some innovative approaches/processes that combine flames with sequential nonrelated flame processes have been developed for the formation of unique/modified TMOs. For instance, an innovative approach for the synthesis of TMOs in the form of composites has been developed by the Tse’s group [183]. In that contribution a two-step synthesis process (flame and electrodeposition) for the synthesis of tungsten-oxide/Al nanowires ( $WO_{2.9}/Al$  NWs) was employed. This is typically achieved in a sequential process with the first array composed of tungsten-oxide NWs formed using the “*solid support*” in a W probe inserted in a counterflow flame, followed by exposure to an ionic-liquid electrodeposition method containing an Al wire. This process has resulted in the flame synthesis of TMOs of higher dimensional shapes (see **Table 4**).

**Table 4.** Flame configuration and generated 1D and 3D TMO Nanostructures.

Author	Burner Configuration	Flame Type	Fuel/Oxidizer	Catalytic Material	Structure
Rao et al. [184]		Co-flow diffusion	CH <sub>4</sub> + H <sub>2</sub> /Air	Mesh (W)	Nanowires 
Rao et al. [173]		Co-flow diffusion	CH <sub>4</sub> + H <sub>2</sub> /Air	Mesh (Fe)	Nanowires 
Xu et al. [171]		Counter-flow diffusion	CH <sub>4</sub> /Air	Probe (W)	Nanowires 
Merchan-Merchan et al. [185]		Counter-flow diffusion	CH <sub>4</sub> + C <sub>2</sub> H <sub>2</sub> /O <sub>2</sub> +N <sub>2</sub>	Probe (W)	Hollow and semi-hollow large 3D structures 
Rao et al. [186]		Premixed	CH <sub>4</sub> /Air	Mesh (W)	
Cai et al. [187]		Co-flow diffusion	CH <sub>4</sub> + H <sub>2</sub> /Air	Mesh (Mo)	Single (i), branched (ii), flower-like (iii) 

Merchan-Merchan et al. [188]		Counter-flow diffusion	$\text{CH}_4 + \text{C}_2\text{H}_2/\text{O}_2 + \text{N}_2$	Probe (Mo)	Solid channels (i), hollow channels (ii), dendrite formation (iii) 
Merchan-Merchan et al. [189]		Counter-flow diffusion	$\text{CH}_4 + \text{C}_2\text{H}_2/\text{O}_2 + \text{N}_2$	Probe (Nb)	
Kathirvel et al. [190]		Premixed	$\text{C}_2\text{H}_2/\text{O}_2$	Metallic Zinc (Zn)	Nanorods 
Xu et al. [180]		Inverse co-flow diffusion	$\text{CH}_4/\text{Air}$	Probe (Zn)	Hexagonal nanowires 
Xu et al. [191]		Counter-flow diffusion	$\text{CH}_4/\text{Air}$	Probe (Zn)	Tower-like structure 
Dong et al. [192]		Hybrid Method (Solid support and electrodeposition) Counter-flow diffusion	$\text{CH}_4/\text{Air}$	Probe (W) Probe (Al)	Flame synthesis $\text{WO}_{2.9}$ $\text{WO}_{2.9} @ \text{Al}$ Electrodeposition $\text{WO}_{2.9} @ \text{Al}$ (Core-shell)

### 2.2.3 Volumetric flame synthesis of 1D and 3D TMOs

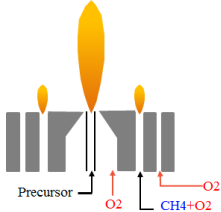
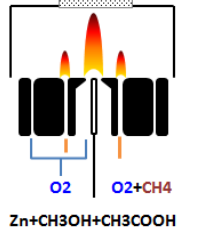
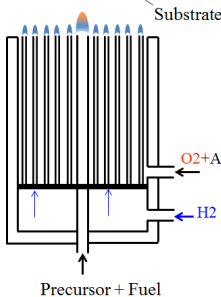
Gas-phase combustion synthesis has proved to be one of the most versatile and promising techniques employed for scale-up production of nanoscale materials [193,194]. Modern applications of TMOs require them to be of multidimensional shapes involving 1D (i.e., nanorods, nanowires, etc.), 2D (i.e., nanoribbons, nanosheets, nanoplatelets, etc.), and 3D (i.e., nanotrees, nanoforest, nanopolyhedrons, etc.) structures. Whether this becomes a reality will depend on the ability to design controllable synthesis methods for the generation of elongated objects with a high aspect ratio and at large scales. The ability to synthesize the structures directly in the gas-phase makes the flame a continuous single step process ideal for large scale production of the nanostructures. **Table 5** represents a list of works on the “*gas-phase*” synthesis of 1D and 3D TMO nanoforms using aerosol, FSP, and “*solid-support*” feed; these methods are discussed below:

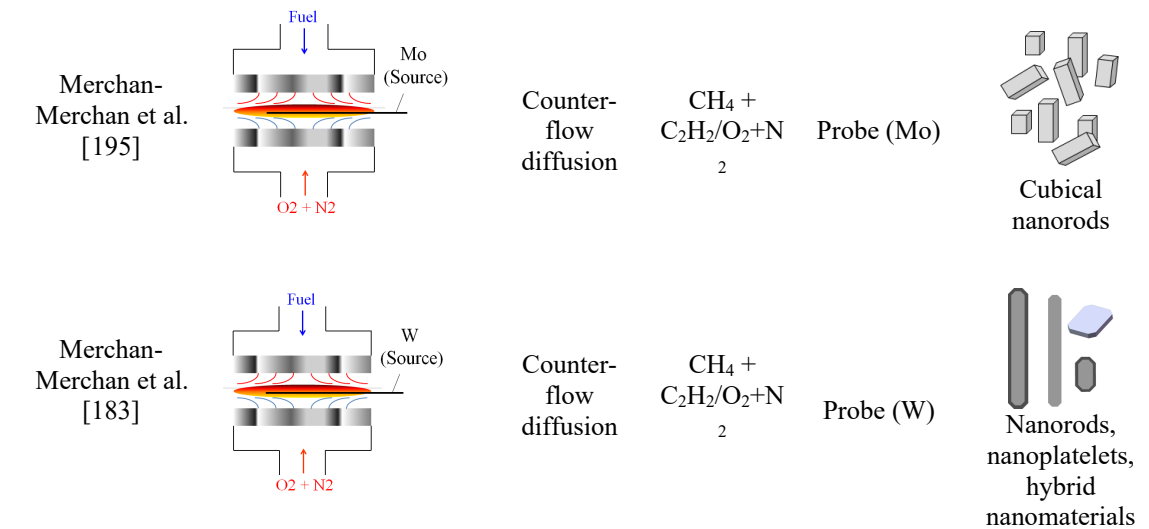
#### 2.2.3.1 TMOs (1D) formed using “*aerosol*” and “*spray pyrolysis*”

In some cases under certain conditions the “*aerosol method*” and “*flame spray pyrolysis*” has resulted in the synthesis of elongated TMOs. Height et al. reported that the introduction of tin and indium dopants in their FSP experiments altered the structures to form rod-like shapes (with closely controlled aspect ratio) as the concentration was elevated while the lithium dopant did not have an effect on the shape of the ZnO [137]. Furthermore, they reported that the specific surface area for the indium and tin doped ZnO materials increased as the dopant concentration was elevated. These materials are promising in sensing, electronics, and optical displays. Tani et al. [133] reported on the use of the flame spray pyrolysis method for the synthesis of ZnO nanoparticles using a co-flow premixed flame. By increasing the precursor feed rate, the flame location was increased

resulting in greater surface growth and larger diameter particles. The introduction of higher precursor feed rate resulted in elongated TMOs made of Zn. Memon et al. reported that the introduction of metal vapor precursors (aerosol) using hydrogen and ethylene as the carrier can result in the synthesis of non-spherical particles [136]. For the hydrogen mix, the group reported nanoparticles exhibiting a polyhedral shape with diameters ranging from 50-100 nm. For the ethylene mix, the group reported a carbon-coating thickness of approximately 3-5 nm [136].

**Table 5.** “Gas-Phase” Burner configurations for flame synthesis of 1D and 3D TMO nanostructures.

Author	Burner Configuration	Flame Type	Fuel/Oxidizer	Catalytic Material	Structure
Height et al. [151]		Co-flow premixed	CH <sub>4</sub> /O <sub>2</sub>	Toluene/zinc naphthenate solution, indium and tin dopants. FSP	ZnO nanorods
Tani et al. [147]		Pre-mixed	CH <sub>4</sub>	Zinc acrylate FSP - 94% methanol + 6% acetic acid FSP	ZnO nanoparticles
Memon et al. [150]		Co-flow diffusion	H <sub>2</sub> or C <sub>2</sub> H <sub>4</sub> /Ar + O <sub>2</sub>	Titanium tetraisopropoxide (TTIP) Aerosol	TiO nanoplatelets



### 2.2.3.2 Gas-phase flame synthesis of 1D and 3D TMOs

The “*solid support*” studies also lead to the flame gas-phase synthesis of 1D and 3D TMO nanostructures by the authors and others. During the “*solid support*” synthesis of TMOs it was noticed that the flame medium slightly changed color as the result of the insertion of the wire (source). One of the hypotheses was that the change in flame color was due to the rapid oxidation of the inserted probe at its surface. To prove this hypothesis TEM grids were inserted (thermophoretic sampling technique) in the flame volume at various distances from a W probe for potential sample collection. Indeed these experiments showed that when a Mo probe was inserted in the flame, Mo oxide structures of polygonal shape were formed directly in the gas-phase.

The presence of ultra-small crystals is observed close to the surface of the solid probe. Particle transformation occurs as the small crystals are pushed upstream in the direction of the fuel nozzle by the gas flow. Sampled material collected further away from the probe’s surface shows the presence of larger nanocrystals with the shape of cubes and rods.



The direct synthesis of the TMOs in the flame volume involves the oxidation of the solid wire to form various oxide layers on the surface of the probe exposed to the high temperature oxygen-rich region of the flame. Evaporation and/or sublimation of the oxides and their further transfer from the high temperature oxygen-rich region to the lower temperature fuel zone create an ideal environment for metal oxide synthesis. As the metal oxide vapor precursors travel in the gas flow, structures are crystallized in the form of elongated 1D nanorods and 3D nanorods octahedron nanoplatelets.

### **2.3 Core-shell and Mixed Transition Metal Oxide Nanostructures (MTMOs)**

The simple cross-linking of two transition metals with oxygen atoms or the combination of two transition metal oxides into a single compound (or a core-shell TMOs  $X@Y$ ) allows for the formation of an entirely new type of material. In recent years extensive research has been devoted to the study of these NMs revealing the unique properties and the potential applications in a broad-spectrum of sciences and engineering. *MTMO and core-shell TMOs* have shown to have superior chemical, piezoelectric, optical, electrochromic, and photochromic properties and are essential components for the development of new state-of-the-art technologies (ranging from catalysis, LIBs, smart windows, medical and biomedical applications, among others) that stem from the superior properties that they exhibit [196- 201]. However, the development of these new technologies is greatly hampered by the high cost of production of the NMs. For instance, Jiang et al., [202] reported an overview of the latest developments in metal oxide-based electrode architectures for electrochemical energy storage applications with a focus on lithium-ion batteries (LIBs). The authors concluded that the key to satisfy the requirements

of future power sources consist of developing advanced designs and simple fabrication methods of nanostructured films/arrays of hybrid electrodes [202]. Therefore, a continuous and facile method for the production of these novel nanomaterials is needed. The ideal method should be able to produce the *NMs* at a high rate with controllable composition, nanosizes, crystallinity, shape, structure and morphological characteristics. Therefore, the development of a method to generate such structures that is facile, inexpensive, with a fast growth rate will impact whether these new technologies become commercially viable in the future. Various synthesis methods including chemical vapor deposition (CVD) [203, 204]; sol-gel method [205]; and plasma [206,207] have been used for the synthesis of mixed Mo-W oxides. CVD and the sol-gel methods are currently considered the “ideal methods” for the synthesis of MTMOs. Both CVD and sol-gel are composed of multi-step processes. Both methods initially require the pyrolytic decomposition of the metal/alkoxide precursors. The sol-gel method requires a time intensive ultrasonic bath to achieve homogenous mixing of the solution containing the pyrolytic decomposed precursors. In the same process an extensive “aging process” is required (~24hrs). Both methods require extensive deposition time and annealing in the final stage. As an example of the multi-steps process that these conventional techniques employed, Gesheva et al. [203] demonstrated the use of the CVD technique for synthesizing tungsten/molybdenum-oxide films for electrochromic applications. The synthesis process involved pyrolytic decomposition of hexacarbonyls for each metal source, Mo(CO)<sub>6</sub> and W(CO)<sub>6</sub>, at a 1:4 ratio, respectively. The mixed metal oxide films were deposited by mixing the precursors at 90 °C with a constant supply of Ar loaded with precursor vapors, followed by the separate introduction of O<sub>2</sub> gas at an Ar to O<sub>2</sub> ratio of 1:32. The deposition process occurred at 200 °C for 40

min, resulting in different growth rates or film thicknesses, followed by an annealing process in air between 400 to 500 °C for an additional hour to complete the synthesis.

### 2.3.1 *Flame synthesis of core-shell and MTMOs on solid substrates*

**Table 6** lists important works on the flame synthesis of MTMOs and core-shell TMOs using different types of flame configuration and techniques. Some of these methods are hybrid that allow for the combination of different deposition processes of the vapors [208,166]. The process includes “*flame vapor deposition*”, “*solid diffusion growth*” or a combination of the two to grow 1D binary metal oxide and complex core-shell TMO nanostructures [201]. In the “*solid diffusion growth*” process some areas of the substrate serve as the metal source. This process requires the flame to rapidly heat the metal. This causes the metal atoms to diffuse toward the surface of the source material and become oxidized by the flame, forming metal oxide nanostructures on the original substrate. The “*flame vapor deposition*” process for the synthesis of MTMOs as described by Cai et al. encompasses: i) the flame oxidizes the surface of the metal (e.g., Mo mesh); ii) the newly formed metal oxide sublimates to form vapors; and iii) the metal oxide vapors condense onto colder growth substrates, placed further down the flame front, in the form of 1D NMs. A multi-step process called “*Sequential solid-vapor growth*” was used to generate nano TMOs of a core-shell structure. The “*Sequential solid-vapor growth*” combines both the “*flame vapor deposition*” and “*solid diffusion growth*” to form the complex metal oxide nanostructures. In the Cai et al. contribution, copper oxide (CuO) nanowires were formed first by the process of “*solid diffusion growth*” on the surface of a Cu substrate. The newly grown CuO nanowires serve as nano substrates to be used in the “*flame vapor deposition*” of a 4 cm x 4 cm, 99% purity Mo wire mesh (0.318 cm wire spacing and 0.064 cm wire

diameter). MoO vapors are deposited on the already formed CuO nanowires, coating them with MoO<sub>3</sub> in the form of solid shells or branches. It was reported that the morphology of the metal oxide nanostructures was dependent on the MoO<sub>x</sub> vapor concentration, growth substrate temperature and the time of growth. When T<sub>Mo</sub> and T<sub>Cu</sub> are maintained at 480 °C and 420 °C, respectively, for 10 minutes with a 0.5 fuel to oxygen ratio, MoO<sub>3</sub> is deposited evenly around the already grown CuO nanowires. For complex metal oxide nanostructures to occur, the growth rate for the creation of both oxides (e.g. MoO and CuO) needs to be similar. This can be difficult since “*flame vapor deposition*” method has a much faster growth rate than the “*solid diffusion growth*” method. Therefore, the Cu substrate is kept at a temperature at which the nanostructure growth is fastest (~500 °C) and Mo mesh wire was maintained at a temperature resulting in low MoO<sub>x</sub> vapor concentration, where the fuel (CH<sub>4</sub> and H<sub>2</sub>) to oxidizer (air) equivalence ratio was 0.53 and the Mo source mesh was ~550 °C. The temperatures of the meshes are achieved by the use of heat sinks in the form of plain steel cooling meshes. The cooling meshes are placed between the flame and the source mesh as well as between the source mesh and the growth substrate as needed for temperature control.

Cai et al. [210] also used the simultaneous “*vapor-vapor deposition*” method to synthesize 1D complex W-doped MoO<sub>3</sub> nanoflower-like structures. This flame synthesis process requires the simultaneous oxidation of two source materials and their deposition on the surface of a substrate placed further downstream. The simultaneous “*vapor-vapor deposition*” process involves the use of two different transition metals (i.e. Mo and W), which are placed in the post-flame region. The metals are then oxidized by the flame, producing metal oxide vapors by means of sublimation. The sublimated vapors formed,

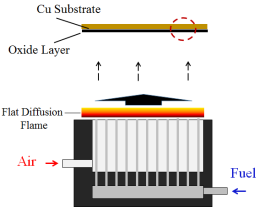
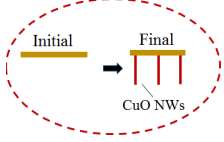
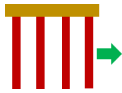
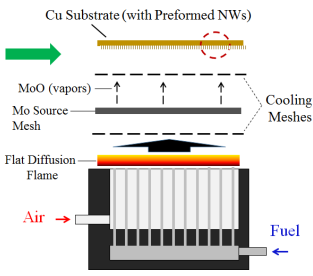
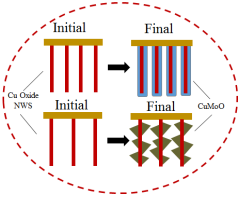
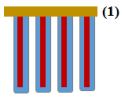
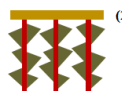
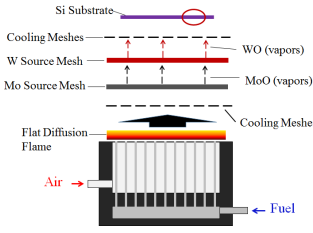
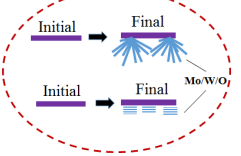


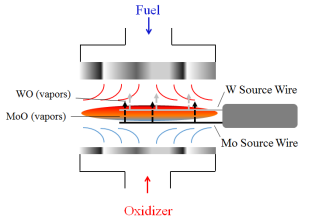

WO<sub>x</sub> and MoO<sub>x</sub>, then move with the gas flow toward a silicon (Si) substrate placed further downstream. Complex W-Mo-O nanostructures are formed when the vapors condense and deposit on the colder Si substrate. To form mixed metal oxides instead of separate binary oxides, it is necessary to ensure that the nucleation and growth rates of both metals are similar.. The structure of the complex metal oxides is found to be dependent on the temperature of the growth substrate. W and Mo mesh wire temperatures were kept relatively constant, using the steel cooling meshes, at around ~670 and ~560 °C respectively. When the vapor concentrations and substrate temperature (~351 °C) were comparatively low, square and hexagonal nanoplates of average area 1 μm were formed on the Si substrate after 20 minutes. To obtain a low vapor concentration the fuel to oxidizer equivalence ratio was set at 0.8 and the temperature of the metals was ~667 °C for the W mesh and ~558 °C for the Mo mesh. These nanoplates had layer structures indicating the nanostructures contained evenly dispersed Mo and W. The atomic ratios of Mo to W were estimated to be 22:1. Most of the complex metal oxides formed have a crystal structure similar to the one found in α-MoO<sub>3</sub>, and ultimately the W-Mo-O complex oxide nanoplatelets are likely made of tungsten-doped MoO<sub>3</sub>.

### ***2.3.2 Synthesis of MTMOs and related core-shell nanostructures using “flame spray pyrolysis”***

As was noted in the previous sections of this contribution, flame aerosol synthesized products are strongly dependent on the state in which the precursor is fed into the flame medium. This basic principle was employed by Stark et al. in flame spray pyrolysis to selectively synthesize ceria-oxide and ceria/zirconia mixed nanocrystals of a high specific surface area and improved thermal stability [204]. It was reported that the

introduction of Ce (FSP) using isooctane/acetic acid/2-butanol carrier resulted in large CeO<sub>2</sub> structures of a polydisperse size distribution [209].

**Table 6.** Flame generated core-shell and mixed metal oxide nanostructures.

Author	Burner Configuration	Method of Growth	Fuel/ Oxidizer	Flame Type	Structure
Cai et al. [210]		<p>Solid Diffusion</p> 	CH <sub>4</sub> + H <sub>2</sub> / Air	Co-flow diffusion	 <p>Cu Oxide nanowires</p>
		<p>Sequential Solid-Vapor</p> 	CH <sub>4</sub> + H <sub>2</sub> / Air	Co-flow diffusion	 <p>(1)</p>  <p>(2)</p> <p>(1) Core-shell NWs; (2) NWs with branches</p>
Cai et al. [210]		<p>Vapor-Vapor</p> 	CH <sub>4</sub> + H <sub>2</sub> / Air	Co-flow diffusion	 <p>(1)</p>  <p>(2)</p> <p>W-Doped MoO<sub>3</sub>: (1)- nanoflow- ers and (2)- platelets like structures</p>
Farmahani et al. [211,212]		<p>Gas-Phase</p>	CH <sub>4</sub> + C <sub>2</sub> H <sub>2</sub> / O <sub>2</sub> + N <sub>2</sub>	Counter- flow diffusion	 <p>W-doped MoO<sub>3</sub> nanocubes</p>

Stark et al (Maddler) [213]		Flame-Spray Pyrolysis	CH <sub>4</sub> / O <sub>2</sub> + N <sub>2</sub>	Air- assisted nozzle with flamelets	 Ce <sub>0.5</sub> Zr <sub>0.5</sub> O <sub>2</sub>
Ismail et al. (Memon) [214]		Flame-Spray Pyrolysis	H <sub>2</sub> / O <sub>2</sub> + Ar	Diffusion flame and flamelets	 C-TiO <sub>2</sub> , Fe/C-TiO <sub>2</sub> , V-TiO <sub>2</sub>
Zhang et al. [215] (Axelbaum)		Flame Assisted Spray Technology (FAST)	MeOH+H <sub>2</sub> / Air	Co-flow diffusion	 LiMn 0.5Ni <sub>1.5</sub> O <sub>4</sub>

Zhang et al. employed the flame assisted spray technology (FAST) that allowed for the continuous production of nanostructured LiNi<sub>0.5</sub>Mn<sub>1.5</sub>O<sub>4</sub> with an outstanding average particle of 16 nm [206]. The MTMOs appear to be consisting of powders composed of spherical-like primary particles. Of interest are the wide ranges of particle size that exist in the powder; that is, the particle diameter ranges from the micro to the nanoscale. It is reported that the spinel structures are valuable materials for energy applications.

### 2.3.3 *Gas-phase synthesis of MTMOs*

Recently, using a counter-flow diffusion flame our group showed that MTMO nanopolyhedrals made of W-doped MoO<sub>3</sub> can be synthesized directly in the gas-phase [216,217]. High purity molybdenum and tungsten probes, 1 mm in diameter, are introduced simultaneously into the oxygen-rich zone flame as the material source. The process starts with the formation of Mo Oxide and W oxide vapors in a region of the flame, initial crystallization of the vapors into shapeless particles in an intermediate flame zone, and ending with the transformation/combination into well-developed cubes (W-doped MoO<sub>3</sub>) in another region of the flame. The process takes place as flame gases move in the direction of the stagnation plane. The underlying mechanism is as follows: (i) the high temperature flame causes fast formation and sublimation of molybdenum oxides from the surface of the Mo wire, (ii) molybdenum oxide vapors cool down and nucleate to form shapeless particles that are transformed to nanocubes as they travel inside the flame volume; (iii) tungsten oxides evaporated from the tungsten probe deposit on the surface of existing MoO<sub>3</sub> nanocubes and form chain-like tails attached to the nanocubes, (iv) chain-like tails diffuse into the nanocubes and elemental tungsten intercalate into layers of nanocubes; (v) as nanocubes are transported inside the flame, W atoms distribute evenly inside the structures and increase the lattice spacing of the existing nanocubes. However, the nanocubes maintain crystalline structure.



### 3. CHAPTER 3—RESEARCH OBJECTIVES

---

This chapter defines the core objectives of this dissertation and sets the foundation to assess the impact of this research.

#### 3.1 Thesis Objectives

In the past decades, research in flame synthesis of micron and nanosized structures has taken this method to a new level. Flame synthesis is shown to be a scalable single step process, with high growth rates, optimum control over the morphology, growth flexibility (i.e. gas-phase and/or solid support), and is therefore an economical technology [218, 219] for producing controlled single and metal-oxide nanoscale heterostructures [220, 221, 222, 223, 224]. In this study a reactor with the counter-flow configuration is employed for investigating the synthesis of TMOs. The flame counter-flow flame structure depends on the gas velocities (strain rates), oxygen content in the oxidizer, fuel type, among other parameters.

The main purpose of this study consists of showing the flexibility of flame media as a rapid and single step process for the synthesis of TMO nanostructures. Secondly, gaining a fundamental understanding of the synthesis mechanism of complex structures such as, hybrid, heterogeneous, and multi-dimensional structures on both the solid support and the gas-phase synthesis media is of key interest of this work. It is hypothesized that:

- (i) When metal probes are introduced into oxygen-rich flames with strong temperature gradients, the metal atoms react with the oxygen species in the flame, resulting in the formation of metal oxide compound films on the surface of the metal probes.
- (ii) The metal oxide layer is then evaporated or sublimated to form metal oxide vapors.

(iii) The oxide vapors are then carried by the gas flow downstream in the direction of the stagnation plane and are deposited on the upper surface (or fuel side) of the probe/substrate with lower temperatures which promotes crystallization of the oxide vapors to form the crystals.

Gaining further understanding of the effect of flame dynamics (i.e. residence time, temperature, chemical species, fuel and oxidizer ratios, etc.), along with crystallization kinetics will certainly enhance our knowledge on solid support and gas-phase synthesis of single and hybrid TMO nanostructures with complex morphologies. Ultimately, our hypothesis is supported by validating the principal research objectives of this dissertation. The principal components of this research involve:

1. To provide a well searched background on the high flexibility of flames as scale-up method or commercial production for the synthesis TMO structures (i.e. typically spherical and micron size structures). Hence, highlighting how the “legacy flame processes” have evolved for the synthesis of high-purity production of several types of well-defined TMO nanostructures with a multiplicity of morphologies.
2. To illustrate how the combination of a 1D diffusion oxygen-rich flame with the introduction of solid support (i.e. material source) can result on an ideal process/method for the synthesis of a new generation of nanocrystalline TMOs.
3. To comprehend the fundamental mechanism involved in the solid support-based growth of single transition metal oxide nanostructures and mixed transition metal oxide (MTMO) structures, which exhibit complex morphologies. The growth of both Mo and W probes will be investigated as examples of material sources for the synthesis of single and MTMO nanoscale structures. By understanding the growth mechanisms, it

- is possible to apply this knowledge to various transition metals in the periodic table, resulting in tailored physico-chemical properties of the synthesized nanoscale materials, achieved by combining transition metals with complementary properties.
4. To gain further insight into the physical and chemical properties of the synthesized nanoscale materials to support the proposed growth mechanisms.
  5. The ultimate outcome of this work consists of gaining new knowledge in the application of oxygen-rich flames for the synthesis of complex MTMO nanostructures with unique properties and morphologies suitable for a wide range of applications.

### **3.2 Research Impact**

This investigation is focused on gaining detailed understanding on the synthesis and growing mechanism of complex TMO heterostructures both on the solid support and in the gas-phase employing a counter-flow oxygen-enriched diffusion flame. The attained understanding of how complex structures with tailored morphologies sets the foundation to enable mass production of these structures for optimizing their properties and allowing their wide range of novel applications. Several contributions will be made from these research project:

- The significance of the physico-chemical interactions between the 1D counter-flow diffusion flame and the metallic probe substrates. These interactions favor the oxidation of the metallic probes, followed by the formation oxide vapors that act as precursors of highly crystalline structures.
- The importance of synthesizing complex and hybrid heterostructures composed of at least two metals to enable significant performance improvements on the

end-structure due to counterbalancing the shortcomings and optimizing the advantages of the individual components.

- The ability of flames to fabricate nano- and micron-sized structures with a multiplicity of morphologies based on flame position of the metal substrates, short residence times (<150 sec), and azimuthal crystallization sites for deposition.
- Optimum understanding of the growth mechanism of the structures with complex morphologies (core/shell, grass, flower, tree, forest, polyhedron, etc.) as a result of the interaction of the metal probes with the highly oxidative flame environment.

## 4. CHAPTER 4—EXPERIMENTAL SETUP AND PROCEDURE

---

The purpose of this chapter is to present the details of the experimental setup and procedures used to enable the synthesis of complex heterostructures. The chapter comprises of four main parts including: (i) details of the counterflow combustion reactor; (ii) details of the mechanism/procedure used for the probe insertion or bulk material source into the flame medium; (iii) sample preparation used for both scanning electron microscopy (SEM) and transmission electron microscopy (TEM) analyses after the structures are synthesized in the flame; (iv) key features of the counter-flow diffusion flame along with the numerical predictions of the major chemical species and the temperature profile distribution.

### 4.1 Experimental Setup of the Counterflow Reactor

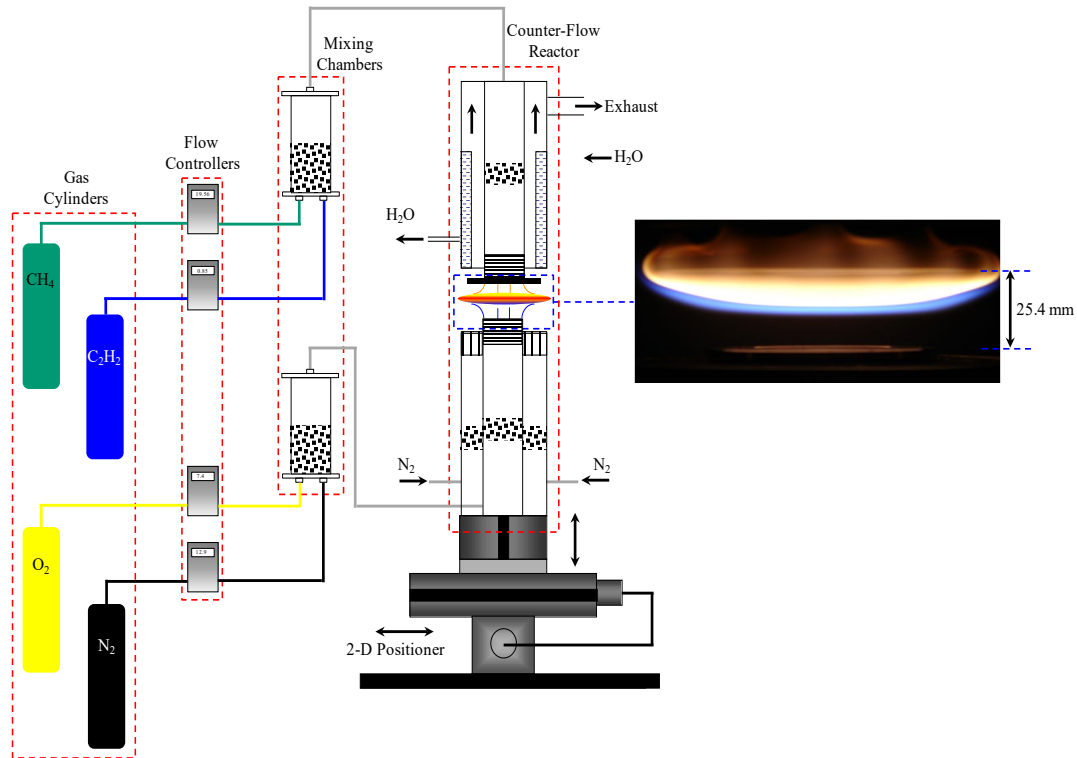
A schematic of the experimental setup is shown in **Fig. 3**. Two opposite streams of gases are introduced in a counter-flow diffusion flame combustion reactor; the fuel (methane seeded with acetylene) is inserted from the top nozzle and the oxidizer (oxygen/nitrogen) is supplied from the bottom nozzle. The fuel and the oxidizer nozzle have inside diameters of 42 mm and they are 25.4 mm apart. A cylindrical annular duct around the oxidizer nozzle is employed to introduce co-flowing nitrogen with various purposes such as extinguishing the flame near the outer jacket and preventing it from dissipation into the environment, and it also creates a protective shield around the flame that serves as a stabilization mechanism that helps protect the flame from disturbances in the surrounding environment. This plays a key role in the stabilization process of the flame

considering that small disturbances, such as a person moving close to the burner position, can result in flame instabilities due to the low fuel and oxidizer streams flows, ~20 lpm. The nitrogen duct has inner and outer diameters of 60 and 108 mm, respectively. The nitrogen flowrate varies based on the strain rate (e.g. for strain rates of 20 and 30 s<sup>-1</sup>, the N<sub>2</sub> flowrate is 96.70 and 145 l/min, respectively).

The fuel and the oxidizer streams impinge against each other creating a stable stagnation plane. The flame front is formed on the oxidizer side with respect to the stagnation flame. Methane (CH<sub>4</sub>) seeded with 4% by volume of acetylene (C<sub>2</sub>H<sub>2</sub>) were employed as the fuel in this work; whereas the oxidizer is composed of 50% by volume of oxygen (O<sub>2</sub>) and 50% by volume of nitrogen (N<sub>2</sub>). It is important to mention that the addition of C<sub>2</sub>H<sub>2</sub> in the fuel stream increases the flame temperature and affects the growth rate of metal oxide structures. The oxygen content can be varied in some cases in order to study its influence over the synthesized material.

The flows of all the gases were metered with Aalborg electronic mass flow controllers which have accuracies within 1.5% and are located upstream of the burner nozzles (**Fig. 4**). Mixing chambers are located downstream the flow controllers in the respective top/bottom sections of the burner for the fuel and the oxidizer streams, respectively, as depicted in **Fig. 4**. These chambers have the function of guaranteeing a well mixture of the respective gasses, CH<sub>4</sub>/C<sub>2</sub>H<sub>2</sub> and O<sub>2</sub>/N<sub>2</sub>. The chambers are metallic cylinders with one and two outlet nozzles on the top and on the bottom, respectively. These

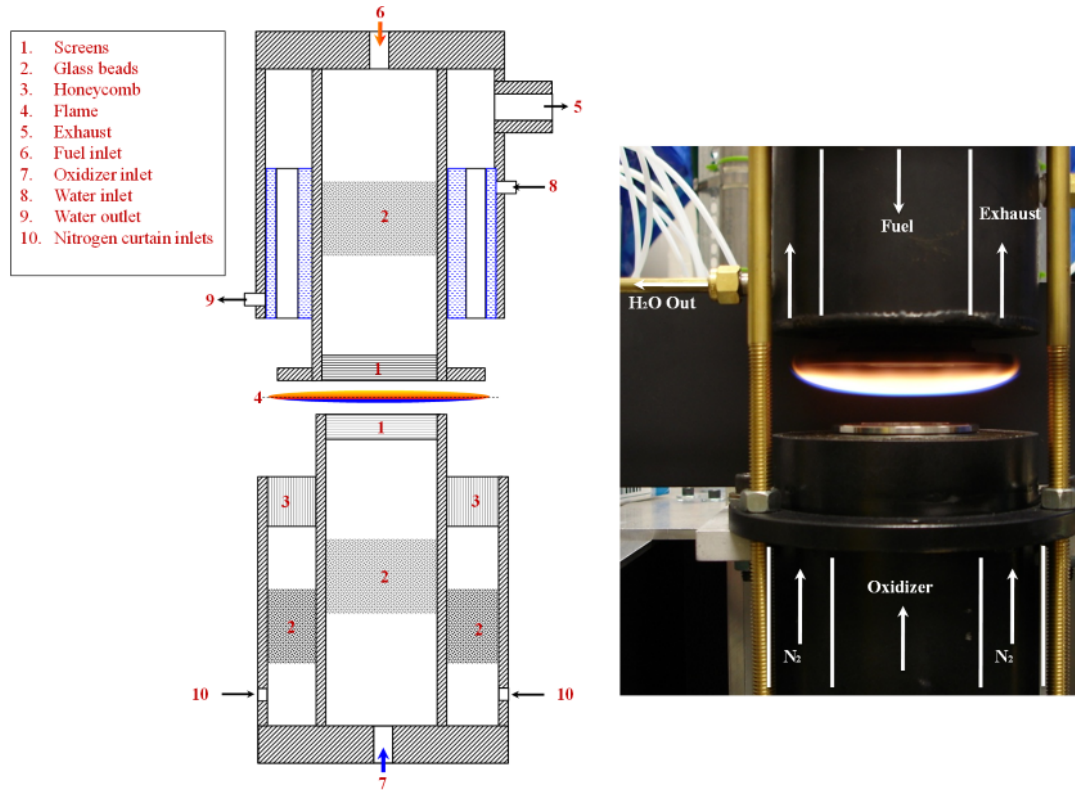
metallic cylinders are half-filled with 3-mm diameter glass beads in order to further improve and distribute the gases flow in the mixing process.



**Fig. 3.** Schematic of the experimental facility. The gas flows are measured and regulated by mass flow controllers, then the fuel and oxidizer mixing process takes place in their respective mixing chambers. The fuel mixture is introduced from the top nozzle and the oxidizer mixture is supplied from the bottom nozzle. The photograph represents a regular counter-flow diffusion flame.

**Fig. 4** illustrates a schematic of the cross-sectional view of the counter flow diffusion burner and the various components employed to further benefit the flame stabilization process. Several stainless-steel screens are positioned in the fuel and oxidizer nozzles exits, and a honeycomb plate is placed in the annular nitrogen duct. These devices are employed to stabilize the flow through the top and bottom nozzles. A cooling system with water as the permanent flowing work fluid is included in the upper nozzle aiming to dissipate heat from the exhaust gases preventing failure of the burner due to overheating.

A photograph of the counter-flow burner, along with a typical diffusion flame and the direction of the respective flows, is shown in the insert of **Fig. 4**.



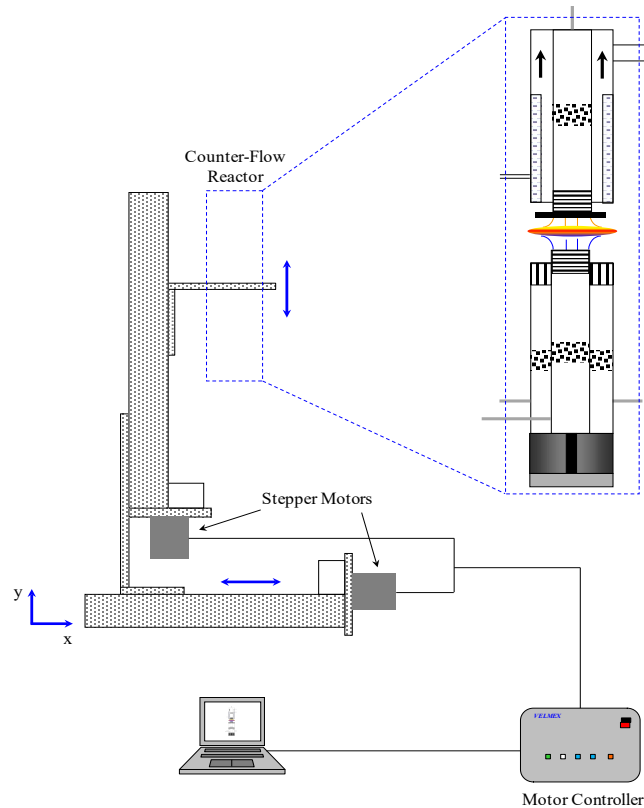
**Fig. 4.** Schematic of the cross-sectional view of the counter-flow combustion reactor. The inset represents a photograph of the actual combustion reactor and the counter-flow diffusion flame.

#### 4.1.1 Counter-flow reactor positioning system

The entire combustion reactor was placed on a 2-D stepping motor positioning system, driven by UniSlide Velmex MA 6000 units, in order to achieve precise positioning of the reactor and the metallic probe within the reactor. A personal computer data acquisition system was connected to the stepper motors to control the operation of the positioning system, therefore, governing the position of the metallic probe inside the flame



environment. The interface COSMOS V3.1.4 (Computer Optimized Stepper Motor Operating System) was used as the data acquisition software, which allowed precise positioning within fractions of a millimeter (0.0000625 inches). The system has a variable velocity of 0 to 0.20 inches/second. This allowed the probes to be accurately inserted into the flame at a specified Z location. A schematic of the positioning system utilized in this investigation is illustrated in **Fig. 5**.



**Fig. 5.** Schematic of the 2-D stepping motor positioning system. The stepper motors are controlled through the control box by the personal computer.

## 4.2 Counter-flow Diffusion Flame Structure

1D characteristics and easily variable residence time within the flame are two main factors that make flames fed by opposing jets of fuel and oxidizer an interesting

area of fundamental research. Both experiments and calculations are much more workable owing to 1D features of the counter-flow flame.

It is important to highlight that the diffusion flame created by the counter-flow combustion reactor is always established between the nozzles and it is essentially flat, with a disc-like geometry, having dependencies only in the axial direction. The flame has two very unique zones. The flame has a strong transition from blue in the oxidizer side, oxygen-rich area, to bright yellow in the fuel side, hydrocarbon rich area (photograph of the flame in **Fig. 4**). The soot particle radiation gives the yellow color to the flame and is also responsible for the flame brightness. Strong temperature and chemical species composition gradients along with the counter-flow diffusion flame features discussed above make this type of flames an ideal synthesis medium for both CNTs and TMOs. The production capability of several types of materials greatly adds flexibility to any process developed with this type of flame.

Another neat characteristic of this flame corresponds to the ability of controlling the two characteristics zones only by modifying the oxygen content in the oxidizer stream and the gas velocities.

#### ***4.2.1 Structural response of counter-flow diffusion flame to strain rate modifications***

The counter-flow diffusion flame is characterized by a local strain rate,  $SR$ , obtained by fitting a straight line to the computed approximate velocity profile just upstream of the thermal mixing layer at the oxidizer side, and it is defined as half of the negative of the axial velocity gradient [225]. The local strain rate is inversely proportional

to the residence time of the reacting species in the reaction zone. Strain rate represents a key parameter that plays an important role in regulating the counter-flow flame structure. The flame cannot be sustained if the strain rate is too high or too small [226]. The global strain rate is defined as:

$$SR = \frac{2V_g}{L}$$

where the parameter  $V$  denotes the velocity of the reactant streams at the nozzle boundaries,  $L$  represents the separation of the nozzles and the subscript  $g$  symbolizes the gases stream. It should be noted that both the oxidizer and the fuel stream have the same velocity.

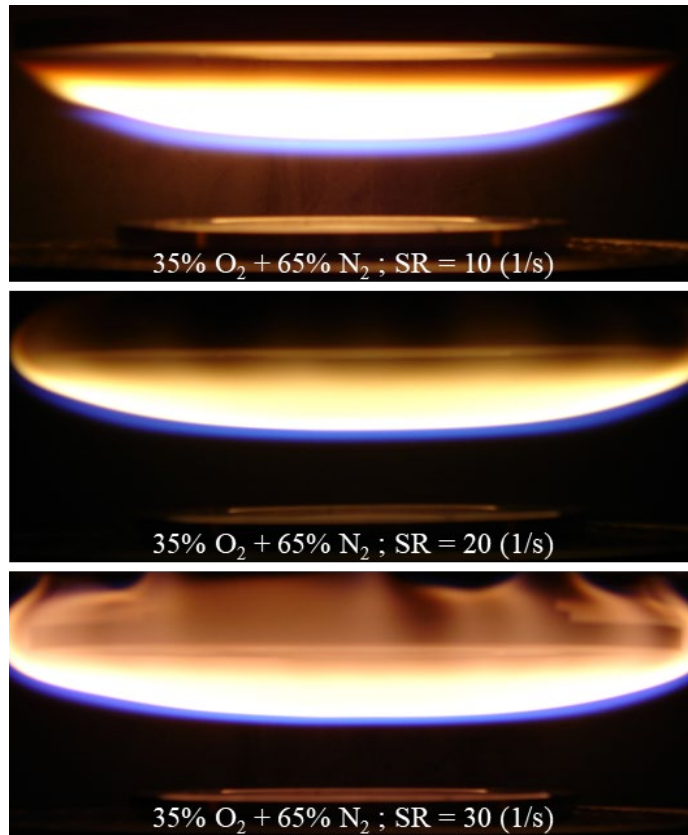
**Fig. 6** shows several photographs of counter-flow diffusion flames with a constant oxidizer concentration of 35% O<sub>2</sub> and 65% of N<sub>2</sub> and strain rates ranging from 10 to 40 s<sup>-1</sup>, this was accomplished by changing the outlet flow velocities and the nozzles' separation distance. The counter-flow diffusion flame structure is strongly influenced by modifying the strain rate, for instance, the brightness of the yellow zone of the flame decreases as going from strain rates of 10 s<sup>-1</sup> to 40 s<sup>-1</sup>. These photographs reveal that the brightest yellow zone of the flame takes place when the strain rate is 10 s<sup>-1</sup> and it is also interesting to note that this zone becomes weaker with higher strain rates, **Fig. 6**. For lower stream velocities at the nozzles' boundaries, more time is available for pyrolysis processes as a result of longer residence times of the particles inside the flame, which will later aid to increase the soot concentration in the flame medium. The blue zone is also affected by changing the strain rate, it can be clearly observed from **Fig. 6** that the blue zone becomes substantially narrower and less active when increasing the strain rate. The flame thickness is reduced by increasing the strain rate; likewise, the thickness of the characteristics zones of the

flame, yellow and blue, are also reduced. **Table 7** and **Fig. 7** show the measurements performed using ImageJ software (a public domain image processing program developed by the National Institutes of Health) on the flame photographs referencing the known distances between the nozzles with an accuracy of 0.01 mm. Results show how the flame yellow and blue zone thicknesses are reduced from 14.91 mm to 12.50 mm, 12.22 mm to 11.21 mm, and 2.69 mm to 1.29 mm, respectively, as going from a strain rate of 10 to 40  $s^{-1}$ . Sung and coworkers also studied the structural response of counter-flow diffusion flames to strain rate variations and they found that both experimental and computational analyses reveals that diffusion flame structures become thinner with increasing strain rate, with its thermal thickness roughly proportional to  $1/\sqrt{SR}$  [225]. Sung's studies strongly agree with the results presented herein.

#### ***4.2.2 Structural response of counter-flow diffusion flame to oxygen concentration variations***

The counter-flow combustion reactor has the capability not only of changing the strain rates but also has the ability of varying the oxidizer gas mixture ratio. This adds substantial flexibility to this reactor by creating strong temperature and chemical components gradients. A constant strain rate of 20  $s^{-1}$  was employed for both the fuel and oxidizer streams in order to study the flame response to the variation of the oxidizer oxygen content from 21% to 100%, **Fig. 9**. It is clearly observed that the air-based flame (21%  $O_2$ ) has a considerably thinner blue zone compared to the flames with higher oxygen contents; moreover, this air-based flame does not curl around the fuel nozzle plate. On the other hand, when the oxygen content was increased to 100%  $O_2$  the blue zone is much thicker, more active and the flame visibly curl around the upper disc of the combustion reactor

owing to the suction of the exhaust system. With oxygen enrichment the flame is compressed decreasing the overall flame thickness (**Table 8** and **Fig. 8**). The curves in **Fig. 8** confirm that the flame overall thickness decreases, whereas the blue zone thicknesses is increased by increasing the oxygen content in the oxidizer stream. On the other hand, the yellow zone thickness is reduced by increasing the oxygen content. As the oxygen enrichment increases, the maximum temperature and the stagnation planes are moved toward the fuel side, and the distance between them decreases; furthermore, the high temperature region is much wider compared to the air case and the pyrolysis is improved considerably [227]. The 50% oxygen flame has ideal features that make it suitable for synthesis of TMOs considering its highly-stability and strong gradient of temperature and chemical species characteristics. This particular flame lies in between the two extreme conditions explained above.

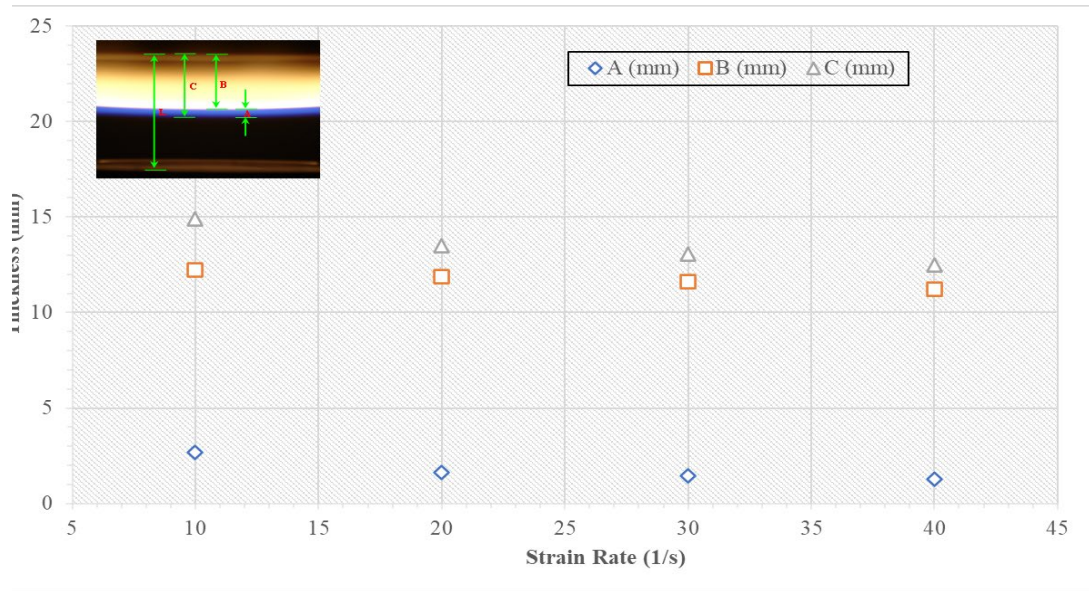


**Fig. 6.** Counter-flow diffusion flame photographs with oxidizer concentration of 35% O<sub>2</sub> + 65% N<sub>2</sub> formed with various strain rates ranging from 10 s<sup>-1</sup> to 30 s<sup>-1</sup>. Increasing strain rates results in reduced flame zone thicknesses.

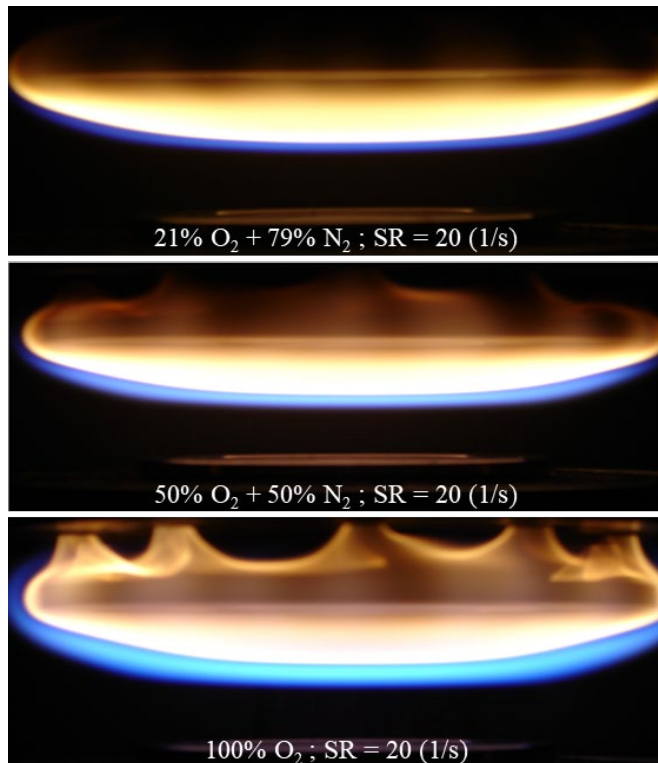
**Table 7.** Measured flame geometry by varying the strain rate.

Strain Rate (1/s)	A (mm)	B (mm)	C (mm)
10	2.69	12.22	14.91
20	1.65	11.88	13.52
30	1.47	11.60	13.07
40	1.29	11.21	12.50

A = blue zone; B = yellow zone; C = flame thickness



**Fig. 7.** Flame structure response to strain rate variations. Results show that both the characteristics zones of the flame and the flame thickness are reduced with increasing strain rates.

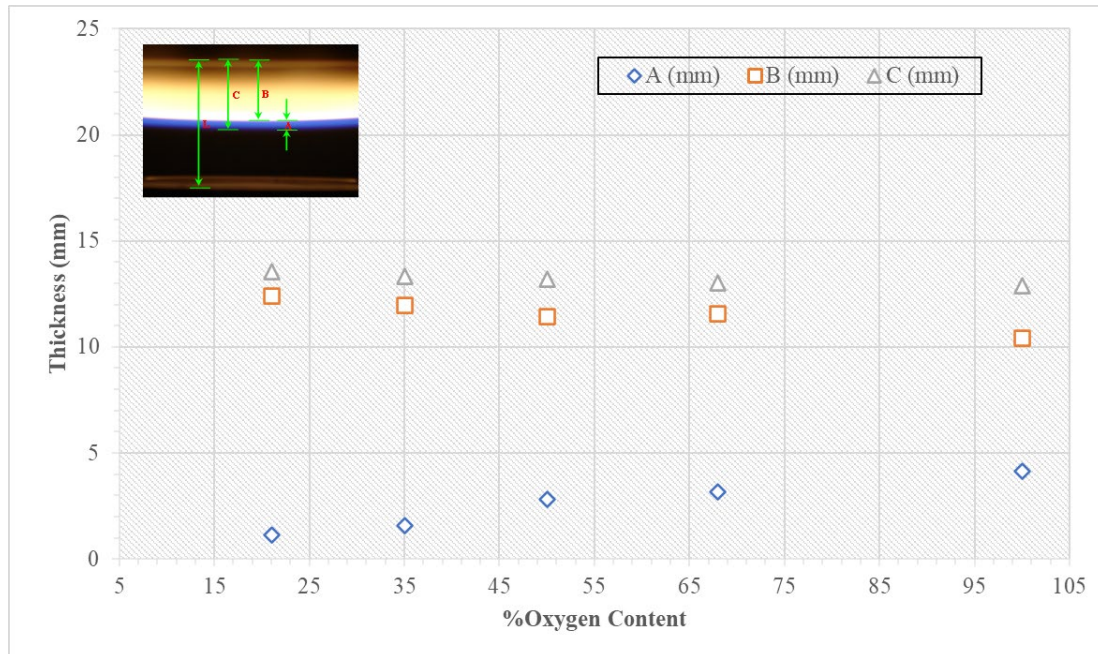


**Fig. 8.** Counter-flow diffusion flame photographs with strain rate of  $20 \text{ s}^{-1}$  formed with various oxygen concentrations. As oxygen content is increased, both zones become more active.

**Table 8.** Measured flame geometry by changing the oxygen content.

Oxygen (%)	A (mm)	B (mm)	C (mm)
21	1.12	12.40	13.55
35	1.59	11.96	13.31
50	2.79	11.43	13.21
68	3.16	11.55	13.00
100	4.14	10.41	12.90

A = blue zone; B = yellow zone; C = flame thickness



**Fig. 9.** Flame structure response to oxygen content variations. Results show that blue zone thickness increased by increasing the oxygen content in the oxidizer stream. Conversely, the yellow zone and the overall flame thickness decrease with increasing oxygen content.

#### 4.2.3 Numerical predictions of temperature profile and chemical species distribution

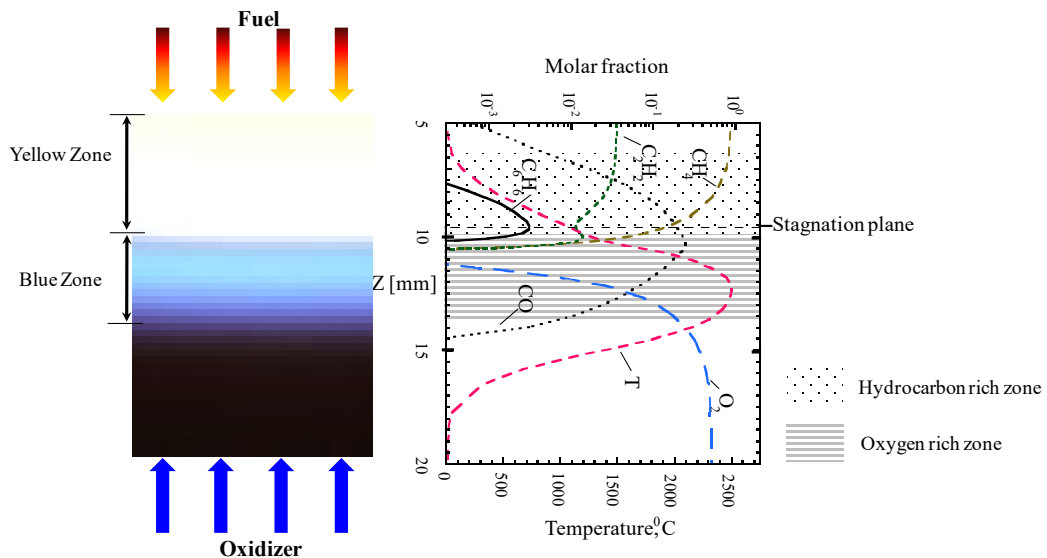
The flame temperature and concentration of chemical species for analysis of nanomaterial synthesis results were obtained from intensive numerical studies by Beltrame et al. [227] and Silvestrini et al. [228] performed for an identical flame configuration to the



counter-flow flame employed in this investigation. **Fig. 10** illustrates the temperature and chemical species profiles for a diffusion flame at a strain rate of  $20 \text{ s}^{-1}$  composed of 50%  $\text{O}_2$  and 50%  $\text{N}_2$  as the oxidizer, and 96%  $\text{CH}_4$  and 4%  $\text{C}_2\text{H}_2$  as the fuel, which is the same composition employed in this investigation. The numerical simulation utilized a chemical kinetic model developed by combining C1–C6 chemistry consisting of 365 reactions and 62 chemical species, and a soot formation mechanism. The authors accounted for radiation heat losses computed according to the weighted sum of gray gases method considering  $\text{H}_2\text{O}$  and  $\text{CO}_2$  as the most radiating species. The soot contribution to radiation was also considered. The predicted drop of gas flame temperature due to radiative losses was found to be below 50K [227].

The computational simulation provides various chemical species and temperature profiles for the two characteristic zones of the flame medium. In **Fig. 10**, the variable  $Z$  in the y-axes of the numerical simulation plot represents the flame location, which is the distance from the fuel nozzle to any position in the flame medium. The variable  $Z$  ranges from 0 mm at the top nozzle boundary to 25.4 mm at the bottom nozzle (oxidizer nozzle) surface. The computed major chemical species were  $\text{CO}_2$ ,  $\text{CH}_4$ ,  $\text{O}_2$ ,  $\text{H}_2\text{O}$ , and  $\text{CO}$ . Although,  $\text{CO}_2$  and  $\text{H}_2\text{O}$  are not shown in the chemical species profiles depicted herein, they were in optimum agreement with measure species as reported by Beltrame et al. [227]. It is important to mention that that both temperature and the chemical components present strong gradients over varying the flame location only by few millimeters. For instance, by varying the distance within the flame from  $Z = 10 \text{ mm}$  to  $11 \text{ mm}$  results in a temperature change from  $1300 \text{ }^\circ\text{C}$  to  $2150 \text{ }^\circ\text{C}$  creating a temperature gradient of  $850 \text{ }^\circ\text{C}$ , based on the temperature computational simulations performed on the counter-flow diffusion flame

[227]. This flame has the highest flame temperature at  $Z = 12$  mm, and it corresponds to  $\sim 2500$  °C. In the same context, the chemical environment rapidly changes from a hydrocarbon species rich region in the fuel side to an oxygen species rich region in the oxidizer side (flame image in **Fig. 10**). The yellow zone rich in various carbon species represents proper conditions for the synthesis of carbon nanotubes, carbon fibers and related materials [109]. Conversely, the blue zone clearly observed in the flame, **Fig. 10**, is rich in oxygen and oxygen ions species which along with the high temperature gradients present in this area, represents suitable conditions for the oxidation of metals. The main objective of this investigation is the synthesis of transition metal oxides; hence, all the attention will be provided to the blue zone of the flame, which is mainly located at  $Z$  ranging from  $\sim 10$  mm to  $\sim 14$  mm.



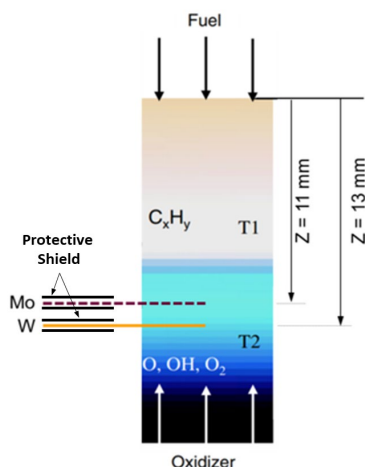
**Fig. 10.** Temperature and chemical species profiles along the  $Z$  axis. The location of the stagnation plane is indicated by the dashed line. Strong temperatures and chemical species gradients are shown in this simulation [227,228,229].

### 4.3 Probe Insertion Mechanism into the Flame Environment

Solid cylindrical W and Mo probes of high purity, ~99.9%, were introduced into the flame medium serving as the bulk metal source for the synthesis of tungsten-oxide and molybdenum-oxide nanostructures, along with combinations thereof. Metallic probe diameters of 0.5 mm and 1.0 mm were employed as the metal precursors. Tungsten and molybdenum were selected as the metals of study in this investigation due to their wide range of unique and unusual properties when converted to their oxides forms with outstanding morphologies of unique and hybrid nature where applications, especially at the micron and nano scales, are remarkable. The TM probes were exposed to the flame medium by introducing them into the blue zone of the flame for a few minutes. Once the targeted residence time was reached, the probe removal process took place within ~30s. This process is driven by sliding a stainless-steel cylindrical tube over the metal probe, the cylindrical tube acts as a protective heat sleeve that shields the probe from exposure to undesired regions of the flame and to the rapid change of environment from the flame to the atmospheric environment. The probe and protective sleeve exposure to the flame medium are depicted in **Fig. 11**.

The TM probe(s)/flame medium interaction play a critical role in studying the synthesis and growth mechanism of nanoscale structures. The temperature of the TM probe used for TMOs nanostructure synthesis is always lower than the local flame temperature due to the radiant and conductive heat losses [230]. The metal probe inserted in the flame is heated by convection and loses heat by radiation and heat conduction along the axial direction of the wire. The probe portion that is not exposed to the flame environment acts as cylindrical pin fin and is responsible for heat conduction loses. It is

important to mention that the temperature difference between the surrounding flame medium and the metal probe can be less than few hundred degrees depending on the probe material properties and the flame conditions [231].



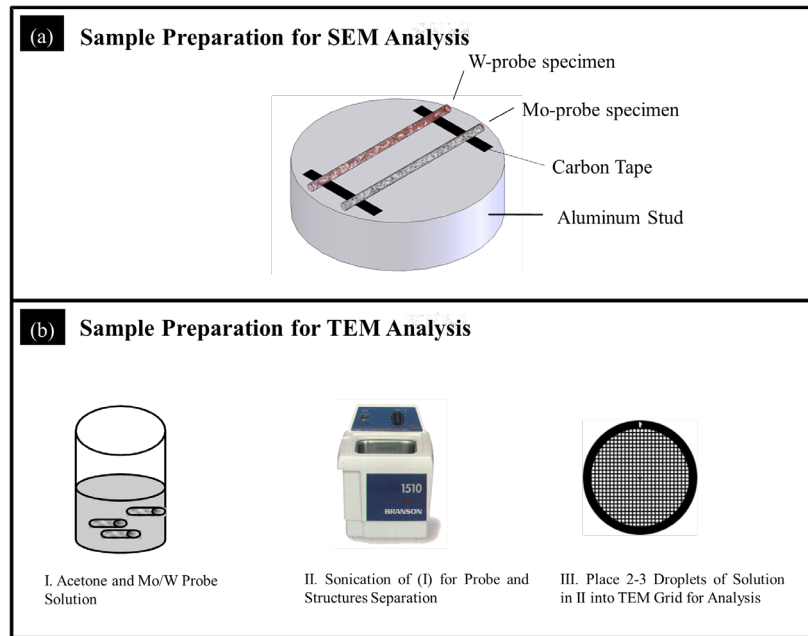
**Fig. 11.** Schematic of the TM probes and protective sleeve/flame interaction.  $Z$  represents the flame location, which is measured from the fuel nozzle. The fuel and oxidizer stream are also illustrated.

#### 4.4 Sample Preparation and Characterization Techniques

Once the TM probe(s) have been exposed to the flame environment, it is hypothesized that the metal oxide layers will form on the probe's surface, thus, preparation steps and various characterization techniques need to be applied in order to analyze the synthesized materials. The part of the TM probes exposed to the flame environment is cut in small pieces immediately after the exposure time has been reached. The smaller pieces with potential nanostructures on their surface are fixed to aluminum studs with electrical conductive carbon tapes in order to perform SEM analyses of the deposits, **Fig. 12a**. Optimum branding of the probes' orientation with respect to the flame environment (i.e. fuel vs. oxidizer side) is critical for understanding material crystallization sites on the probe surface when performing analytical evaluations. As a result, the metal probes upper side

exposed to the fuel side of the flame was strategically marked with white droplet to identify deposition sites around the probe surface as the probe was rotated 180° in both directions to move from the fuel to the oxidizer facing sides of the probe.

The specimens for TEM examinations were prepared by ultrasonic dispersion of TMO deposits collected from the probe's surface in acetone; a drop of the suspension was placed on the TEM copper-substrate/carbon film grid. **Fig. 12b** shows the 3 steps used to accomplish this process.



**Fig. 12.** Sample preparation methods for both SEM and TEM analyses.

In order to further characterize the nanomaterial, other techniques, besides SEM and TEM, must be applied. Among them, X-ray energy dispersive spectroscopy (EDX), selective area electron diffraction (SAED) pattern, X-ray photoelectron spectroscopy (XPS) were employed to characterize the structural and elemental composition of the produced materials. A general description of all these characterization techniques is provided in Appendix A [232].

## 5. CHAPTER 5—FLAME SYNTHESIS OF TMOs ON A SINGLE METAL SUPPORT

---

The objective of this chapter is to describe the underlying mechanism for the flame synthesis of TMOs when a single solid support is introduced in the flame medium. Those mechanisms will serve as the foundation for:

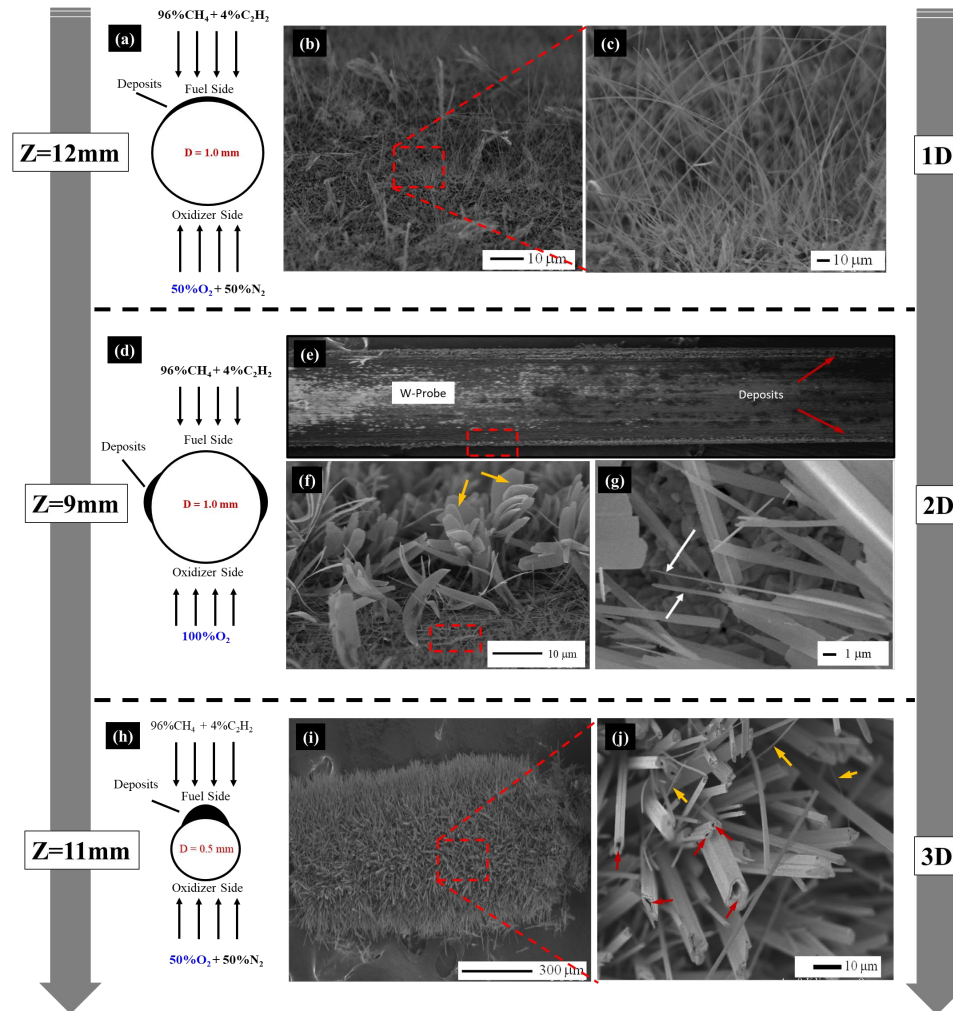
1. The development of a novel combustion-based synthesis method to synthesize crystalline 1D, 2D and 3D tungsten-oxide nanostructures with multiple morphologies on the surface of a solid support.
2. The feasibility of the flame to convert bulk pure W material into 1D and 3D tungsten-oxide nanostructures in a counter-flow flame with strong axial temperature (up to 2000 K/cm) and chemical composition gradients.
3. The first ever fabrication of hybrid nanostructures composed of tungsten-oxide nanorods uniformly covered by layered carbon shells along with their formation mechanism and thus a description of our ability to control their morphologies.
4. Providing fundamental knowledge on the underlying mechanism of solid support synthesis of various types of TMO nanostructures in our flame. That is, one side of the probe (oxidizer side) served for material source while the other side (fuel side) allowed for deposition.

The introduction of a single solid support acting as both material source and deposition allowed our research group to gain detailed insights regarding the formation of TMO nanostructures ranging from 1D/2D/3D to hybrid structures.

### **5.1 Flame Synthesis of 1D, 2D, 3D and Hybrid Nanostructures**

Three key parameters were used to tailor the synthesized structures morphologies and sizes: (i) W-probe diameter, (ii) flame location, and (iii) oxygen/nitrogen content. Tungsten probe with different diameters were independently introduced in the high temperature zone of the opposed flow flame medium for the synthesis of tungsten-oxide nanostructures. For both tested probe sizes it was found that the introduction of the probes in the 1D reaction zone of the counter-flow flame did not visibly disturb the flame nor did it create flame instabilities near the probe's surface or in the overall flame structure. The flow behavior in relation to the metal probe inserted in the flame medium can be considered as a flow around a stationary cylinder. Therefore, flow deceleration is very small in the front of the cylindrical probe [233] and the flow continues to travel upwards around the smooth cylindrical surface. In contrast large flow field instabilities can be created behind the probes with the introduction of ribbon like probes, even when the probes are micron size [233]. The buoyancy effects caused by the hot gases within the flame volume present a challenge for accurately determining the Reynolds number or localized flow characteristics of the cylindrical probes in the gas-flow

The flame location was leveraged along with probe size and oxygen content to yield the optimum chemical species and temperature gradients that favor metal oxidation, sublimation and crystallization.



**Fig. 13.** Evolution of tungsten-oxide nano-sized structures from 1D to 3D morphologies after a Mo probe is exposed into a counter-flow diffusion flame during 2 minutes process. SEM: (a) schematic of probe size and location within flame media, flame/oxidizer configuration, and deposits location for 1D structures, depicting the location of the fuel and oxidizer sides of the probe; (b) low resolution SEM (LR-SEM) image illustrating a high density layer of tungsten-oxide nanowires; (c) high resolution SEM (HR-SEM) image of the boxed area in (b); (d) schematic of probe size and location within flame media, flame/oxidizer configuration, and deposits location for 2D structures; (e) LR-SEM image of the W-probe indicating the deposition takes place on the probe sides; (f) SEM imaging of the boxed area in (e); (g) HR-SEM imaging of the fabricated ribbon-like structures along with the cylindrical 1D nanostructures; (h) schematic of probe size and location within flame media, flame/oxidizer configuration, and deposits location for 3D structures; (i) LR-SEM image of a tungsten-oxide nanostructures cluster; (j) depicts the various hollow and semi hollow large 3D structures (red arrows) along with the high aspect ratio solid cylindrical structures (yellow arrows). Note the boxed areas are not drawn to scale.



The introduction of 1-mm diameter tungsten probes in the high temperature flame medium at flame locations of  $Z = 12$  mm during 2 min resulted in material deposition on the top of the probe (**Fig. 13a**). The fuel and oxidizer were composed of 96%  $\text{CH}_4$  + 4%  $\text{C}_2\text{H}_2$  and 50%  $\text{N}_2$  + 50%  $\text{O}_2$ , respectively. A high density layer of synthesized 1D nanostructures was observed to cover the upper part of the probe's surface (**Fig. 13b**). HR-SEM imaging of the boxed area in **Fig. 13b** indicated that the layer is composed of numerous elongated nanorods randomly oriented with very high aspect ratios (lengths of  $\geq 50$  and diameters of  $\leq 100\text{nm}$ ), **Fig. 13c**. Interestingly, these type of structures present remarkable properties to develop uniform and stable field-emission and for flat panel displays applications with a low threshold field ( $\sim 4.37$  MV/m for an emission current density of  $10\text{ mA/cm}^2$ ) [234]. Similarly, needle-like structures were synthesized by Jin and coworkers [235]. They produced  $\text{W}_{18}\text{O}_{49}$  nanoneedles with high aspect ratios using tungsten powder reacting with water at temperatures ranging from  $800 - 1000$  °C. Argon flow was bubbled through the boiling W/water mixture placed in a furnace; the temperature was raised to  $800 - 1000$  °C and maintained during 40 min. This technique evidently requires longer synthesis' times and various steps compared to the counter-flow flame method.

Additional experiments were conducted enriching the oxidizer stream with 100%  $\text{O}_2$  while the fuel type and composition (96%  $\text{CH}_4$  + 4%  $\text{C}_2\text{H}_2$ ) was kept constant. Increasing the oxygen content results in a compressed flame, thus, reducing the overall flame thickness; while increasing the height of the high temperature region of the flame, **Table 8**. In the pure oxygen flame the two characteristic zones are easily identified: a

yellow zone rich in hydrocarbon species and a blue/high temperature zone abundant in oxygen based radicals. The insertion of 1-mm diameter W probes in the high temperature flame medium at flame locations of  $Z = 9$  mm for 2 minutes resulted in a thick layer of material deposited on the sides of the probe surface (**Fig 13d-e**). The deposits are composed of micron-sized flat ribbon-like structures of few nanometers in thickness and of tens of micrometers in length. Interestingly, the base of the flat ribbons-like structures is filled with nanoscale 1D structures similar to those illustrated in **Fig. 13c**. The yellow arrows in **Fig. 13f** depict the flat ribbon-like structures; whereas the elongated 1D nanorods are illustrated by the boxed area. HR-SEM on a selected area at the base of the ribbon-like structures shows 1D nano scale structures are extruded from the edges of the flat nanoribbons (see arrows in **Fig. 13g**). Similar tungsten-oxide ribbon-like structures were reported by Li et al. [236] who conducted experiments employing a heating process carried out for more than 1 hour, followed by cooling in order to achieve synthesis.

Tungsten probes of different diameters were also tested in order to gain insight into the growth mechanism of the tungsten-oxide structure on a solid support. The synthesis results show the effect of the probe diameter directly affects both the thermal and chemical environment of solid support flame nanomaterial synthesis by (i) limiting the variation of the chemical species and temperature around its surface, and (ii) defining its temperature by balancing convective and radiant losses. The insertion of the 0.5-mm probe closer to the flame front at a flame location of  $Z = 11$  mm resulted in the formation of high density materials composed of large 3D structures (**Fig. 13h-j**). At this particular flame position, the flame temperature is  $2100^{\circ}\text{C}$  (**Fig. 10**); whereas the probe temperature corresponds to  $1200^{\circ}\text{C}$  due to heat losses from radiation and conduction through the probe. Numerous

individual 3D structures were located on the  $900 \times 600 \mu\text{m}$  cluster, as shown in the inset of **Fig. 13i**. **Fig. 13j** depicts a HR-SEM image of the boxed area in **Fig. 13i** showing a high density of 3D independent structures with several microns in length and a few micrometers in diameter possessing various channel-shaped structures either completely or semi-hollow. Some of these structures present a clearly visible cross-section of square, rectangular, and triangular shapes as illustrated by the red arrows in **Fig. 13j**. Among the large 3D structures, it is evident the presence of solid 1D structures of very high aspect ratios similar to those observed in **Fig. 13c**, see yellow arrows in **Fig. 13j**. Hollow tungsten-oxide structures are of particular interest due to their possible application as host structures. Their hollowness may also contribute to the extension of porosity and surface area. Hollow tungsten-oxide structures organized in pine-tree-like arrays were synthesized by Hu et al. [237] by heating  $\text{WS}_2$  powder in oxygen. This multi-step process was performed at a temperature of approximately 1300 to 1400°C during 1 hour [237]. Hexagonal W-trioxide tubes were produced by Wu et al. [238] by using an electrochemistry deposition technique; the growth process involved various stages and a tungsten substrate temperature of about 800°C lasting 1 hour. Cheng et al. [239] obtained highly ordered tungsten trioxide nanotube arrays utilizing a method consisting of an anodic aluminum oxide (AAO) template. The use of AAO has various disadvantages including the introduction of impurities into the tungsten-oxide structures and eventually complicates the process of separation.

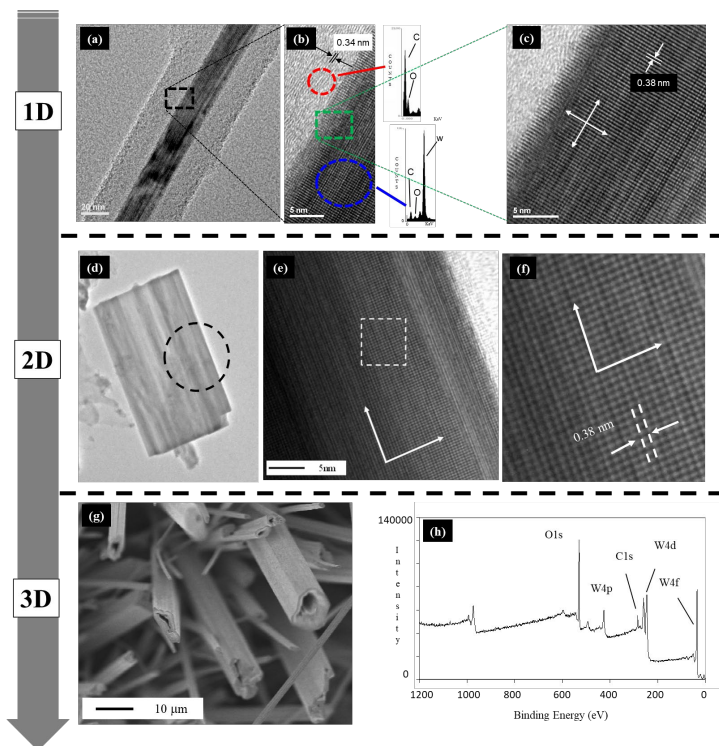
### ***5.1.1 Characterization of the chemical composition of the 1D, 2D and 3D tungsten-oxide nanostructures***

TEM and high resolution-TEM (HR-TEM) provided further insight into the structural, compositional and morphological characteristics of the formed structures. Initial analysis on the 1D nanostructures revealed contrast of light and dark regions indicating that the presumed nanorods are, indeed, built of two different materials, **Fig. 14a**. The core/inner material of darker contrast is composed of a highly crystalline metal oxide which is covered by an outer material of lighter contrast composed of carbon layers with lattice spacing similar to that of graphite indicating that these 1D structures are, in fact, nanowires composed of metal oxide cores and carbon shells, **Fig. 14b**. Moreover, electron beams of various diameters applied to the selected areas on the surface of the grown structure were employed for studying the chemical composition of these structures via EDX analyses. Results indicated that focused beam on the core materials contains W, O, and C (carbon from the TEM holder film) whereas, the lighter contrast material is composed primarily of O and a high intensity peak C (i.e., carbon shells), **Fig. 14b-inserts**. The inner metal oxide material has a lattice spacing of 0.38 nm, which closely corresponds to a (002) plane of monoclinic  $\text{WO}_3$  (**Fig. 14c**); whereas the sheath material is composed of cylindrical carbon layers with d-spacing of 0.34 nm, resembling the characteristics of graphite. A more detailed assessment of how the hybrid metal oxide cores surrounded with a sheath of carbon shells are formed is described in section 5.1.2.

Due to their minimal thickness, the 2D structure selected for TEM analysis is highly transparent to the electron beam (**Fig. 14d**). Higher resolution TEM imaging on the selected structure shows the extraordinary structural uniformity and highly ordered

crystalline structure, **Fig. 14e**. HR-TEM imaging shows that these thin flat structures are free of dislocations and structural defects, and similarly to the nanowires, a lattice spacing of 0.38 nm (**Fig. 14f**) was measured, which corresponds to a (002) plane of monoclinic  $\text{WO}_3$ .

Due to the large size of the 3D structures for TEM analysis the oxidation states of these structures are carried out by XPS. For XPS analysis, the structures were removed from the W probe and placed on a carbon adhesion tape in powder form (**Fig. 14g**). The quantitative results show 3:1 ratio for O and W and the percentage of atomic concentration for W 4f and O 1s are measured to be 23.1 and 76.9 which closely correspond to  $\text{WO}_3$ , **Fig. 14h**.



**Fig. 14.** Chemical composition characterization of the synthesized 1D to 3D tungsten-oxide nanostructures: (a) LR-TEM image depicting the core-shell morphology of the formed 1D nanorods; (b) HR-TEM illustrating the morphology of the 1D core and shells and their elemental compositions (EDX inserts); (c) higher resolution TEM showing the lattice spacing of the formed 1D structures; (d) typical TEM image of a grown ribbon-

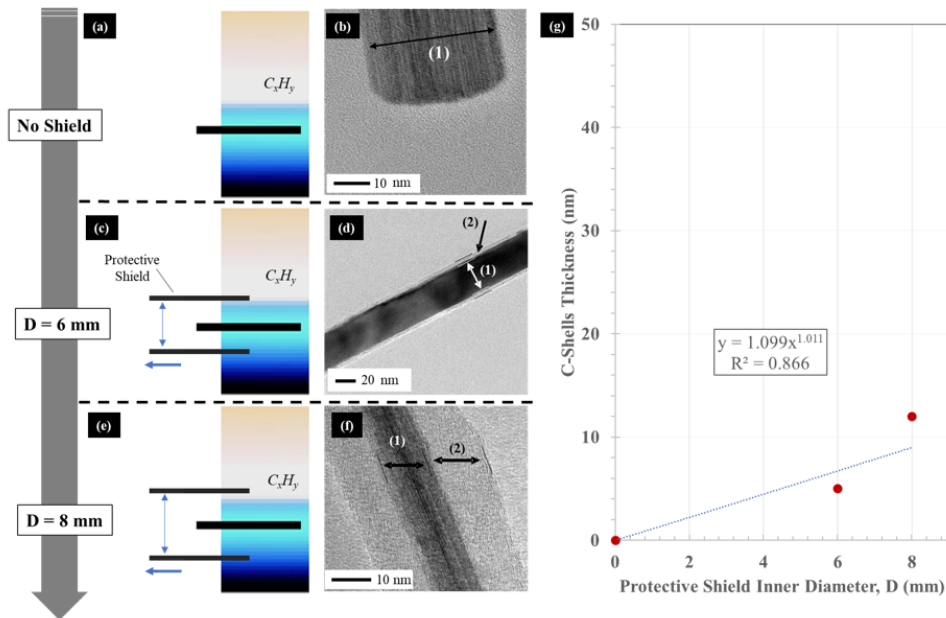
like 2D structures; (e) higher resolution image of (d); (f) HR-TEM image of the boxed area in (e); (g) SEM image of the typical 3D structures; (h) XPS spectrum of the large 3D tungsten-oxide nanostructures. Note the boxed/circled areas are not drawn to scale.

### 5.1.2 Synthesis of hybrid tungsten-oxide cores with carbon shells

Recently, much attention has been focused on the synthesis of engineered hybrid nanomaterials that are organic and inorganic in nature. Decreasing the characteristic size of inorganic and organic components presents a pathway to optimum tailoring of the materials' properties at a molecular level. As a result, the atomic manipulation yields novel materials that either exhibit characteristics in between the two original components or even new properties [240].

Various tubular shields with diameter  $D$  ranging from 2 to 8 mm were employed in order to protect the grown nanomaterials from the non-uniform boundary envelope of the flame during the probe removal process from the flame media. This process typically requires ~20 seconds and it is very likely that the large shield diameters can capture hydrocarbon species from the fuel side of the flame and exposed the already synthesized metal oxide nanorods to carbon-rich species. Experimental results indicated tungsten-oxide nanorods are first grown on the surface of the probe by exposing the W-probe in the flame oxygen-rich region for a few seconds. Upon the nanorods being formed, the capture of carbon-rich species from the fuel-rich zone of the flame during the probe removal process results in the rapid formation of uniform carbon shells. Experimental results performed with no shield and probe tubular shields with internal diameters of 6 and 8 mm resulted in 1D nanorods covered with no carbon layers (**Fig.15a-b**), 5 nm (**Fig.15c-d**), and 12 nm (**Fig.15e-f**), thick carbon shells, respectively. This further confirms that carbon species

present in the upper part of the flame were captured during the shield motion and served as a source of the carbon to form the C-shells surrounding the tungsten-oxide 1D structures. **Fig. 15g** depicts the carbon layer increase with increasing internal diameter of the protective shield, used during metal probe removal post flame exposure time, following a power mathematical format. The technique of using different sizes of tubular shield diameters allows for tailoring the amount of carbon species transferred, hence, controlling the thickness of the CNT layer surrounding the metal-oxide nanorod. In other studies on flame synthesis of tungsten-oxide nanowires [241], it was suggested that carbon can diffuse from the upper part of a flame rich in carbon species to a flame zone where only oxygen radicals are present, although in that work the carbon present in the structures was detected by EDX only and was not evident via TEM imaging.



**Fig. 15.** TEM images of hybrid nanowires and tungsten-oxide nanorods formed on the surface of the 1 mm W-probe: (a) schematic indicating probe position at  $Z = 12$  mm and the lack of protective shield use; (b) TEM results illustrating the sole presence of tungsten-oxide on the formed 1D nanorods; (c) schematic indicating probe position at  $Z = 12$  mm and the protective shield with internal diameter  $D = 6$  mm; (d) TEM image depicting the tungsten-oxide nanorods covered with a thin layer of carbon shells; (e) schematic indicating probe position at  $Z = 12$  mm and the protective shield with

*internal diameter  $D = 8$  mm; (f) TEM image revealing the tungsten-oxide nanorods covered with a larger layer of carbon shells; (g) chart representing the C-shells thickness obtained with varying protective shield diameters during probe removal. Diameter of the probe/substrate, the protective shield and the size of the flame structure are not drawn to scale.*

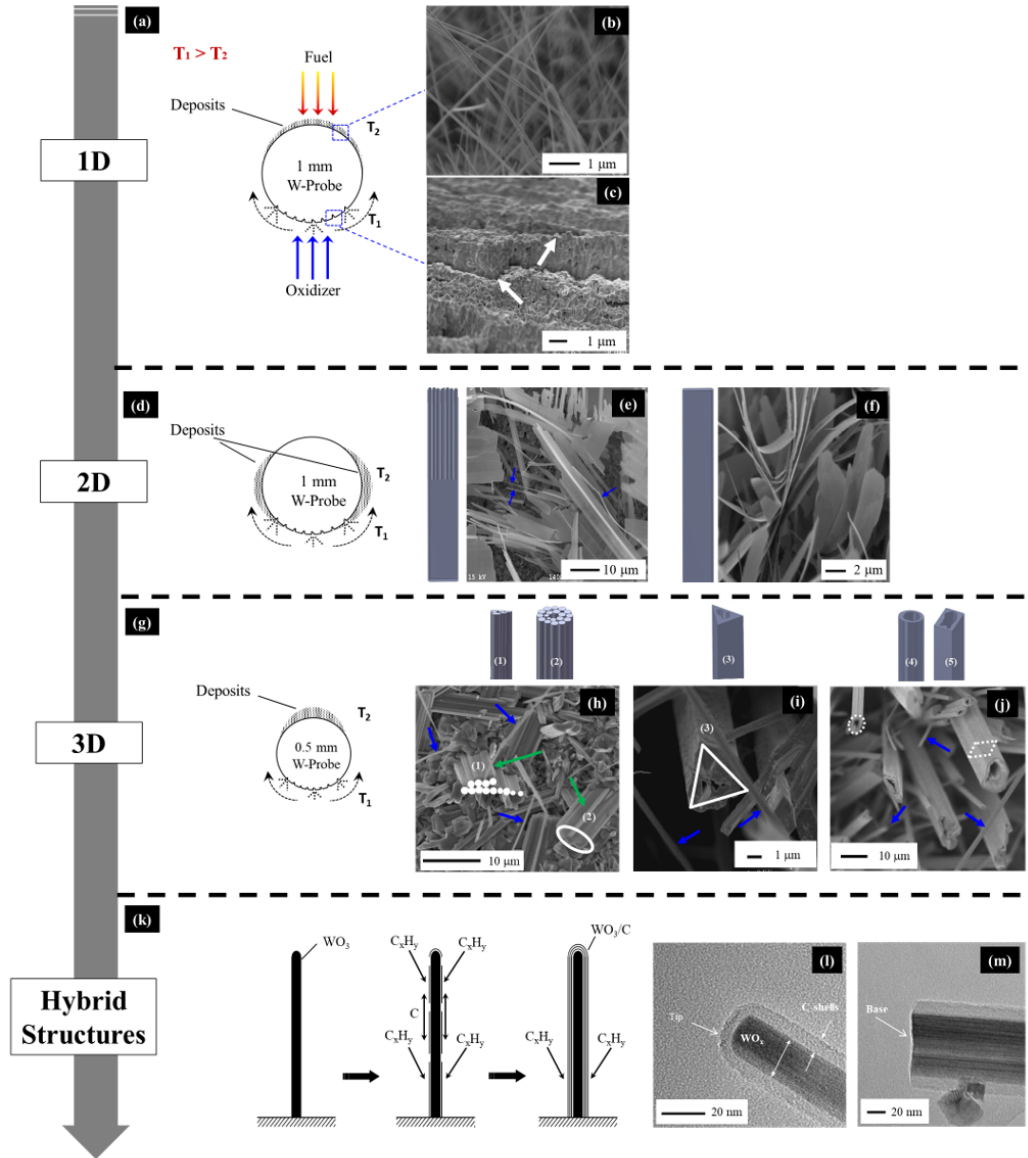
The ability to synthesize hybrid nanomaterials composed of metal and metal oxides with carbon shells have been studied by several authors [242,243]. For example, superconducting nanowires and nanorods from lead, tin, and other materials are sensitive to oxidation. Encapsulation in carbon nanotubes is an ideal method to protect and stabilize such nanostructures. A simple and reproducible method yielding individual micrometer-long carbon nanotubes filled with superconducting tin nanowires was developed by Jankovic et al. [242].

### ***5.1.3 Proposed growth mechanism of the 1D, 2D, 3D and hybrid nanostructures***

The growth mechanism of tungsten-oxide structures consists of two consecutive sub-mechanisms: 1) the global mechanism which deals with the melting/sublimation, and condensation of tungsten-oxides on the lower side of the solid support and 2) the crystallization of the structures on the upper surface of the probe as the material is being transported by the gas flow traveling in the direction of the stagnation plane located on the fuel side of the flame. The recorded distribution of the deposited materials suggests that the gas flow transfers the material from the probe side exposed to the high temperature oxidizing environment ( $T_1$ ) and they are then further deposited and crystallized on the probe surface downstream at a lower temperature side ( $T_2$ ) (**Fig. 16a**). The deposits' location, thickness, and their shapes are tailored as the flame and the probe diameter vary affecting the crystallization process and resulting morphology of the structures. The same



effect has been observed during the flame synthesis of molybdenum-oxides when using a Mo-probe as the solid support [244,245].



**Fig. 16.** Growth mechanism of the synthesized 1D, 2D, 3D, and hybrid nanostructures: (a) schematic diagram of the recorded distribution of deposited materials suggests the transfer of material from the lower to the upper part of the probe,  $T_1 > T_2$ ; (b) SEM image collected on the deposits on the upper part of the probe show the layer to be composed of needle-like 1D nanostructures; (c) SEM image of the bottom surface of the probe depicting strong material erosion; (d) schematic diagram of the recorded distribution of deposited materials suggests the transfer of material from the lower to the sides of the probe,  $T_1 > T_2$ ; (e-f) SEM image of the synthesized 2D flat ribbon structures with the presence of 1D nanorods (e) and inserts depicting the computer

*generated 2D shapes; (g-j) schematic and SEM images of the 3D formed structures along with computer generated inserts; (k-m) schematic and TEM images of the fabricated tungsten-oxide core and carbon-shells hybrid nanostructures.*

SEM analyses on the surface of the probe facing the oxidizer side show no accumulation of any type of structural material for all morphologies. To the contrary, a strong degree of material erosion is present mainly due to the probe exposure to the high temperature which modifies the probe surface in an irregular manner (**Fig. 16c**). The W probe inserted in the flame medium containing high concentrations of atomic and molecular oxygen is rapidly oxidized. Various oxides ( $WO_{3-x}$ ) and hydroxides are continuously formed and evaporated from the lower part of the probe considering the lower boiling points of tungsten-oxides when compared to pure W metal (i.e., ranging from 2255 to 3855 °C lower boiling points for their oxide forms). This supports hypothesis (i) and (ii) postulated in Section 3.1 regarding the formation of oxide films on the metal substrate and their subsequent evaporation to form oxide vapors. Interestingly, these metal oxides are crystallized as  $WO_3$  structures (**Fig. 16b**) in the upper part of the probe due to the change of flame temperature and chemical environment. In fact under these flame conditions, the formation of vapor-phase tungsten-oxides can be quite spontaneous [246], especially at the gas-phase temperature attained in the counter-flow flame (i.e.  $\sim 2400^\circ\text{C}$  at  $Z = 12$  mm). Jin et al. [235] reported that by increasing the reaction zone temperature above  $1100^\circ\text{C}$ , solely  $WO_3$  structures are formed. Furthermore, the presence of water vapor (combustion by-product) and radical species such as OH and H at the probe location may further enhance chemical and phase transformation of metal oxides and the growth process [246,247], further supporting the hypothesis (iii) in Section 3.1.

Both, oxygen content and probe diameter can increase the concentration of the material in the gas-phase, therefore, affecting the crystallization process on the upper parts of the probe [245]. Experiments conducted increasing the oxygen content in the oxidizer to 100% effectively compresses? the flame thickness; while, increasing the high temperature zone area. The introduction of 1-mm W-probe in the oxygen-rich flame at  $Z = 9$  mm, resulted in the formation of 2D flat ribbon like structures on the sides of the probe (**Fig. 16d**), Interestingly, 1D nanorods appear to also extrude from the flat ribbon structures (**Fig. 16e**), hence, suggesting that the flat structures are formed as a result of (i) growth of 1D nanorods, followed by (ii) lateral agglomeration of 1D structures. As the crystallization rate increases due to varied flame temperature and chemical species gradients favoring greater deposition rates within the same exposure time (i.e. 2 minutes) as that used for synthesis of 1D structures, the ribbon-like structures facets become well defined as shown by the SEM image in **Fig 16f** and demonstrated by the computer generated schematic, **Fig 16f-insert**.

Additionally, it was found that experiments performed on a 0.5-mm diameter probe during 2 minutes resulted in the synthesis of large 3D structures along with few 1D structures. While experiments conducted on 1-mm diameter probes for flame exposure time of 2 minutes resulted in the production of only 1D nanostructures. The reduction in the size of the probe diameter increased the probe's temperature and therefore the etching rate of the material on the lower part of the probe facing the fuel side thus yielding the crystallization of larger 3D structures. Extensive studies by Hu et al. [237] showed that  $W_{18}O_{49}$  whiskers could aggregate to form hollow fibers. Jeong and coworkers [248] produced ZnO microtubes by coalescence of ZnO nanowires. Wu et al. [238] reported the

formation of well-faceted hexagonal tungsten trioxide tubes. They proposed that tungsten-oxide nanowires agglomerate and then coalesce laterally into tubular structures followed by a dehydration process which was responsible for the formation of the well-faceted structures.

The schematic of the interpretation of the 3D in **Figs. 16g-j**. The first stage corresponds to the growth of individual tungsten-oxide 1D structures on the probe surface. In the case of high influx of material being transported by the gas flow from the lower to the upper part of the probe, nanorods grow closely to each other to create closely packed bundles of the 1D nanostructures (**Fig. 16h**). The green arrows in the SEM image in **Fig. 16h** point to a microbundle of 1D nanostructures, in an earlier synthesis stage, with the shapes as illustrated by the matching numbers in the computer generated graphics shown in **Fig. 16h**. A lower number of individual 1D structures are also present as highlighted by the blue arrows in **Figs. 16h-j**. Interestingly, the diameters of the individual nanorods closely resemble those present in the microbundles as shown by the white dots. The closely packed 1D structures began to coalesce laterally into 3D structures of various configurations depending on the shape of the initial arrangement of the 1D structures, **Figs. 16h-j**. As the influx of material continues downstream, the coalesced structures will continue to grow laterally. It is also interesting to note that some of these 3D structures are hollow with a rough surface as shown in **Fig. 16i**. The hollow effects can be attributed to the absence of some nanowires at the center of the structures, considering that if a microbundle contains a large number of the 1D structures, the incoming  $WO_x(g)$  material depositions takes place along the edges of the coalesced 1D nanorods (Berg effect) and may never reach the 1D bundle of structures located at the center, therefore, preventing

their continued growth and as a result leaving a cavity in the center [249, 250], as shown in **Fig. 16j**. Although further theoretical and experimental analysis is needed to confirm the proposed mechanism of formation of the large 3D structures, observations similar to those made in CVD studies [251] greatly support the validity of this mechanism.

Remarkably, it was assessed that varying the diameter of the protective shield employed for specimen removal post flame exposure results in hybrid structures composed of tungsten-oxide cores covered by carbon layers of different thicknesses. The growth mechanism of the 1-D tungsten-oxide/carbon nanowires involves two sequential steps: (i) the tungsten-oxide nanorod formation and (ii) the carbon shell growth. At the flame location of  $Z = 9$  and 8 mm corresponding to the maximum flame exposure for both protective shields used, the resulting concentration of hydrocarbon-rich species can be significant. That is 0.5mol%  $C_2H_2$  and 20mol%  $CH_4$  and 2mol%  $C_2H_2$  and 60%  $CH_4$ , for the 6 mm and 8 mm diameter shields, respectively. **Fig. 16k** represents a schematic proposing the progression of growth of the hybrid tungsten-oxide/carbon nanowires with first the synthesis of 1D nanorods, followed by carbon species present in the upper part of the flame being captured by a protective shield during the removal process. At high temperature the tungsten-oxide nanorods act as an active surface for the rapid deposition of hydrocarbons. Thus, it is possible to suggest that the entire 1D nanorod acts as a catalytic surface for hydrocarbon decomposition and growth as cylindrical carbon nano-shells. The presence of tungsten-oxide inside a graphitic shell is quite surprising. However, this agrees well with existing thermodynamic data for bulk materials. In particular, tungsten trioxide has an enthalpy of formation of  $\Delta H_f^\circ = -843$  kJ/mol that is much lower than the enthalpy of formation of carbon dioxide  $\Delta H_f^\circ = -394$  kJ/mol [252]. This preserves the preferential

bonding of oxygen with tungsten ensuring the structure's stability. HR-TEM analysis of the hybrid structures reveal that the tips of the slender metallic structures are capped with carbon layers, **Fig. 16l**; and in contrast, the bases of the structures are always flat and free of carbon layers, **Fig. 16m**.

## **6. CHAPTER 6—GAS-PHASE SYNTHESIS OF TMO NANOSTRUCTURES BASED ON A SINGLE SUPPORT**

---

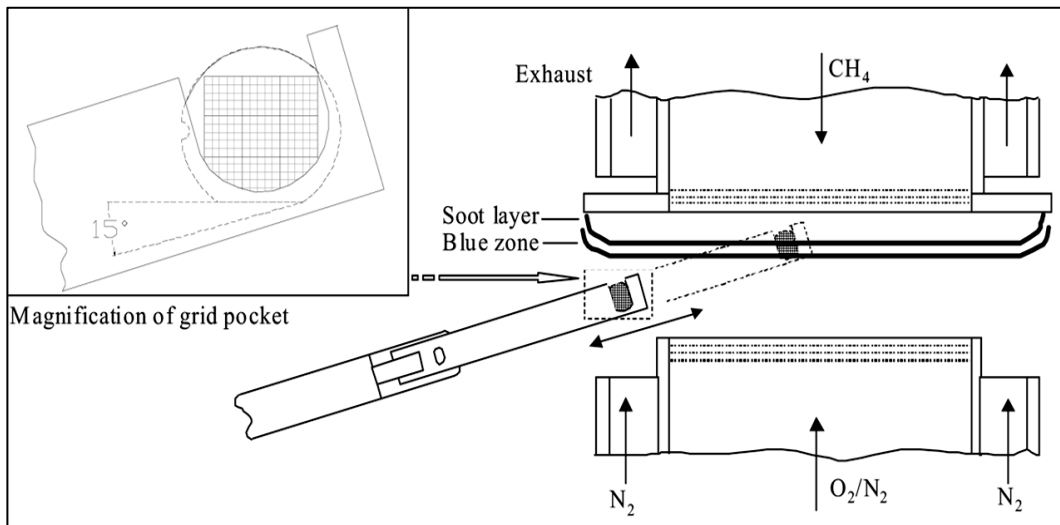
The need to further understand the synthesis mechanism of 1D/2D/3D and hybrid nanostructures drove the need to investigate how or whether 1D-3D structures can be formed in the gas-phase and hence evaluate the formation of TMO structures in the flame media and how they can, then, be deposited on the solid support taking advantage of the counter-flow flame high temperature and chemical species gradients. Furthermore, gas-phase combustion synthesis has proved to be one of the most versatile and promising techniques employed for scale-up production of spherical nano-scaled particles like ceramics, carbon black, etc. [253,254].

This chapter focuses on the gas-phase combustion synthesis of elongated tungsten-oxide polygonal nanocrystals and octahedron nanoplatelets by inserting a W-probe into the oxygen-rich flame to produce metal oxide precursors near the surface of the probe followed by the synthesis of the nanostructures in the upper part of the flame gas-phase medium. The non-isothermal counter-flow diffusion flame employed as the synthesis medium in this investigation provides strong temperature and chemical composition gradients which produce an appropriate environment for the synthesis of high purity nanostructures with controlled morphology, composition and structure.

### **6.1 Gas-phase Synthesis of TMO Nanoplatelets**

To facilitate the collection of formed structures in the gas-phase media, a thermophoretic sampling technique [255,256] was employed for collection at different

flame positions (**Fig. 17**). In this technique, a cold surface, i.e. an electron microscope grid, placed into the hot flame media produces considerable gradient of temperatures. As a result, the synthesized structures travel in the direction of the generated gradients toward the cold surface driven by thermophoretic forces. The 3 mm in diameter electron microscope grid possesses a copper mesh substrate along with a  $\sim 20$  nm pure carbon film deposited on one side of the grid. The synthesized materials collected on the electron microscope grid were then evaluated and characterized employing TEM and EDX techniques.



**Fig. 17.** Thermophoretic sampling technique used for collection of the gas-phase fabricated nanostructures. Adapted from [227]

The evolution of the fabricated structures was obtained by analyzing the collected specimens at distances from the fuel nozzle of  $Z = 13, 12,$  and  $11$  mm, where the temperature varies from  $2100$  to  $2450^\circ\text{C}$  and structures evolve from discrete particles to elongated nanocrystals (**Fig. 18a-b**). The structures collected at the flame location of  $Z = 13$  mm (i.e. TEM grid and W-probe at the same flame position, **Fig. 18**) illustrate the early formation of a high density of smaller discrete shapeless particles (blue arrows)

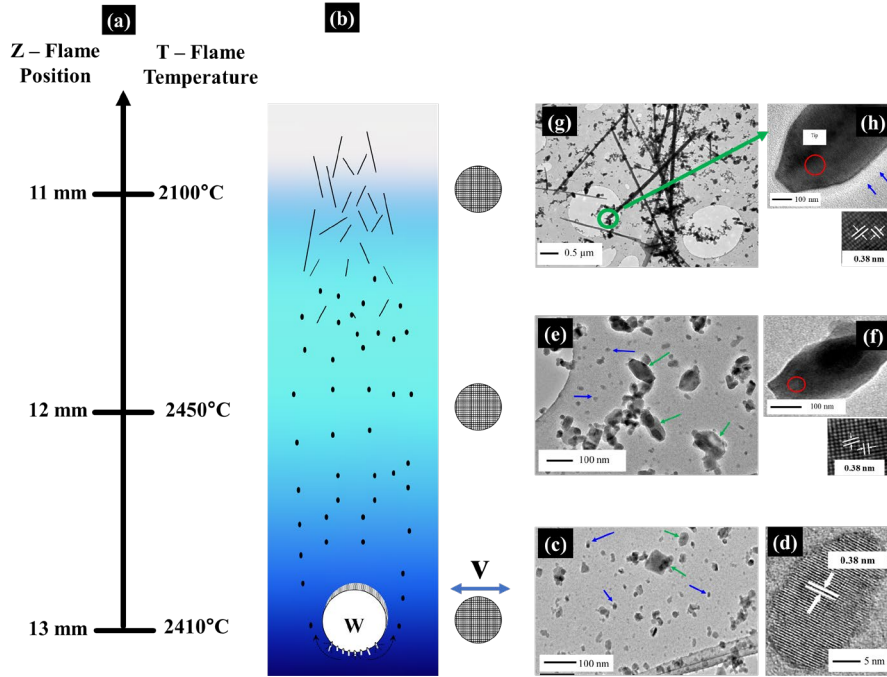


accompanied by a few larger crystal-like structures (green arrows), **Fig. 18c**. HR-TEM image of a typical discrete shapeless particle shows its well-organized atomic structure that likely resulted from tungsten-oxide vapors nucleation from the metal probe/flame interaction to form  $\text{WO}_3$  as per the measured lattice spacing of 0.38 nm, **Fig. 18d**.

Additional specimens were collected further away from the W-fixed precursor source to study their morphology evolution as they travel toward the stagnation plane through varying gradients of temperature and chemical species. TEM images depicting the typical morphology of the thermophoretically collected samples at a flame position of  $Z = 12$  mm are illustrated in **Figs. 18e-f**. Resulted structures consist of well-defined polygonal nanocrystals (green arrows) accompanied by smaller discrete shapeless particles as pointed out by the blue arrows in **Fig. 18e**. Further inspection shows that the synthesized structures have a well-defined polygonal shape as depicted by the HR-TEM image in **Fig. 18f**. The atomic resolution image of the circled area in **Fig. 18f** reveals that they are highly organized, crystalline, and free of defects, **Fig. 18f-insert**.

TEM analysis of the samples collected at a closer distance from the edge of the fuel nozzle,  $Z = 11$  mm, revealed the formation of large aspect ratio structures with lengths in the order of several microns and well-defined shapes, **Fig. 18g**. The morphology of the synthesized elongated structures resembles well-defined polygonal nanocrystals bounded with multiple lateral faces, **Fig. 18h**. The application of atomic resolution imaging analysis on a typical rod-like structure, circled area in **Fig. 18h**, clearly shows the high degree of crystallinity present in the synthesized structure, **Fig. 18h-insert**. However, it is important to mention that the synthesized structures at  $Z = 11$  mm are surrounded by a carbon layer as pointed out by the blue arrows on the wall of the structure, in **Fig. 18h**. This may be the

result of the partially exposure of the 3 mm TEM grid to the yellow/blue zone interface. Evidently, the ultra-small discrete shapeless crystal particles present at the lower part of the flame clearly represent the building blocks for the larger well-faceted polygonal crystals formed in the upper flame zone as the vapors and structures travel toward the stagnation plane.



**Fig. 18.** Gas-phase synthesis of octahedral and elongated polygonal nanocrystals: (a) flame positions and respective temperature within the flame media; (b) schematic of the formed structures evolution from tungsten-oxide vapors to well-defined elongated polygonal nanocrystals as structures flow toward the stagnation plane; (c-d) LR- and HR-TEM imaging of the high density discrete shapeless particles collected at  $Z = 13$  mm, where the probe and TEM grid are at placed at the same position in the flame; (e-f) LR- and HR-TEM images of polygonal structures accompanied by smaller discrete shapeless particles collected at the  $Z= 12$  mm; (g-h) LR- and HR-TEM images of high density of nanocrystals of large aspect ratios collected at  $Z= 11$  mm.

Atomic resolution TEM imaging on the octahedral and elongated polygonal structures formed at  $Z = 12$  and  $11$  mm, respectively, shows the highly ordered crystalline lattice of the structures. It is interesting to note that the lattice spacing for the structures

obtained at all three flame positions was measured to be  $\sim 0.38$  nm closely corresponding to the (002) plane of monoclinic  $\text{WO}_3$ . Therefore, it can be inferred that the elemental composition of the formed structures does not vary with the position in the flame medium, along with the lattice spacing of the gas-phase synthesized structures resembling that of the 1D W-oxygen based nanowires [257] grown on the solid support in Chapter 3.

## 6.2 Growth Mechanism of the TMO Octahedron Nanoplatelets

The quick and continuous evolution of irregular and discrete particles in the lower part of the flame to well-faceted octahedron nanoplatelets and elongated rod-like nanocrystals in the upper part of the flame can be attributed to the strong temperature and chemical species gradients present in the counter-flow flame environment. For instance, at a flame location of  $Z = 13$  mm the metallic oxide vapors are exposed to a combustion environment with 1.5 mol% of O and 10 mol% of  $\text{O}_2$  and a flame temperature of  $2450^\circ\text{C}$ ; while at flame location of  $Z = 11$  mm the vapors are exposed to only 0.2 mol% of  $\text{O}_2$  with a flame temperature of  $2100^\circ\text{C}$ . Therefore, O and  $\text{O}_2$  concentration gradients between the specified flame positions correspond to 0.75 mol%/mm and 4.9 mol%/mm, respectively, with a temperature gradient of  $175^\circ\text{C}/\text{mm}$ .

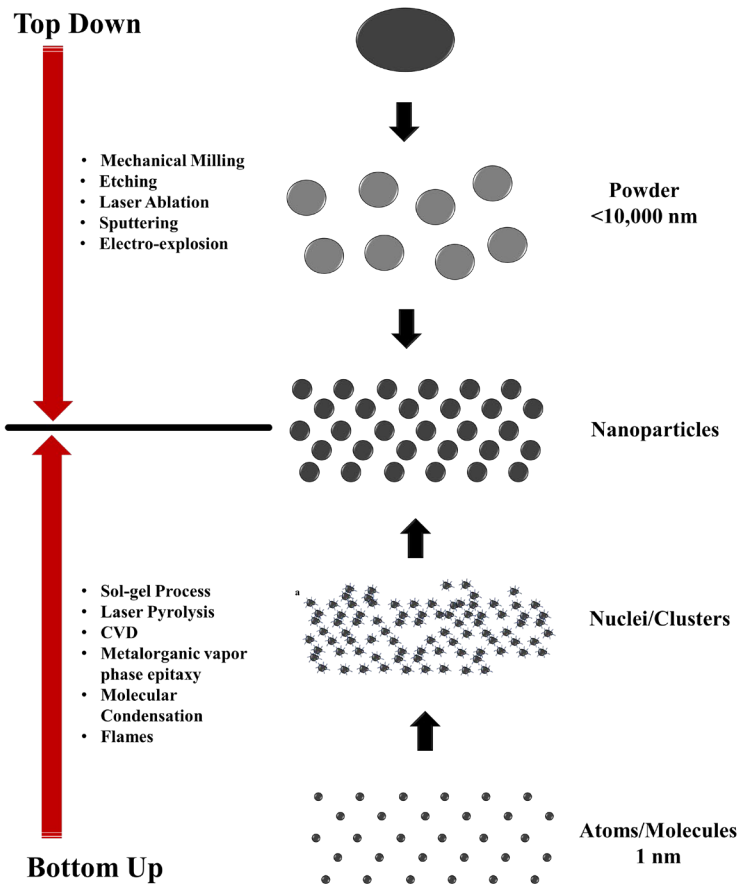
The proposed mechanism (**Fig. 18b**) consists of: (i) the solid W wire probe interaction with the oxygen-rich environment, containing O and OH radicals [258], leads to the quick oxidation of the solid precursor with the formation of highly oxidized metal layers in strong oxidation states; (ii) The tungsten-oxide's outermost layer is first vaporized and transported by the gas flow and exposed to the flame medium which rapidly varies in temperature and chemical species concentrations as the gas flows towards stagnation plane;

(iii) The evaporation or sublimation from the probe surface of the metal oxide layers resulted in the formation of the precursor gas, which polymerizes or nucleates to form shapeless or irregular discrete particles which will later form polygonal structures or octahedron nanoplatelets and later well-defined elongated polygonal rod-like nanostructures. The continuous thermophoretic collection of micron size samples of synthesized materials at flame locations in the axial direction suggests the transfer of Tungsten-oxides by the gas-phase from the side of the wire exposed to the high temperature oxidizing environment and their further crystallization and shape evolution as they travel away from the probe towards a region of lower temperature and oxidation states, **Fig. 18b**. It is important to mention that the structures will be transported by the gas flow towards the stagnation plane, where carbon-rich components are present; therefore, the interaction of the formed structures with hydrocarbon-rich species in the upper part of the flame can be expected. TEM grids of 3 mm in diameter inserted at flame zones of  $Z = 11$  mm cover flame zone range from  $Z = 9.5$  (hydrocarbon-rich zone) to 12.5 mm (oxygen-rich zone), thereby, the production of hybrid tungsten-oxide rod-like polygonal structures covered with carbon-shells is also attained, **Fig. 18h**, with the metal-oxide structure serving as the catalytic surface that favors hydrocarbon decomposition and crystallization similar to the structures described in Section 3.1.3.

## 7. CHAPTER 7—FLAME SYNTHESIS OF HYDRID AND COMPLEX TMOs HETEROSTRUCUTURES ON SOLID MULTI- METALS SUPPORT

---

Despite several methodologies being typically applied for the synthesis of nano- and micron-scaled materials, they can be classified in two different approaches: “*top-down*” and “*bottom-up*” (Fig. 19). The “*top-down*” approaches are based on miniaturizing larger-sized materials into smaller components through etching and/or ion-beam milling. Focused electron beam and/or focused ion beam are employed in the “*top-down*” approach for reducing the size of the materials. Highly patterned and aligned nanostructures can be produced via the “*top-down*” method. However, this technique is considered expensive since it is composed of multistep processes resulting in the need of extensive preparation time. Another drawback of this method is the inability to produce high quality (single crystalline) structures. The “*bottom-up*” method is based on the assembly of molecules through evaporation and deposition on a surface through vapor-phase transport or chemical reactions such as electrochemical deposition and solution-based techniques. Through this method, highly pure nanocrystalline and complex objects (physically and/or chemically) can be produced. This approach is considered a low cost procedure compared to the “*top-down*” process. Also, doped and mixed materials can be easily synthesized. However, material integration (e.g. the combination of oxygen with a metal to form a metal oxide) on the surface of substrates might be troublesome and also, production of well-arranged and patterned structures is often very challenging to produce employing this method [259].



**Fig. 19.** The synthesis of nanomaterials via top-down and bottom-up approaches.

Adopted from [260].

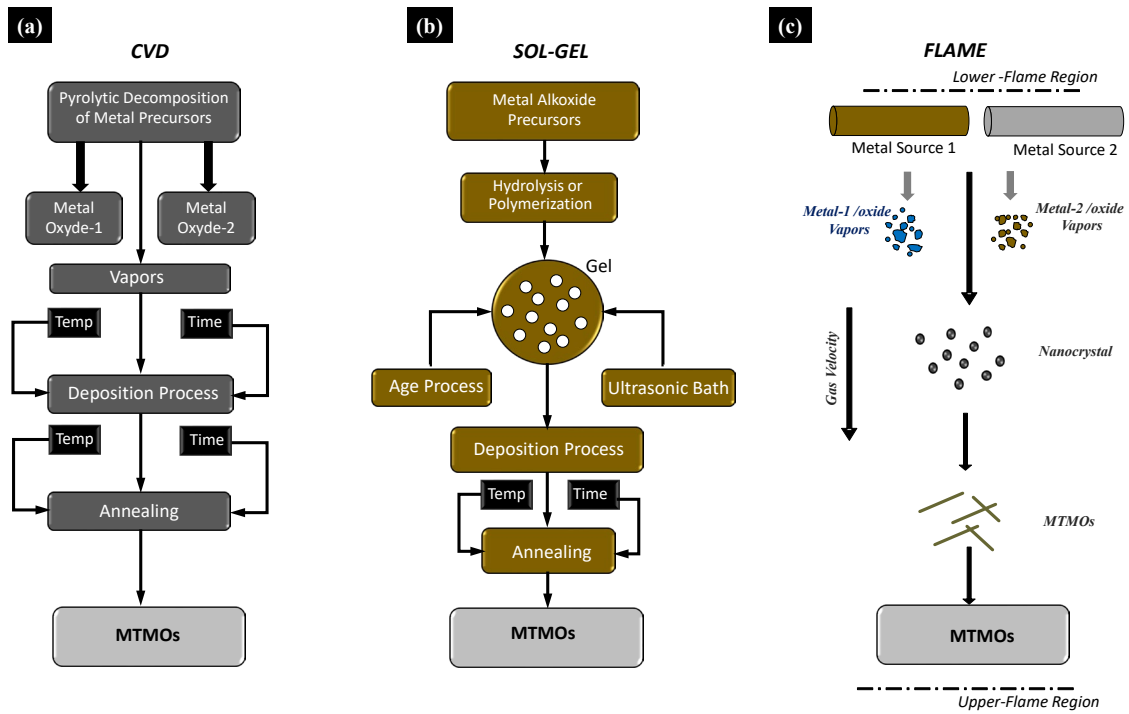
Common synthesis methods of TMO nanostructures such as CVD, sol-gel, and flames, are all categorized under the “bottom-up” methods. A variety of “bottom-up” related techniques have been proposed and developed for the synthesis of TMOs including aqueous chemistry [261,262,263], chemical vapor deposition [264,265,266], pulsed laser deposition [267, 268, 269], high temperature heating process in a restricted vacuum chamber [270], and metalorganic vapor phase epitaxy [271], flames [221], etc.

In recent years nanotechnology research focus has shifted to increasingly complex nanostructures, especially those of a hybrid nature, which offer sensational opportunities

for tailoring materials with end-functionality based on the chemical composition, morphology, and size of the initial precursors at the nanoscale [272,273]. This allows for gaining significant performance optimization on the end-structure as a result of counterbalancing the disadvantages and optimizing the advantages of the individual components. Mixed metal oxide nanomaterials (or heterometal oxides nanomaterials) represent an interesting group of hybrid materials that can play an important role in many areas of chemistry and physics as a result of their exclusive electronic and magnetic properties obtained when synthesizing structures with multiple metals in an oxide matrix [274,275].

The level of structural excellence needed for the fabrication of heterostructures made of MTMOs have led the development and evolution of multiple synthesis methods. Different research efforts have shown that fabricating a large number of MTMO heterostructures of different architectures can be achieved by combining different precursor materials [211,276]. CVD is a well-developed technique for the synthesis of multiple heterostructures consisting of four key phases performed in the span of multiple hours and different temperatures: (i) pyrolytic decomposition of the metallic precursors; (ii) transport of the volatile precursor via the vapor phase to the reaction chamber, (iii) decomposition of the formed materials on the substrate, (iv) annealing to improve absorption of the precursor materials (**Fig. 20a**). The Sol-gel technique also consists of a multi-step process to achieve synthesis of MTMOs including (i) hydrolysis or polymerization which results in metal alkoxide precursor monomers (i.e. sol); (ii) reaction assisted via aging and/or ultrasonic energy to form the solution (i.e. gel); (iii) deposition via insertion of substrate into the ‘gel’; (iv) annealing to improve absorption of the

precursor materials (**Fig. 20b**). Some the key limitations of CVD and sol-gel techniques consists of the complexity of multi-step processes, scalability, selectivity of its products, longer synthesis periods (i.e. various hours), and in most cases the limited flexibility of the tailored morphologies that can be synthesized. As a result, flames have emerged as simple and one-step synthesis technique of MTMO heterostructures where the simple introduction of two metal precursor in the flame medium can result in high purity mixed metal oxides of complex architecture in the order of few minutes or even seconds [211,221], **Fig. 20c**.



**Fig. 20.** Schematic representations comparing the essential steps needed for the preparation of MTMOs employing: (a) CVD; (b) Sol-Gel; and (c) flame methodologies.

Flame synthesis is shown to be a scalable single step process, with high growth rates, optimum control over the morphology, flexibility (gas-phase and/or solid support), and an economical technology [277,278] for producing controlled single and mixed metal-oxide nanoscale heterostructures [279,280,281,282]. In this chapter, we present the flame



synthesis of multi-dimensional complex tungsten/molybdenum-oxide heterostructures (i.e. polyhedral, tree, flower, grass, and forest-like) on solid supports employing Mo and W probes as the material precursors and surfaces for deposition; along with the proposed growing mechanism of the fabricated structures.

## 7.1 Classes of Heterostructures

Typically, at least three main types of mixing patterns can be observed when combining multiple materials: (i) core-shell segregated materials, consisting of a core of one component surrounded by a shell of a different one; (ii) subclusters segregated materials with at least two clusters sharing an interface or a small number of bonds at the interface. It should be noted that at the microscopic scale the physical interface between two different materials is known as the heterojunction [288]; and (iii) mixed or intermixed materials, homogenous mixtures of at least two components with clear bonds among them with new Bragg reflections when compared to the individual components [283]. Furthermore, these MTMOs or complex heterostructures can also be classified in six typical configurations:

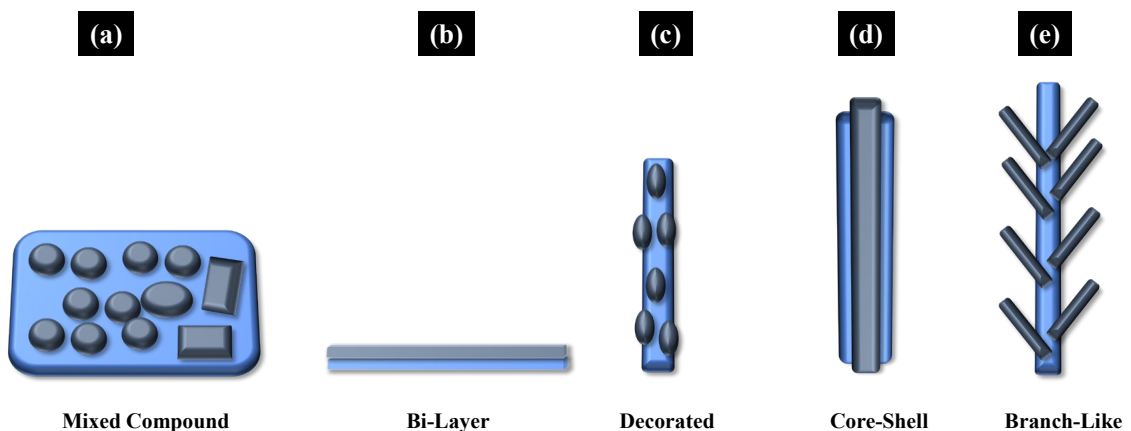
- (i) Mixed compounds: a simple mixture of materials without a specific distribution, where the processing path does influence the materials' dispersion which ultimately tends to control the end structure's performance [284], **Fig. 21a**.
- (ii) Bi/multi-layered films: 2D films with well-defined interfaces. However, these materials are not extremely popular due to the small surface to volume ratios which limits their applications [285] **Fig. 21b**.

- (iii) Decorated structures: where the host structures are decorated with nanoparticles of a secondary material. Interestingly, the degree of decoration and the presence of metal oxide to metal oxide contact can aid multiple applications, such as sensing mechanisms. The effectiveness of these structures consists of the secondary material not covering the entire structure and rather used in smaller quantities [276]

**Fig. 21c.**

- (iv) Core shell structures: this configuration consists of wire-like arrangement where the host structure is completely covered with a secondary phase maximizing the interfacial area and limiting the exposure of the host material to the surrounding environment [276] **Fig. 21d.**

- (v) Branch-like structures: this configuration is formed by the combination of 1D secondary nanorod from a single 1D nanorod host. This heterostructures present similar properties as the decorated structures with much larger surface areas. The fabrication of these structures often requires a multi-step approach [286] **Fig. 21e.**



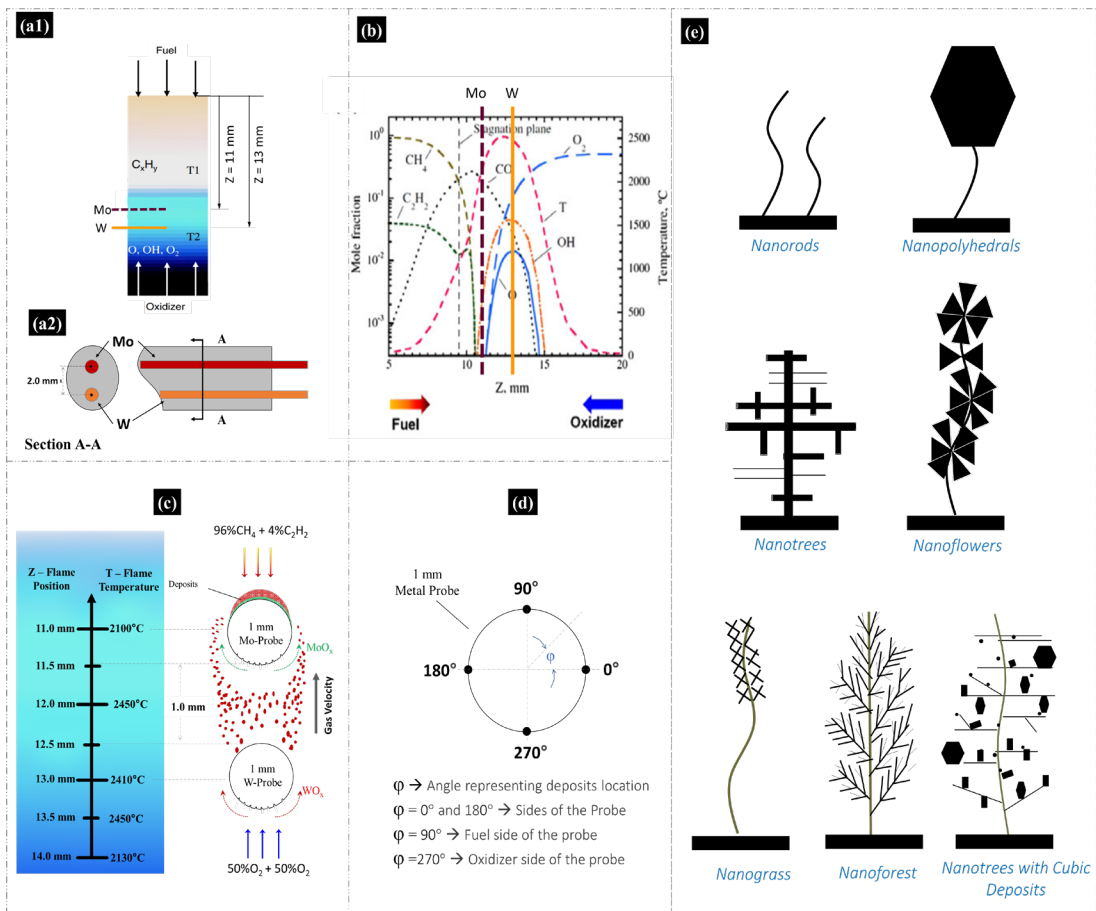
**Fig. 21.** Schematic of multiple configurations of MTMOs or complex heterostructures: (a) mixed compounds; (b) bi-layer films; (c) decorated; (d) core-shell; and (e) branch-like heterostructures. Adapted from [221].

Heterostructure and/or complex nanomaterials are a unique class of nanostructures that offer significant performance enhancements in the end-product by balancing the drawbacks and optimizing the benefits of the individual components. Multifunctionality becomes possible since each main component of the structure with complex chemical/physical morphology plays a complementary role [287]; thus, their combined properties, along with their complex nature make them excellent building materials for many applications including photocatalyst, hydrogen production, energy conversion and storage [287], gas sensors [288,289,290], solar cells [291], smart windows [292,293], among others. Wang et al. [294] reported the construction of 3D transition metal oxide core/shell heterostructure (CuO/CoO) to be used as binder and conductive agent-free anodes for lithium batteries yielding optimum electrochromic performance ( $1,364 \text{ mAhg}^{-1}$  at  $100 \text{ mAg}^{-1}$  after 50 cycles and keeping  $1,140 \text{ mAhg}^{-1}$  after 1000 cycles). Datta et al. [295] fabricated nanostructures composed of branched Te nanotubes on  $\text{SnO}_2$  “backbone” structures. Such complex heterostructure yielded high specific surface areas, offering ample active sites for gas sensing purposes, thus, yielding a quick change in resistance. Rao et al. [296] synthesized a  $\text{WO}_3/\text{BiVO}_4$  core/shell 1D-structure photoanode using the  $\text{BiVO}_4$  as the primary light absorber and  $\text{WO}_3$  as the electron conductor; achieving simultaneous light absorption and charge separation producing a photocurrent of  $3.1 \text{ mA/cm}^2$  which enhanced photoelectrochemical (PEC) water splitting efficiency.

## **7.2 Flame Synthesis W/Mo-heterostructures of Hybrid and Complex Morphology**

The counter-flow burner and flame configuration described in Chapter 4 is also employed for the synthesis of the W/Mo hybrid and complex heterostructures reported in

this chapter. The fuel (96%CH<sub>4</sub> + 4%C<sub>2</sub>H<sub>2</sub>) and oxidizer (50%O<sub>2</sub> + 50%N<sub>2</sub>) were introduced from the top and bottom nozzles, respectively, both at a constant strain rate of 20 s<sup>-1</sup> and atmospheric pressure, **Fig. 22a1**. The distance between the nozzles was kept constant throughout all experiments at 25.4-mm. The 1-mm in diameter (W) tungsten and (Mo) molybdenum probes both with purity of ~99.95% are always introduced into the oxygen-rich zone of the flame at axial positions (Z) of 13- and 11-mm, respectively, employing a ceramic sample holder with two concentric orifices 2-mm apart (**Fig. 22a2**). It is noteworthy to mention that the probes' position 'Z' is selected based on the flame temperature and chemical gradients suitable for each transition metal to have access to oxygen species that favor the formation of metal oxides (**Fig. 22b-c**).



**Fig. 22.** (a1) Photograph of the flame formed by the counter-flow reactor ( $T1$  and  $T2$  are temperatures in the carbon- and oxygen-rich sections of the flame, respectively). (a2) schematic of the ceramic sample holder. (b) numerical predictions on temperature profile and major chemical species in the diffusion opposed-flow flame [227]. (c) sketch of the insertion of the metallic probes and the deposition behavior. (d) graphical representation of the deposition locations and nomenclature defined for discussion thereof. (e) Schematic of the morphology of the synthesized structures.

High axial temperature gradients (up to 2000K/cm) and chemical composition gradients are characteristic features of the counter-flow diffusion flame employed herein [227], **Fig. 22b**. Thereby, the position and the exposure time of the precursor wires within the flame environment can strongly affect the synthesis process. To investigate the synthesis of tungsten/molybdenum-oxide heterostructures with complex morphology by introducing the W and Mo substrates into the flame oxidizer zone, rich in O, OH, and O<sub>2</sub> species. The probes' surface-to-surface separation was approximately 1.0 mm (**Fig. 22c**), with most of the crystallization taking place around the Mo-probe located downstream towards the stagnation plane as a result of the greater oxidation and edging rates of tungsten-oxide vapors when compared to those of molybdenum. It is inferred that nano-sized structures with a variety of morphologies (i.e. polyhedron, tree, flowers, grass, and forest-like structures, **Fig. 22e**) can be synthesized by simply controlling the rate of formation of the metal oxide precursors in one region of the flame and their deposition to form the crystals in cooler regions of the flame. It is noteworthy to mention that the time and mode of insertion of the probes plays a key role on the type of structure formed. For further discussion purposes, the specific synthesis or deposit's crystallization sites will be based on the probe's surface location angle ' $\varphi$ ' measured counter-clockwise, i.e. for the 'oxidizer side' or the lower side of the probe,  $\varphi = 270^\circ$ ; for the 'fuel side' or the top section

of the wire,  $\varphi = 90^\circ$ ; and for the ‘sides of the probe’,  $\varphi = 0^\circ$  and  $\varphi = 180^\circ$  of the metal wire(s) (**Fig. 22d**).

To gain insight into the fabrication mechanism of the multiple morphologies described in **Fig. 22e**, W and Mo probes were introduced into the flame using two experimental mechanisms: (i) simultaneous dual metal flame insertions, and (ii) variable dual metal flame insertion.

The simultaneous insertion exposed the metal substrates to residence times ranging from 30 to 150 sec. Whereas the variable time insertion mechanism consisted of introducing the metal probes into the flame at different times with the Mo probe exposed to an initial constant residence time of 90 sec, followed by increased exposure to the flame environment after the insertion of the W probe during residence times ranging from 30 to 60 sec.

### **7.3 Simultaneous Dual-Metal Flame Insertion at Different Flame Zones to Fabricate Nanostructures with Complex Morphologies**

This experimental mechanism consists of both W and Mo probes being introduced into the flame medium simultaneously employing residence times ranging from 30 to 150 sec that resulted in the synthesis of nanomaterials with complex morphologies resembling polyhedral-, trees-, and flower-like structures.

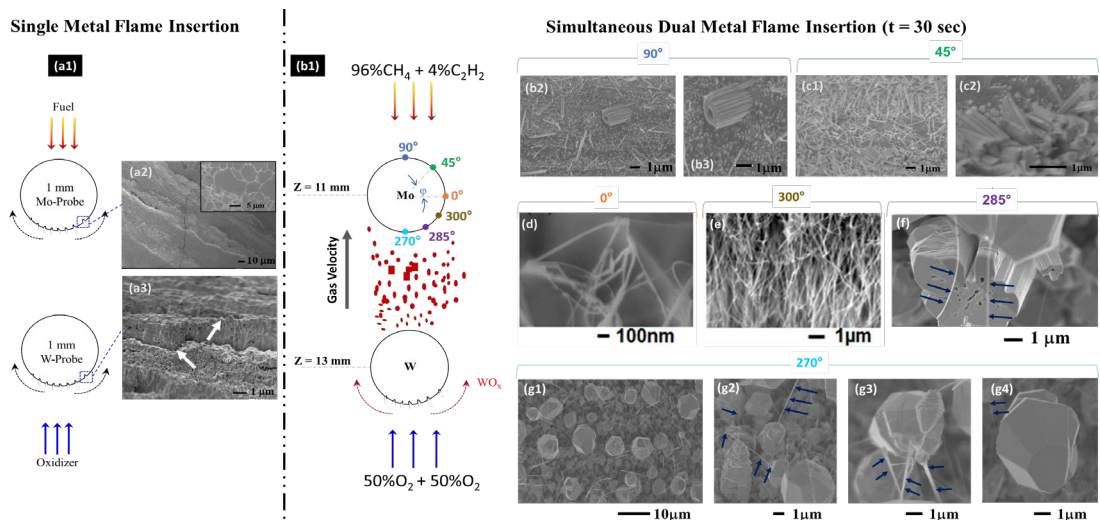
#### ***7.3.1 Synthesis of complex nano and micron scaled structures with 30 sec of flame residence time***

It is reported that that the oxidation rate molybdenum does not significantly change with varying temperature and pressures; conversely tungsten oxidation rate increases with

increasing temperature and pressure [297]. Experimental data reported by Gulbransen et al. [297] indicates that the rate of oxidation of tungsten is over twice that of molybdenum and it tends to increase with increasing temperature and pressure. This suggests that after some time the W-probe releases tungsten-oxide vapors at higher concentrations to overwhelm the deposition and crystallization of structures taking place on the surfaces of the Mo probe. To further support this hypothesis SEM images collected from the bottom of the Mo and W probe when inserted by themselves into the flame media indicates no structural growth and rather a higher erosion of materials in the oxidizer side of the W probe when compared to that of Mo, **Figs. 23(a1-a3)**.

**Fig. 23(b1)** depicts the schematic of the dual insertion of Mo and W probes along with the location of the crystallization sites. Results obtained from the Mo probe after simultaneous exposure of both probes for 30 seconds indicated that deposits at the 90° crystallization site resulted in 1D nanorods or the “backbone” structures, **Figs. 23(b2-b3)**. As the evaluated location nears the 45° range (i.e., arc length from 0°), it is evident that the deposition rate tends to augment forming a larger density of 1D structures (**Fig. 23(c1)**), which in some cases commence to coalesce to form larger 3D agglomerates composed of 1D rod-like nanostructures **Fig. 23(c2)**. As crystallization sites at 0° and 300° are evaluated, higher aspect ratios and increased density of 1D nanorods are fabricated, **Figs. 23(d-e)**. It is evident that the geometrical location of the crystallization sites at 0° (i.e. sides of the probe) favors the larger deposition rates based on the flow of oxide gases around the metal substrate. **Fig. 23f** confirms the presence of larger 3D structures at the 285° site, however, the presence of 1D rod structures is always confirmed at all crystallization sites, see arrows in **Fig. 23(f)**. The structures formed at the 270° crystallization site primarily depicts

irregular polyhedral-like morphologies of sizes ranging from 3.2 to 9.5  $\mu\text{m}$  structures and up to twenty facets, **Fig. 23g**. Interestingly, rod like ‘backbone’ structures extruding from the 3D polyhedral structures are also present, see arrows in **Figs. 23(g2-g4)**.



**Fig. 23.** 1D rod-like ‘backbone’ structures and polyhedral complex nanostructures fabricated after both probes being exposed to a flame residence time of 30sec. The Mo and W probes are introduced in the flame media at  $Z=11\text{mm}$  and  $Z=13\text{mm}$ , respectively. The metal probes are introduced into the flame simultaneously for a residence time of 30 seconds. (a1) schematic of a single metal probe inserted into the flame media; images collected on the oxidizer side of the Mo (a2) and W (a3) probes when exposed to the flame medium with no additional probe insertion; (b1) schematic of the dual insertion of Mo and W probes into the flame medium at flame positions of  $Z=11\text{mm}$  and  $Z=13\text{mm}$ , respectively, along with the location of the crystallization sites; (b-c) imaging of the 1D structures deposited at  $90^\circ$ ; and  $45^\circ$  crystallization sites on the Mo probe; (d-e) high density of “backbone” structures deposited at  $0^\circ$  and  $300^\circ$  sites; (f-g) imaging of structures synthesized at crystallization sites located at  $285^\circ$  and  $270^\circ$ .

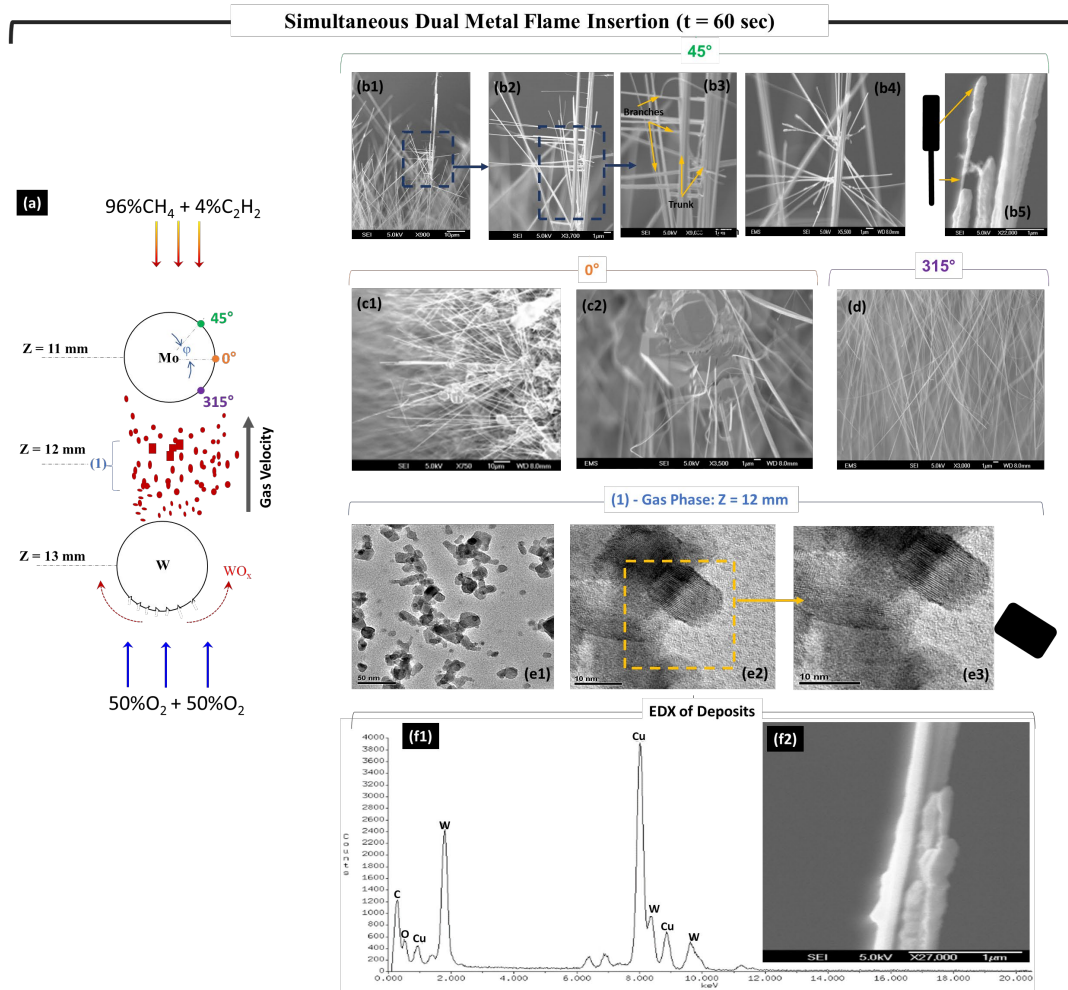
### 7.3.2 Synthesis of complex nano and micron scaled structures with 60 sec of flame residence time

Further increasing the residence time of both metal probes into the flame volume to 60 sec resulted in the synthesis of tree-like structures. **Fig. 24** depicts SEM images from the cyclization sites located at  $45^\circ$ ,  $0^\circ$ , and  $315^\circ$  on the Mo probe surface. The Mo and W probes were introduced simultaneously to the oxygen rich portion of the counter-flow



diffusion flame at  $Z = 11$  mm and  $Z = 13$  mm, respectively, for a duration of 60 sec, **Fig. 24a**. The deposits crystallized at the  $45^\circ$  site, are composed mostly of high aspect ratio nanorods extruding from the surface of the Mo probe, **Fig. 24(b1)**. Higher resolution SEM depicts some of the structures resembling nanotrees that are composed of cylindrical or rod-like ‘trunks’ and ‘branches’, **Fig. 24(b2)**. Each branch consisted of 1D structures with diameters ranging from 100 to 450 nm and extruded nearly perpendicularly from the parent branch, **Fig. 24(b3)**. The trunks or “backbone” structures have diameters ranging from 600 nm to more than  $1.1\ \mu\text{m}$  and the average height of the nanotrees was approximately  $89.5\ \mu\text{m}$ ; thus, indicating that the nanotrees are, indeed, 3D hierarchical structure composed of 1D rod-like branches with 3D micro-trunks (backbone structures). Additional SEM imaging collected at the  $45^\circ$  site suggest that the tips of the branches and trunks contain metal oxide deposits resembling elongated cubical-like deposits, **Fig. 24(b4-b5)**. Further analysis of the formed structures indicates that their shape is highly dependent on the location of the crystallization sites on the surface of the Mo probe. The structures deposited at the  $0^\circ$  site are composed of nanorods with larger 3D deposits containing various facets, **Figs. 24(c1-c2)**. SEM imaging of the deposits at the  $315^\circ$  crystallization site of the Mo probe reveal that only highly dense nanorods with uniform surfaces and no sign of 3D objects/deposits are attained, **Fig. 24d**. It is evident that the presence of nanorods or “backbone” structures is always attained on the surface of the Mo probe despite the location of the crystallization sites. The morphology of the deposits on the “backbone” structures tend to differ depending on the crystallization site being analyzed, consequently, it can be inferred that the gas flow around the probe and the probes geometry are responsible for the morphology evolutions. The variation of the crystal growth direction or physical

morphology as depicted on the final structures in the SEM images can only be possible by the introduction of the two probes. In this configuration, if both probes are introduced simultaneously, one of the probes (W) serves as the source of material while the second probe (in this case, Mo) serves as a substrate for crystallization and growth of the tungsten-oxide vapors. It is important to note the melting point of the probes and the flame location. The flame temperature where the Mo is introduced in the flame is  $\sim 2,100^{\circ}\text{C}$  while for the W probe the flame temperature is  $\sim 2,410^{\circ}\text{C}$  and the melting point of Mo and W is  $2,623^{\circ}\text{C}$  and  $3,422^{\circ}\text{C}$ , respectively. The variation of flame temperature and oxygen species at evaluated flame locations are ideal for generating metal oxide vapors at various rates. Thereby, it is anticipated that the W probe exposed to the high flame temperature and oxygen species ( $Z = 13$  mm) zone will result in the rapid release of tungsten-oxide vapors in higher concentrations. Consequently, the creation of high concentration tungsten-oxide vapors overwhelms the formation of molybdenum-oxide vapors, also favored by the higher oxidation rates of W when compared to Mo [297]. To further confirm this behavior, thermophoretic sampling was conducted in between the W and Mo probes at the flame position  $Z = 12$  mm, **Fig. 24a**. TEM imaging shows that the tungsten-oxide vapors are composed of well-developed platelets, **Fig. 24(e1-e3)**. Remarkably, the gas-phase formed platelets resemble the tips of the deposits on the surface of the rods, **Fig. 24(b4-b5)**. To aid on the identification of the chemical composition of the formed structures, EDX analysis of the deposits in **Fig. 24(f2)** confirmed they are composed of mostly of W and O, since both C and Cu readings are a result of the TEM grid being made of copper with a carbon film, **Fig. 24(f1)**.



**Fig. 24.** Nanotrees-like structures synthesized after both probes being exposed to a flame residence time of 60 sec. (a) schematic of the dual insertion of Mo and W probes into the flame medium at flame positions of  $Z=11\text{ mm}$  and  $Z=13\text{ mm}$ , respectively, along with the location of the crystallization sites and location of collected samples of the gas-phase formed crystals; (b1-b5) SEM images illustrating the randomly distributed nanotrees; (c1-c2) randomly oriented tree-like structures with 3D deposits with various facets; (d) high dense nanorod-like structures; (e1-e3) TEM images of tungsten-oxide structures generated in the gas-phase at a location (1) depicted in (a); (f1) EDX of deposits at the tips (f2) of the end of the tree-like structures.

### ***7.3.3 Synthesis of complex nano and micron scaled structures with 150 sec of flame residence time***

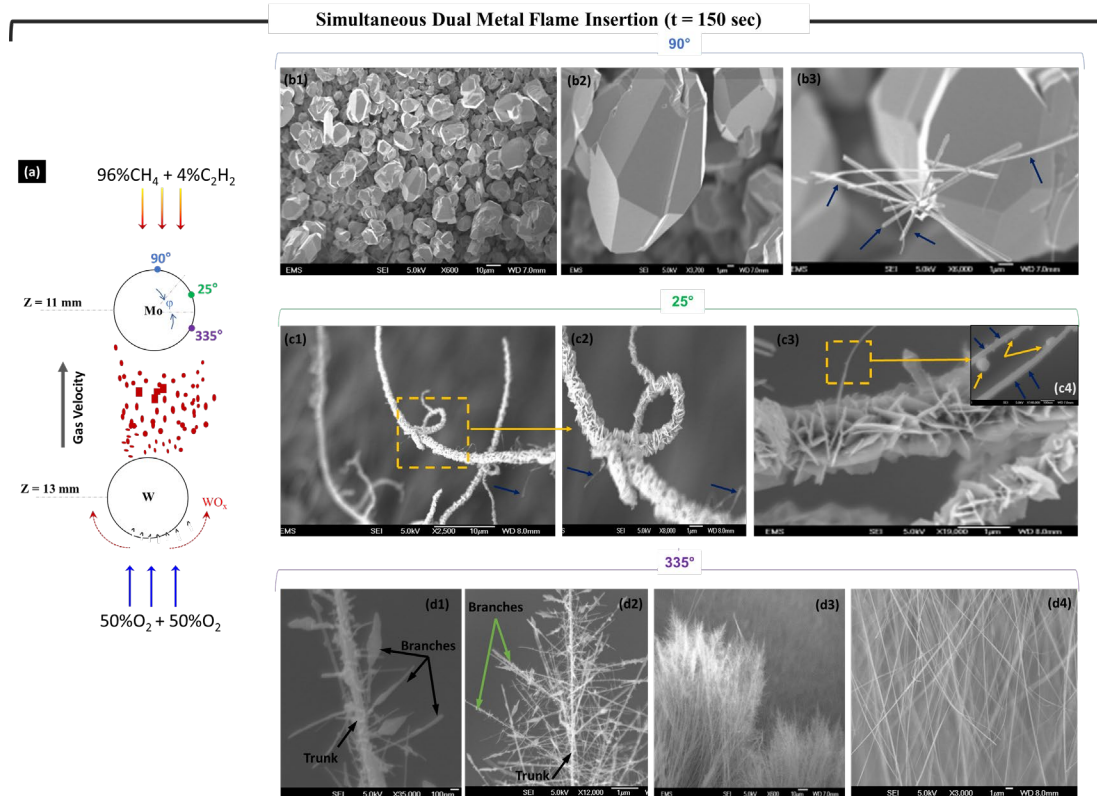
The increase of the residence time of the Mo and W probes simultaneously introduced into the flame volume resulted in the formation of structures with morphologies of higher complexity. The Mo and W probes were introduced at the flame positions  $Z = 11\text{mm}$  and  $13\text{ mm}$ , respectively, during a total flame residence time  $150\text{ sec}$ . Evidently, the increased probe-flame interaction time resulted in larger layer of deposits on the Mo probe surface, particularly at the crystallization sites located at the  $25^\circ$  and  $335^\circ$  sites, see schematic in **Fig. 25a**. SEM images of the deposits located at the  $90^\circ$  crystallization site reveal the presence of highly dense polyhedral-like structures, **Fig. 25(b1)**. The increased crystallization of metal oxide vapors on the sides of the Mo probe (i.e.  $25^\circ$  site) prevents further deposition of material on the top surface of the wire (i.e. at the  $90^\circ$  site). As a result, the structures deposited on the fuel side of the Mo-probe evolved into micro-polyhedrons of  $6$  to  $30\ \mu\text{m}$  and up to  $20$  facets (**Fig. 3b2**). Interestingly, a few rod-like structures are still observed within the polyhedral structures, however, indicating that the 1D nanorods are synthesized along the polyhedral structures and don't appear to serve as the "backbone" materials for the fabrication of polyhedral structures when both probes are introduced into the flame media simultaneously for  $150\text{ sec}$  (arrows in **Fig. 25(b3)**).

Well-defined flower-like structures were deposited at  $25^\circ$  crystallization site on the Mo probe. **Figs. 25(c1-c4)** depicts representative SEM images of the flower-like structures (with average flower size of  $1.2\ \mu$  and flat petals with characteristic dimensions in the order of  $755\text{ nm}$  and average thicknesses of  $40\text{ nm}$ , **Fig. 25(c3)**). Interestingly, this type of structures is only observed at crystallization sites containing the largest deposition rates.

The arrows in **Figs. 25(c1-c4)** depict the individual 1D structures serving as the “backbone” structures that allows further oxide vapors to crystallize along the high aspect ratio 1D nanorod at multiple locations, which then favors the growth of the multiple layers of petal-like structures or nanosheets, **Fig. 25(c4)**. The nanoflowers represent a high density of nanosheets distributed in multiple directions (12 to 15 petals per  $1 \mu\text{m}^2$  of surface area); thus, highly increasing the structures’ surface to volume ratio.

Further SEM imaging of the Mo probe surface at the lower crystallization sites at the  $335^\circ$  location shows morphologies resembling the early “nanotree-like” structures attained during the probe-flame interaction time of 60 seconds, **Fig. 25(b1-b5)**. Nevertheless, the “nanotree-like” structures formed after the prolonged flame exposure time closely resembles forest-like structures, **Fig. 25(d1-d4)**. SEM imaging “nanotree-like” structure reveals that the branches have deposits resembling platelet-like structures at the tip of the branches, **Fig. 25(d1-d2)**. Further analysis indicates that the forest structures consist of trees with trunks of lengths ranging up to  $190 \mu\text{m}$  and branches and trunks with diameters up to  $200 \text{ nm}$ .

Various studies address the synthesis and applications of polyhedron-like nano- and micro-materials. Zhao et al. [298] reported the synthesis of 26-facet  $\text{Fe}_2\text{O}_3$  nanocrystals by directly combusting solutions of metal-organic compounds. With this technique, uniformity is attained at the expense of production rate when compared to other flame methods such as spray flame synthesis. Other methods involve solution routes that include multiple steps and can require numerous hours [299,300]. It should be noted that flowers- and forest-like engineered structures are synthesized in highly dense arrays and thus their morphologies can have advantages in bulk heterojunction systems [301].



**Fig. 25.** Synthesis of polyhedron and forest-like structures after both probes being introduced into the flame volume for a residence time of 150 sec. (a) schematic of the dual insertion of Mo and W probes into the flame medium at flame positions of  $Z=11\text{mm}$  and  $Z=13\text{mm}$ , respectively, along with the location of the crystallization sites; (b1-b3) SEM images of the polyhedral structures synthesized on the fuel side of the Mo-probe at the  $90^\circ$  site; (c1-c4) SEM images of flower-like complex structures deposited at the  $25^\circ$  crystallization site; (d1-d4) SEM images of the tree- and forest-like complex structures crystallized at the  $335^\circ$  site.

#### 7.4 Variable Dual-Metal Flame Insertion at Different Flame Zones to Fabricate Nano and Micron Scaled Heterostructures

The metal probes insertion and flame residence times were varied and tailored to gain further insight into the synthesis mechanism of the multiplicity of morphologies formed. The Mo probe was introduced in the flame medium at  $Z = 11\text{ mm}$  by itself for 90 sec. Immediately after, a W probe was introduced in the flame at  $Z = 13\text{ mm}$  for times ranging from 30 to 60 sec, while retaining the Mo probe inside the flame volume (**Fig. 26**).

A schematic depicting the variable dual-metal insertion setup along with the graphical representation of the crystallization sites evaluated on the surface of the Mo probe is displayed in **Fig. 26a**. SEM imaging conducted on the surface of the Mo probe reveals the variation of the formed structures with increasing flame residence time and the location of the crystallization sites on surface of the Mo probe. The introduction of the Mo probe by itself for 90 sec allowed for 1D rod-like structures to be initially formed on the upper surface of the probe. Subsequent insertion of the W probe into the flame media while keeping the Mo wire in the flame media during additional 30 sec, results in the formation of 1D rod-like structures with deposits in the form of foxtail-like plumes predominately towards the tips of the 1D nanorods resembling grass-like morphologies. The nanogras structures have an average length of 50  $\mu\text{m}$  and diameter of 180 nm, **Figs. 26(b1-b2)**. Higher resolutions SEM analysis of the deposits indicate that they are formed of randomly oriented and truncated 1D nanorods with diameters and lengths ranging 14 to 66 nm and 155 to 560 nm, respectively, **Fig. 26(b3)**. The average diameter of the foxtail-like plumes is approximately 1.35  $\mu\text{m}$  with lengths of 3  $\mu\text{m}$ , **Fig. 26(b2)**.

Additional increase of the residence time after exposure of the W probe to 60 sec resulted in a multiplicity of morphologies deposited at different crystallization sites on the surface of the Mo probes. SEM imaging of the deposits at the 90° site suggest that the formation of large polyhedral structure is always connected to a nanorod as pointed out by the blue arrows in **Fig. 26(c1)**. At this location the polyhedral structures are composed of well-defined edges and flat surfaces **Fig. 26(c2)**. The “backbone” or nanorod structure attached to the polyhedral visibly resembles a “lollipop” morphology. Interestingly, having the polyhedral structures suspended by a rod indicates that the 1D nanorods are grown prior

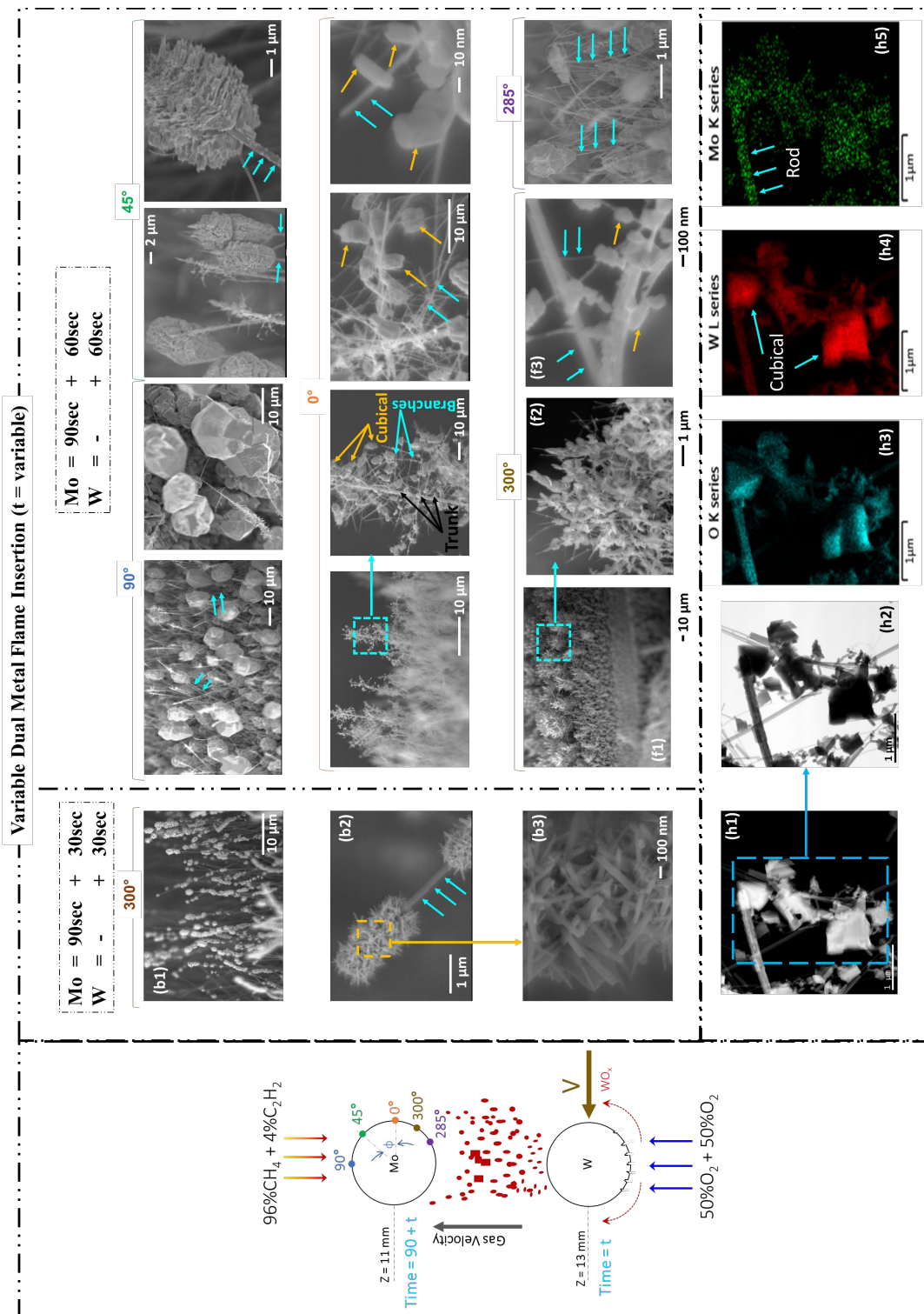
to the polyhedral structure, specifically during the first 90 sec when solely the Mo probe was exposed to the flame. During the sole insertion of the Mo wire into the flame medium, a Mo oxide layer is formed around the metal probe due to quick interaction with the oxygen rich chemical species of the counter-flow flame. The oxide layer was rapidly sublimated or evaporated, creating molybdenum-oxide vapors carried by the gas flow in the direction of the stagnation plane to crystallize in the form of 1D nanorods on the upper side of the probe exposed to lower temperatures that favored crystallization of the oxide vapors. It should be noted that the temperature gradients along the probe surface (i.e., bottom to top surface of the probes) could not be measured considering the spatial resolution of the pyrometers employed is in the order of 1 to 2 mm. Interestingly, the “lollipop”-like structures with polyhedral tips contrast to the polyhedral structures presented in Section 7.3, when the probes were introduced simultaneously into the flame volume, since imaging results thereof revealed that the polyhedrons are not grown on the nanorod, **Fig. 25(b1-b3)**. However, evaluation of the deposits at the 45° crystallization site illustrates similar polyhedral structures with “lollipop”-like morphology with the not well defined edges, and rather irregular surfaces of the polyhedrons primarily due to the excess of tungsten-oxide vapors tending to crystallize at higher rates as the sites closer to the side of the probes favored by the gas flow around the cylindrical probe, **Fig. 26(d1-d2)**. Remarkably, the 1D nanorods are confirmed to support the irregular polyhedral structures, **Fig. 26(d2)**. SEM imaging of the deposits at the 0° crystallization site on the surface of the Mo probe shows the presence of “nanotree-like” structures decorated with a large number of small well-developed cubical structures, **Fig. 26(e1-e4)**. The tree-like structures are composed of the trunk with multiple branches decorated with the cubical structures, **Fig. 26(e2)**. The



branches are mainly 1D rod-like structures (blue arrows in **Fig. 26(e2-e4)**) decorated with well-defined cubical structures characteristic of tungsten-oxide deposits carried by the gas-phase, yellow arrows in **Fig. 26(e2-e4)**. Further imaging analysis of the deposits crystalized at the 300° site reveal the structures are composed of highly dense “nanotree-like” structures, **Fig. 26(f1)**. Higher resolution imaging of the boxed area in **Fig. 26(f1)** shows that the formed “nanotree-like” structures’ branches are less densely adorned with cubical structures, **Fig. 26(f2-f3)**. It is noteworthy to note that imaging analysis of the deposits located that 285° crystallization site are composed of highly irregular defined polyhedrons suspended on nanorods, **Fig. 26(g)**. It is anticipated that the structures formed on the surface of the Mo probe facing the oxide side are purely made of tungsten-oxide. As the Mo probe is inserted first into the flame medium rich in oxygen species, a molybdenum-oxide layer immediately forms, then as a result of the high temperature gradients, the oxide layer evaporates and sublimates from the bottom surface of the probe and crystalizes downstream a lower temperature sites in the form of nanorods. The evaporation of the oxide layer from the oxidizer side of the probe results in high material erosion, thus, confirming there is no formation of structural species on the oxidizer side of the Mo probe, **Fig. 23(a2)**. However, once the W probe is introduced, the material evaporated/sublimated from the W probe will be carried by the gas flow and crystallize on the Mo probe in the form of the 1D nanorods with polyhedral-like tips on the lower side of the Mo probe.

Low resolution TEM images of the samples collected from the deposits resulted from experiments varying the insertion of the two metal probes into the flame media are show in **Fig. 26 (h1-h2)**. TEM-EDX elemental mapping performed on the collected samples indicated that the formed nanostructures have uniform and major contributions of

W and O, **Fig. 26(h3-h4)**. Interestingly, the Mo content is present in lower levels; however, its greater magnitude is observed at the 1D nanorod host or “backbone” structures (see arrows in **Fig. 26(h5)**), which further supports the hypothesis that the “backbone” or host 1D structures are formed during the first 90 seconds of exposure to the flame environment and appear to be primarily composed of molybdenum-oxide.



**Fig. 26.** Synthesis of heterostructures after varying the insertion and residence time of the metal probes. a) schematic of the variable insertion of Mo and W probes into the flame medium at flame positions of  $Z=11\text{mm}$  and  $Z=13\text{mm}$ , respectively, along with the location of the crystallization sites; (b1-b3) SEM imaging of the grass-like

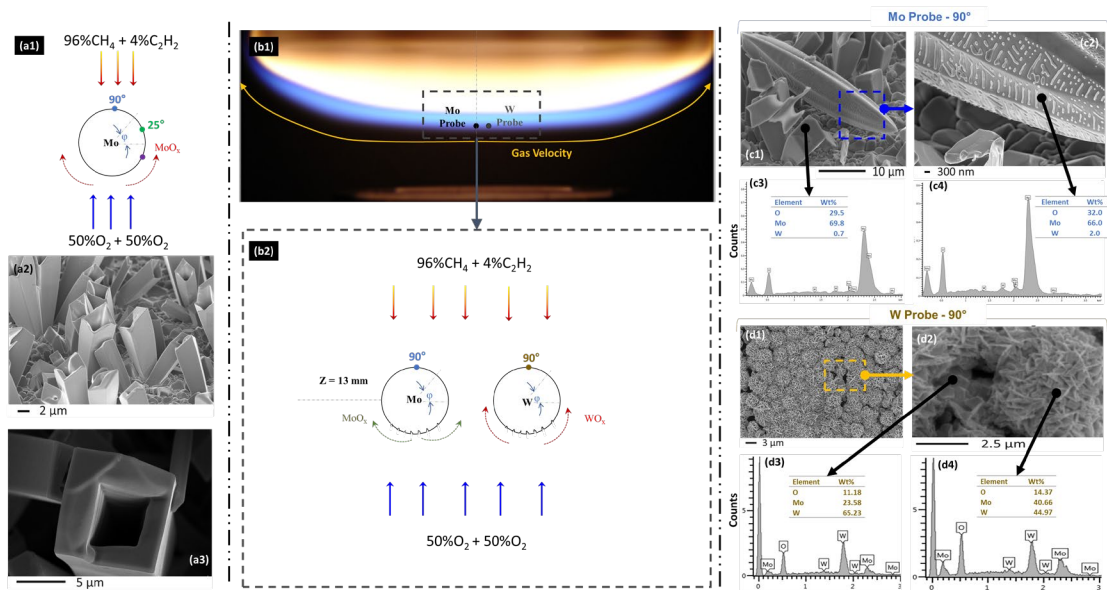
*heterostructures with the Mo probe inserted first in the flame (Z= 11mm) for 90 sec by itself, followed by the introduction of the W probe (Z = 13 mm) for 30 sec while the Mo probe was maintained inside flame region; SEM imaging of the heterostructures formed when the Mo probe inserted first in the flame (Z= 11mm) for 90 sec by itself, followed by the introduction of the W probe (Z = 13 mm) for 60 sec while the Mo probe was maintained inside flame region (c1-c2) SEM imaging of polyhedron structures synthesized at 90° site; (d1-d2) polyhedral heterostructures deposited at the 45° crystallization site; imaging of tree-like structures with high (e1-e4) and low (f1-f3) density of cubical deposits on their 1D rod-like branches; (g) SEM imaging of deformed or irregular polyhedrons suspended on nanorods; and (h1-h5) TEM imaging and EDX elemental mapping of the collected materials.*

## **7.5 Simultaneous Dual-Metal Flame Insertion at the Same Flame Zone to Fabricate Nano and Micron Scaled Heterostructures**

In an attempt to further understand the formation of the structures with complex morphologies, both the Mo and the W probe were introduced into the flame environment at the same flame location (Z = 13 mm), with the Mo probe position concentrically with the vertical symmetry plane of the counter-flow diffusion flame, **Figs. 27(b1-b2)**. Initially, the first phase of the assessment process consisted of evaluating the structures formed based on the single introduction of the Mo probe at flame location of Z = 13 mm within a flame environment rich in oxygen species and a temperature of 2410°C, **Fig. 27(a1)**. The single Mo probe insertion in the flame media resulted in the synthesis of high dense 3D solid and hollow rectangular structures with wall thicknesses ranging from 250 nm to 3.5  $\mu\text{m}$ , cross sectional areas ranging from 2.8 to 18.1  $\mu\text{m}^2$ , along with sharp edges, **Fig. 27(a2-a3)**. These morphological attributes make these structures particularly suitable for medical and biological applications [174]. The second phase of the assessment process involved the introduction of both metal wires into the flame medium at the same flame location (Z = 13 mm), which resulted in the formation structures of different morphologies driven by geometric position of the probes in the flame volume, **Figs. 27(c1-c2, d1-d2)**. The

introduction of the Mo probe aligning with the vertical symmetry plane of the flame suggests the transport of molybdenum-oxide vapors towards the W probe and minimizes the transport of tungsten-oxide vapors towards the Mo wire as a result of the gas flow direction characteristic of the 1D counter-flow diffusion flame employed. This makes the location and orientation of the probes highly critical factors to the end morphology and chemical composition of the formed structures. **Fig. 27(c1-c2)** depicts the formation of 3D structures on the Mo probe surface (i.e. 90° crystallization site) with full and hollowed rectangular structures similar to those attained from the single insertion of the Mo probe in the flame volume. The rectangular structures were accompanied by dendritic structures with lengths of 38  $\mu\text{m}$ , multiple facets with pointy tip morphology, **Fig. 27(c1-c2)**. Localized SEM-EDX analysis on both formed structures (i.e. rectangular- and dendritic-shaped) revealed the synthesized materials are made primarily of molybdenum-oxide with traces of W (**Fig. 27(c3-c4)**), which further supports the fact that the tungsten-oxide vapors reaching the Mo probe are minimax as they would be going against the gas flow based on the geometrical positioning of the Mo probe concentric to the vertical symmetry plane of the flame, **Fig. 27(b1)**. Further analysis of the structures formed on the W probe surface (i.e. 90° crystallization site) as a result of the dual metal insertion at the same flame position indicated the formation of highly dense flower or rose-like structures assembled from thin nanosheets or nanopetals with thickness and lengths ranging from 50 to 100 nm and 86 nm to 1.2  $\mu\text{m}$ , **Fig. 27(d1-d2)**. Localized SEM-EDX on the formed rose-like structures confirms the structures are hybrid in nature with chemical composition being composed of both tungsten and molybdenum-oxides, **Fig. 27(d3-d4)**. The EDX results confirmed that W drives the chemical composition of the formed structures as a result of its higher

oxidation rates despite Mo and Mo oxides having lower melting and evaporation points and being exposed to the same flame temperatures. The results attained from the dual metal insertion at the same flame location further confirms the deposits forming the heterostructures and materials with complex morphologies are composed primarily of tungsten-oxide due their higher oxidation and erosion rates.



**Fig. 27.** Synthesis of the complex and hybrid structures resulted from the single Mo and dual Mo/W probes insertion in the flame at  $Z = 13$  mm. (a) Schematic of the single insertion of the Mo probe in the flame at  $Z = 13$  mm; (a2-a3) SEM images of the rectangular molybdenum-oxide nanostructures resulted from the single insertion of the Mo probe in the flame medium; (b1) photograph of the counter-flow diffusion flame and the location of the Mo and W probes both inserted at  $Z = 13$  mm; (b2) schematic of the dual metal probe insertion in the flame medium at the same location; (c1-c2) SEM images of the formed structures on the Mo probe surface resulted from the dual probe insertion in the flame; and (c3-c4) localized SEM-EDX results thereof; (d1-d2) SEM images of the formed structures on the W probe surface resulted from the dual probe insertion in the flame; and (d3-d4) localized SEM-EDX results thereof. Adapted from [217]. Note boxed area is not drawn to scale.

## 7.6 Characterization of the Formed Structures with Complex Morphologies

HR-TEM analyses were employed to characterize the internal morphology and composition of the deposits formed at the various crystallization sites. TEM imaging of the tree-like structures is shown in **Fig. 28(a1-a3)** after the simultaneous exposure of the Mo and W probes to the flame media for 30 sec. These images further suggest that 1D nanorod structures are formed during the early fabrication stages and serve as the host structures, followed by additional crystallization of oxide species at multiple locations along the 1D “backbone” structure to form multiple branches (**Fig. 28(a1-a2)**). The evident discontinuity between the host core or trunk material and the branches (**Fig. 28(a2)**) further confirms that the structures are not simultaneously synthesized and thus the branches occurred as a result of continued exposure to the flame environment. HR-TEM imaging of the branches indicates the characteristic morphology of the tip of the structures is cylindrical in nature, **Fig. 28(a3)**. HR-TEM imaging and evaluation of the lattice d-spacing of the trunk or 1D “backbone” structure and the branches are made of materials of similar crystal structures or lattice patterns, both resulting in d-spacings of 0.38 nm, which closely corresponds to the (002) plane of monoclinic  $\text{WO}_3$ , measurements in **Fig. 28(a2-a3)** inserts.

The increase of the residence time of the metal probes to 60 sec resulted in the formation tree-like structures with nearly  $90^\circ$  branches formed from the core trunks, **Fig. 28(b1)**. Further inspection of the tip of the rod-like branches indicates the presence of branches (blue arrows in **Fig. 28(b2)**) and cubical-like deposits (**Fig. 28(b2)**-insert) characteristic of the tungsten-oxide cubical structures formed in the gas-phase, further confirming the structures are made of tungsten-oxide **Fig. 26(e3)**. The blue arrows in **Fig. 28(b3)** depict how additional material is deposited on the 1D structures to form the branch-

like materials taking place after initial formation of rod-like structures. Interestingly, additional examination of the synthesized structures present well-defined lattice structures with d-spacing of 0.38 nm, characteristic of  $\text{WO}_3$ , **Fig. 28(b3)**-insert.

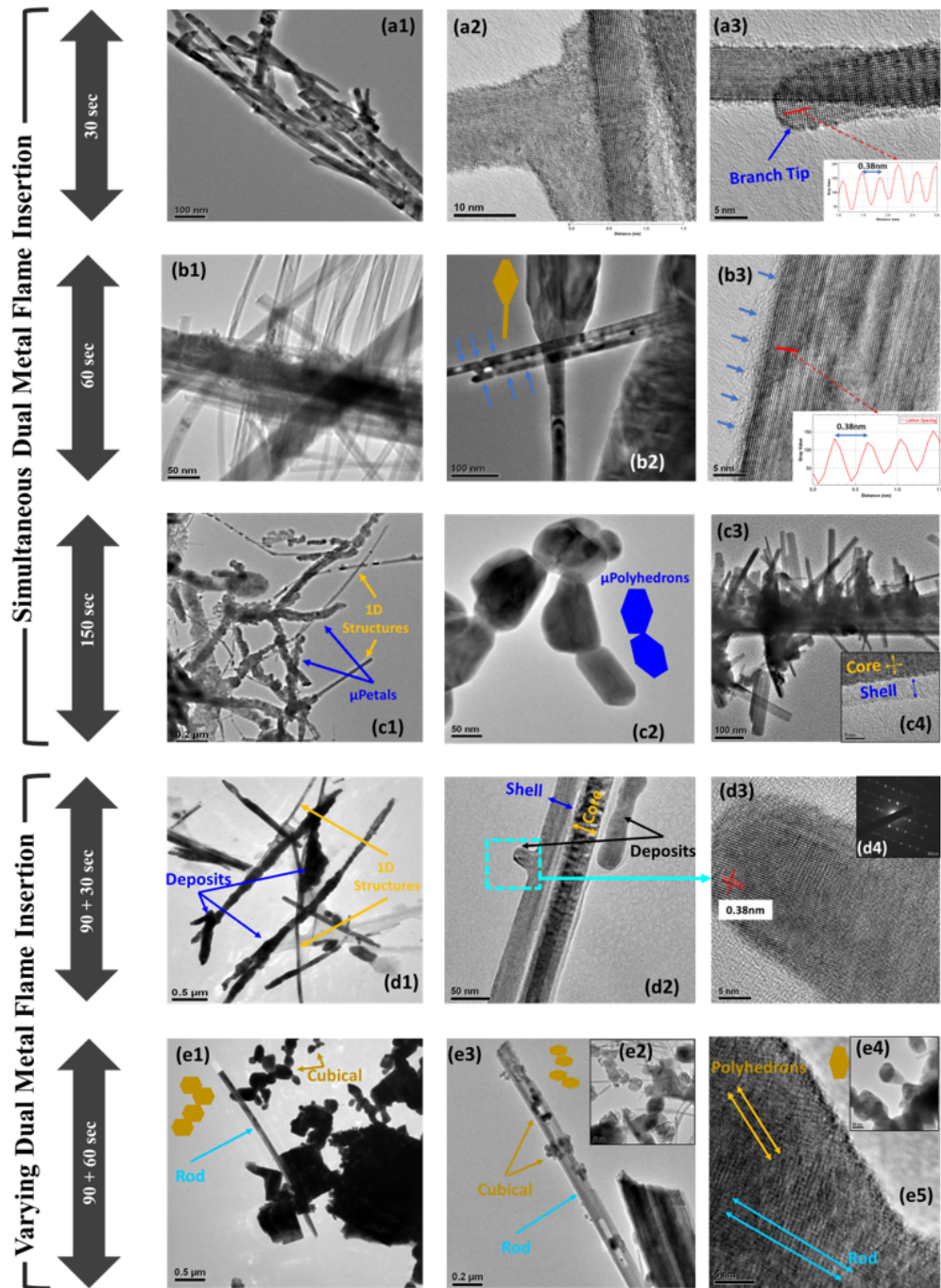
Increasing the exposure time of both probes simultaneously inserted into the flame to 150 sec results in flower-, polygonal-, and clear core and shell-like configurations, **Fig. 28(c1-c4)**. The flower-like structures are composed of core 1D nanorods with aggregates forming micron-sized cubical petals truncated at different angles to form flower-like morphology, **Fig. 28(c1)**. Whereas the polygonal structures do not seem to present the precursor 1D nanorods however, indicating that the 1D structures are synthesized along the polyhedral structures and don't appear to serve as the "backbone" materials for the fabrication of the nano- and micro-polyhedrals when both probes are introduced into the flame media simultaneously, **Fig. 28(c2)**. Furthermore, the core/shell configurations are representative of the forest structures, **Fig. 28(c3)**, with the core presenting dual lattice configurations distributed orthogonally; whereas the edges present a single lattice configuration extended in a single direction, **Fig. 28(c4)**. The core/shell structures and the complexity of the lattice configuration within a single structure further supports the degree of complexity of the formed materials. The clear physical interface between the two apparent dissimilar structures is also known as a heterojunction [302]. The HR-TEM image of these samples clearly reveals the heterostructure junction along the axial direction of the rod, **Fig. 28(c4)**.

Even greater degrees of morphological complexity of the structures formed are attained by varying the time and duration at which the metallic probes are inserted into the flame environment are attained based on the resulted morphologies (i.e. grass-like, trees



decorated with cubical structures and “lollipops” with polyhedrons heads), **Fig. 28(d1-e5)**. Maintaining the Mo probe inside the flame volume by itself for 90 sec allows for the formation of the 1D “backbone” structures, **Fig. 28(d1)**. This is then followed by the continuous deposition of tungsten-oxide on the surface of the 1D precursor structures forming core/shell configurations with deposits of randomly oriented and truncated 1D nanorods forming the grass-like structures, **Fig. 28(d1-d2)**. Higher resolution TEM imaging depicts the core/shell configuration along with the early 1D deposits randomly extruding from the core plane **Fig. 28(d2)**. HR-TEM analysis of the boxed area in the **Fig. 28(d2)** reveals that the deposits present well-defined lattice structure with d-spacing of 0.38 nm, characteristic of  $\text{WO}_3$  (**Fig. 28(d2)**) with a high degree of crystallinity confirmed by the SAED pattern shown in **Fig. 28(d4)**. Further increasing the W probe residence time inside the flame medium after the single insertion of the Mo wire, results in tree-like structures with highly dense cubical deposits employing the 1D nanorods as “backbone” structures, see **Fig. 28(e1)** with schematic depicting the shape of the cubical structures. Higher resolution TEM imaging of the structures in **Fig. 28(e2)** further confirmed that the 1D “backbone” structures are first formed and then served as precursors for the cubical deposits, **Fig. 28(e3)**. Additionally, “lollipop”-like structures with polyhedral shaped tips (**Fig. 28(e4)**) were evaluated utilizing HR-TEM imaging. The resulting structures support the hypothesis that the 1D nanorods form the “backbone” of the complex structures, see blue arrows in **Fig. 28(e5)**. Moreover, additional complexity on the lattice configuration of the formed structures is also apparent with a clear boundary between structures with different lattice patterns (**Fig. 28(e5)**). The heterojunction is visible by following the

distinct patterns of the crystal nanostructure of the rod and polyhedral structure, **Fig. 28(e5)**.



**Fig. 28.** TEM images of structures resulted from simultaneously inserted Mo and W probes into the flame media for a duration of 30 (a1-a3), 60 (b1-b3), and 150 sec (c1-c4). And TEM images of structures resulted from Mo and W probes inserted at different times/durations into the flame environment (d1-e5).

## 7.7 Growth Mechanism

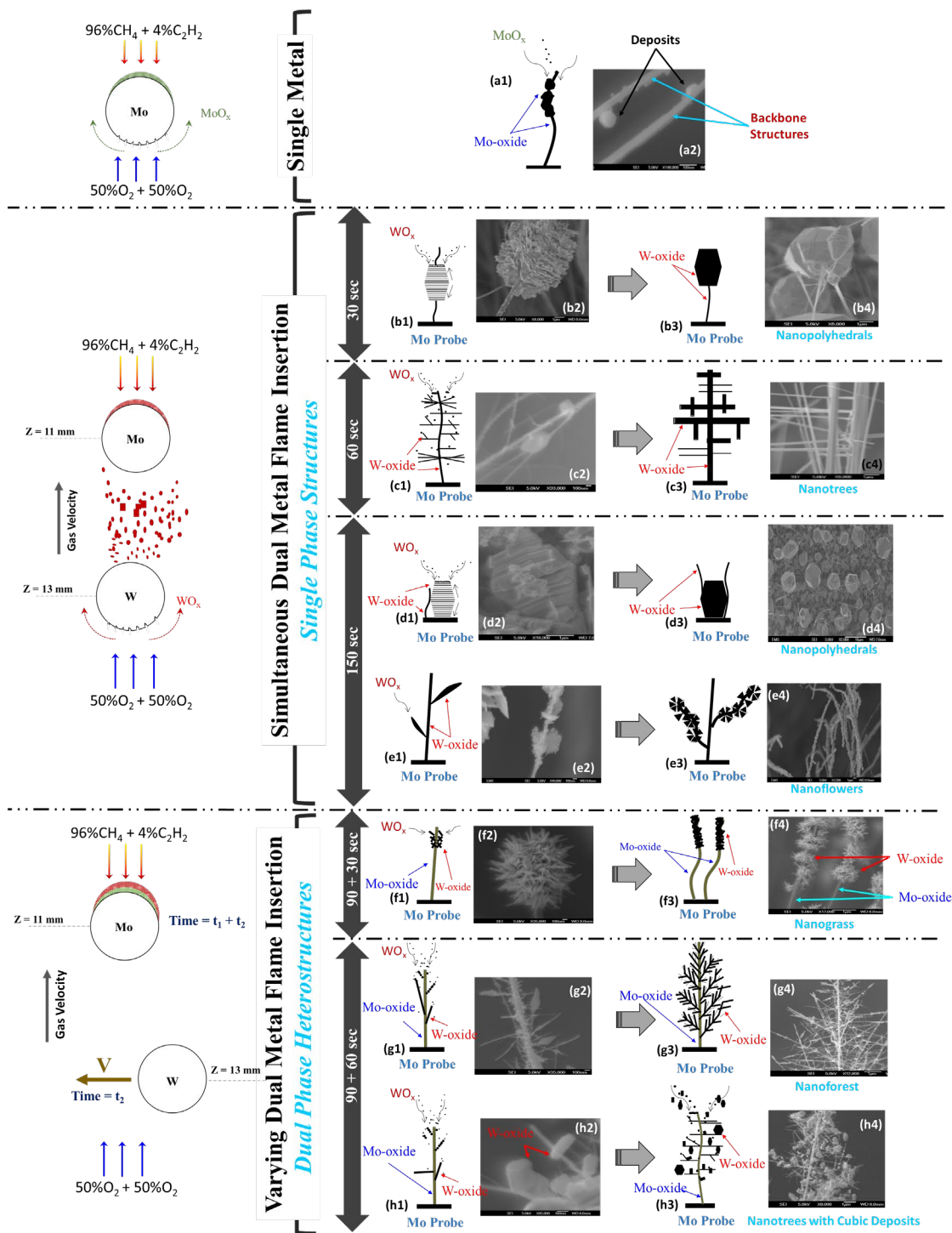
The fabrication of the heterostructures is driven by various factors including (i) the residence time of the metal probes in the flame medium, (ii) the probe position, and (iii) the sequence in which the probes are inserted into the flame volume (**Fig. 28**). The overall fundamental stages of the growth mechanics consist of three phases:

- i) Single metal flame insertion (Fig. 28(a1-a2)):* when the Mo or W probe is inserted by itself in the flame volume, the high flame temperature along with a region rich in oxygen radicals (oxidative environment) results in the formation of oxide layers coating the surface of the metal probe facing the oxidizer side. The experimental plan executed consisted of introducing the Mo and W probe at the flame positions of  $Z = 11$  and  $13$  mm, respectively. It should be noted that the melting temperature of molybdenum-oxides is typically lower than that of tungsten-oxides, therefore the W-wire placed at flame position with a gas temperature of  $\sim 2,480^{\circ}\text{C}$ ; whereas the Mo-wire was subjected to a lower temperature of  $\sim 2,150^{\circ}\text{C}$ . The actual probe temperatures measured with an optical pyrometer for the W and Mo probes are of lower magnitudes due to heat losses from radiation and axial conduction through the probe, with W and Mo measuring  $1,260^{\circ}\text{C}$  and  $1,200^{\circ}\text{C}$ , respectively.
- ii) Simultaneous dual metal flame insertion:* when both probes are inserted simultaneously in the flame volume the Mo probe mostly acts as a substrate for deposition and crystallization of the tungsten-oxide vapors, **Fig. 28(b1-e4)**. In this case, the tungsten-oxide layer coating the W probe commences to evaporate/sublimate and subsequently form the tungsten-oxide vapors, which are carried by the gas flow [303] downstream towards the Mo probe where they

crystallize to form the “backbone” structures, **Figs. 28(b1-b2,c1-c2,d1-d2,e1-e2)**. Results proved that complex structures can be formed within seconds, **Figs. 28(b1-e4)**. The concentration rate of oxide vapors tends to increase with decreasing probe diameter as it is exposed to longer residence times within the flame environment. Thereby, structures with even higher morphological complexity are formed, **Figs. 28(b3-b4,c3-c4,d3-d4,e3-e4)**. Previous reports indicate that when both a Mo and a W probe are exposed to an identical temperature and pressure environment (i.e. high temperature and oxygen rich flames), the W-based material yields a higher rate of oxidation [297]. Interestingly in this work, the W-wire is inserted at the higher temperature and oxygen concentration zone of the flame compared to that of Mo. As the W probe remains in the flame for longer periods of time, it results in higher saturation levels of tungsten-oxide vapors superimposing those of molybdenum-oxide.

*iii) Varying dual metal flame insertion:* when the Mo probe is inserted by itself for an elapsed time, followed by the W probe insertion. The pure metal probe reacts with the oxygen rich species in the flame environment forming a molybdenum-oxide layer, which starts to evaporate/sublimate yielding oxide vapors that are carried by the gas flow traveling in the direction of the stagnation plane. Those vapors will start to cool down and nucleate on the fuel side of the probe at lower temperatures. This first stage enables the formation of the 1D host or “backbone” structures on the lower temperature crystallization sites of the probe (**Figs. 28(f1,g1,h1)**). Once the W probe is introduced a tungsten-oxide layer will be formed and evaporated/sublimated and carried by the gas flow in the direction of the Mo probe

to form the complex heterostructures, **Figs. 28(f1-h4)**. The results indicate that the time of the introduction of the second probe ( $t_2$  in **Figs. 28** - varying probe dual metal flame insertion schematic) plays vital role for determining the type of structure formed. Nanoglass like heterostructures are formed when solely the Mo probe is inserted within the flame for 90 sec, followed by the insertion of the W probe into the flame for 30 sec while maintaining the Mo probe inside the flame volume, **Fig. 28(f1-f4)**. Increasing the W probe residence time to 60 sec while yet maintaining the Mo probe inside the oxygen-rich zone of the flame results in nanoforest (**Fig. 28(g1-g4)**) and nanotrees decorated with cubical deposits (**Fig. 28(h1-h4)**). Remarkably, increasing the residence time of the W probe inside the flame medium results in structures with higher morphological complexity, which is in alignment with the proposed synthesis mechanism. As shown in the results, the deposits crystallization site (i.e.  $0^\circ$  to  $359^\circ$  sites) on the probe surface is also important. It is noteworthy to state that regardless of the process the consistent factor is the presence of the “backbone” or 1D nanorods that serve as the host of oxide vapors for recrystallization on their surfaces forming the highly complex structures with a multiplicity of morphologies. However, the increased deposition of materials typically takes place on the lateral sides of the probes (i.e.  $0^\circ$  and  $180^\circ$  crystallization sites), hence, preventing further deposition of metal vapors downstream. Ultimately, allowing for polyhedral structures to be observed on the fuel side of the Mo probe surface even after prolonged residence times.



**Fig. 28.** Proposed growth mechanism of the various structures using the "solid support" single step method. (a1-a2) Mo probe inserted by itself in the flame medium; (b1-e3) Mo and W probes introduced simultaneously in the flame medium; (f1-h4) Mo and W probes are introduced in the flame volume at different times.

## 8. CHAPTER 8—CONCLUSIONS

There is a wide range of research on metal oxide nanostructures as a result of their remarkable properties resulted from tailored structures with unique morphologies and chemical compositions. However, the rise of potential applications in this field has resulted in the need of suitable synthesis methods that are inexpensive and rapid compared to traditional and current fabrication techniques.

Consequently, a holistic approach to understand how these structures are formed is necessary, along with the need to facilitate and optimize their production rates. Thereby, in this research we focused on gaining a comprehensive understanding of how these complex structures with unique morphologies are synthesized employing a single step and rapid fabrication technique. This technique consisted of employing a 1D counter-flow diffusion flame formed by the oxygen enriched oxidizer and methane seeded with 4% of acetylene as the fuel. The flame medium yielded temperature gradients up to 2000 K/cm and chemical species ranging from oxygen- to carbon-rich chemical species with the ability to form complex structures within less than 150 sec using highly pure transition metal probes as the precursor source.

The formed structures evolved from single oxide nanostructures with 1D, 2D, 3D and hybrid configurations (i.e. tungsten-oxide nanorods with carbon shells) to more complex structures with unique morphologies (i.e. polyhedron-, tree-, grass-, forest-, flower-like structures) resulted from dual simultaneous and variable insertion times of the W and Mo probes into the flame volume.

## 8.1 Conclusions

The single insertion of a 99.9% pure W probe into the oxygen enriched counterflow diffusion flame resulted in the synthesis of 1D, 2D, 3D and hybrid nanostructures on the solid support, along with octahedron nanoplatelets and rod-like nanocrystals in the gas-phase.

- Varying the diameter of the probe inserted into the counter-flow diffusion flame with a fuel consisting of 96% CH<sub>4</sub> doped with 4% C<sub>2</sub>H<sub>2</sub> and an oxidizer composed of 50% O<sub>2</sub> + 50% N<sub>2</sub>, resulted in the formation of 1D and 3D structures on the probe surface.
  - The insertion of a 1 mm diameter W probe in the flame medium at a flame location of Z = 12 mm resulted in the formation of 1D nanowires on the top surface of the probe. The 1D tungsten-oxide elongated structures presented needle-like shapes. The morphological characteristics of the grown structures included lengths up to 50 μm and diameters ranging from 10 to 100 nm. The nanowires contained a composite or hybrid configuration consisting of an inner core crystalline metal oxide material covered by an outer sheath formed of well-ordered carbon shells. The measured lattice spacing of the tungsten-oxide was 0.38 nm, which corresponds to the (002) plane of monoclinic WO<sub>3</sub>; whereas that of the outer shells was 0.34 nm, which corresponds to graphite. Varying the physical size of the shield resulted in various thickness of the carbon layer coating the metal oxide rods.
  - The reduction of the probe diameter to 0.5 mm inserted at Z = 11 mm within the flame with an oxidizer ratio of 50% O<sub>2</sub> + 50% N<sub>2</sub>, triangular, rectangular,



and cylindrical 3D WO<sub>3</sub> structures with hollow and semi-hollow configurations were formed on the upper surface of the probe.

- Increasing the oxygen content of the diffusion flame oxidizer resulted in the formation of 2D structures.
  - The use of a 1 mm diameter W probe and an oxidizer of 100% O<sub>2</sub> resulted in the growth of very thin, ribbon-like, micron-sized structures at a flame location of Z = 9 mm. The structures were synthesized on the sides of the probe rather than the upper surface. These WO<sub>3</sub> structures were about 80 nm thick.
- The different structure's morphologies observed from the various experimental conditions are explained by the variations of probe diameter and flame parameters. The smaller probe diameter presented higher surface temperatures because of lower heat losses, and a pure oxygen oxidizer provided a much more energetic and higher temperature flame medium. Thus, it is suggested that the tungsten-oxide structures are formed by the gas flow transfer of the tungsten-oxides species from the lower probe surface exposed to high temperatures and their further crystallization on the upper probe surfaces located downstream at lower temperature zones.
- It is believed that the polygonal- and cylindrical-shaped 3D and 2D ribbon-like structures are grown by the lateral coalescence of tungsten-oxide 1D structures into tubular structures of multiple shapes, along with flat ribbon-like morphologies.
- Additional experiments were performed in order to attain further insight on controlling the thickness of the carbon sheath of the hybrid tungsten-oxide/carbon nanostructures.

- Experimental analysis indicated that the hybrid tungsten-oxide carbon nanowires resulted from the rapid growth of carbon shells on tungsten-oxide nanorods induced by the transport of hydrocarbon species from the fuel-rich zone of the flame during the probe removal process.
- The thickness of the carbon sheath was controlled by simply varying the removal procedure, i.e. diameter of the probe shield. Results indicated that the amount of the formed carbon cylinders surrounding the metal oxide nanorods decreased with reducing the shield diameter. Moreover, it was confirmed that metal oxide nanorods with no carbon shells were formed when lacking the utilization of the external shield.
- The ability to synthesize the structures directly in the gas-phase makes flames continuous single step methodologies ideal for volumetric or mass production, with the growth process requiring only few seconds.
  - tungsten-oxide elongated nanocrystals were grown in the flame gas-phase by introducing a solid precursor source in an opposed-flow methane/oxygen-rich flame with strong chemical and thermal gradients.
  - A solid high purity W wire of 1 mm in diameter was introduced in the high temperature oxygen-rich area of the flame and served as the metal oxide source.
  - A thermophoretic sampling technique was employed to directly collect samples of crystalized materials composed of nano and micron size structures at several flame positions. Samples collected at flame locations equal to that of the solid W wire probe showed the presence of early formed polygonal-

shaped structures along with ultra-small particles with irregular shapes. Whereas sample material collected further away from the surface of the W probe resulted in the presence of larger/elongated crystals with rod-like shapes.

- The structures of the synthesized nanoscale crystals have polygonal cross-sectional areas with lengths of several microns.
- The direct growth process of the nanocrystals in the flame gas-phase involved (i) the oxidation of the solid wire to form oxide layers on the surface of the probe exposed to the high temperature oxygen-rich environment. (ii) Evaporation of the outermost oxide layer, and the further decomposition and transfer of the metal oxide precursor from the side of the probe exposed to the high temperature oxygen-rich environment to zones with lower temperatures and reduced oxidant states on the fuel side, hence, creating ideal media for gas-phase synthesis. (iii) As the vaporized precursor travels in the gas flow towards the stagnation plane of the flame, tungsten-oxide structures are crystallized in the form of nanorods that can evolve into 3D structures with polygonal cross-sectional areas.
- EDX analysis revealed that the grown structures consist exclusively of tungsten and oxygen indicating that the materials are, indeed, composed of tungsten-oxide. HR- TEM analyses showed that the synthesized structures have a lattice d-spacing of  $\sim 0.38$  nm closely corresponding to the (002) plane of a monoclinic  $WO_3$  cell.

The dual simultaneous and varied insertion of both W and Mo probes into the oxygen enriched counterflow diffusion flame resulted in the synthesis of micron- and nano-scaled tungsten/molybdenum-oxide controllable hierarchical structures.

- The gas flame synthesis of the structures consists of four critical phases: (i) the introduction of high purity metals (i.e. bulk source) in the form of 1 mm diameter wires into the oxygen-rich region of the flame. The resulting chemical reactions at the surface of the probes result in the formation of oxide layers. (ii) The thermal decomposition of the oxide layers via evaporation/sublimation results in oxide vapors or precursors. (iii) The process is followed by the nucleation and synthesis of host nanorods or “backbone” structures on the surface of uppermost probe. (iv) Vapors or precursors from the lower regions of the probes reach the fuel side surface of the probe to nucleate and grow new structures on the firstly fabricated “backbone” nanorods to form complex structures.
- Tuning the insertion and exposure time of the metal probes into the flame media resulted in heterogeneity of the formed structures.
  - The simultaneous insertion of both probes (Mo and W) resulted in the formation of single phase structures with a multiplicity of complex morphologies consisting of nanopolyhedrals, nanotrees, and nanoflowers.
  - HR-TEM analysis confirmed the structures were made of  $\text{WO}_3$  by measuring the well-defined lattice structures with a d-spacing of 0.38 nm. The formation of  $\text{WO}_3$  structures was favored by the higher oxidation rates of W when compared to Mo; thus, the formed tungsten-oxides controlled the formation of precursors and drove the crystallization process.

- The variation of the insertion of the Mo and W probe in the flame medium resulted in dual phase heterostructures consisting of molybdenum-oxide 1D host nanorods with tungsten-oxide multi-morphological deposits forming grass-, forest-, and trees with cubical deposits-like heterostructures. SEM, TEM, EDX, and SAED results confirmed the morphological and chemical characteristics of the structures.

## **8.2 Recommendations for Future Work**

Among the numerous TMOs, tungsten- and molybdenum-oxides are of special interest and of great importance due to their superconducting, photochromic, electrochromic, optochromic, and gaschromic properties. This broad number of properties makes them materials of increasing interest for the scientific and technological world. Nanoscale tungsten/molybdenum-oxide structures have a wide number of applications such as smart windows, field emission, fuel cells, catalysts, optical devices, gas sensors, batteries, solar panels, etc. This research can be further extended by evaluating the applicability of the different fabricated structures in some of the applications mentioned above. Primarily, with sustainability playing a key role in today's world dynamics, solar panels and batteries are the two initially suggested applications of interest. Specifically:

- i. Evaluating the electrochemical properties of Mo/W nanoscale heterostructures to understand their behavior as electrode materials in Li-ion batteries. Techniques such as cyclic voltammetry, galvanostatic charge-discharge cycling, and electrochemical impedance spectroscopy can be used to investigate their specific capacitance, charge/discharge rate capability, and cycling stability.

- ii. Employing techniques such as electrical conductivity measurements, electrochemical impedance spectroscopy, and optical spectroscopy to investigate the charge transport and light absorption properties of the heterostructures for solar panel applications.

Moreover, modeling the mathematical framework to synthesize the multiplicity of morphologies synthesized in this research is of great importance to further tailor and control the formed structures. Among the models that can be evaluated: (i) nucleation model—accounting for the concentration, precursor saturation and growth mechanisms; and/or reaction-diffusion model—considering the evolution of concentration, nucleation, and morphology based on space and time. These models will also allow for assessing the and the yield rates of each characteristic structural morphology and what factors contribute to increase their production rates.

Another complementary extension to this research consists of developing a method to produce and collect large quantities of the tailored heterostructures in the flame gas-phase and solid support. Considering the historically high potential of flames as a nanoscale structure synthesis method for mass production, it is critical to enhance the material collection techniques.

## REFERENCES

- 
- [1] C.N.R. Rao and V. Subbarao. 1974. *Transition Metal Oxides - Crystal Chemistry, Phase Transition and Related Aspects*, NSRDS-NBS Monogr. 49. Washington, D.C.: Natl. Bur. Stand.
- [2] D.J. Shanefield, *Organic Additives and Ceramic Processing: With Applications in Powder Metallurgy, Ink, and Paint* / by Daniel J. Shanefield. 2nd ed. Boston: Kluwer Academic, 1996. Print.
- [3] N. Baig, I. Kammakam, and W. Falath, Nanomaterials: a review of synthesis methods, properties, recent progress and challenges. *Mater. Adv.* 2 (2021) 1821-1871.
- [4] A. Nandagudi, S.H. Nagarajao, M.S. Santosh, et al., Hydrothermal synthesis of transition metal oxides, transition metal oxide/carbonaceous material nanocomposites for supercapacitor applications, *Materials Today Sustainability* 19 (2022) 100214.
- [5] E.C. Okpara, O.C. Olatunde, O.B. Wojuola, et al., Applications of Transition Metal Oxides and Chalcogenides and their Composites in Water Treatment: a review, *Environmental Advances* 11 (2023) 100341.
- [6] O.I. Sallam, M.M. Atta, E.O. Taha, et al., Synthesis and modification of photoluminescence and dielectric properties of novel fluorophosphate glass by incorporating different transition metal oxides for optoelectronic applications, *Optical Materials* 136 (2023) 113413.
- [7] Q. Shi, S. Deng, Y. Zheng, et al., The application of transition metal-modified biochar in sulfate radical based advanced oxidation processes, *Environmental Research* 212 Part B (2022) 113340.
- [8] H. Ye, G. Zheng, X. Yang, et al., Application of different carbon-based transition metal oxide composite materials in lithium-ion batteries, *Journal of Electroanalytical Chemistry* 898 (2021) 115652.
- [9] M. Gerloch, E.G. Constable. *Transition Metal Chemistry: the Valence Shell in the d-Block Chemistry*. Wiley-VCH Verlagsgesellschaft mbH, Weinheim (Federal Republic of Germany), 1994.
- [10] E. Crabb, E. Moore, L.E. Smart, *Concepts in Transition Metal Chemistry*. Published by Royal Society of Chemistry, 2010.
- [11] K.C. Patil, M.S. Hedge, T. Rattan, et. al., *Chemistry of nanocrystalline oxide materials: combustion synthesis, properties and applications*. Singapore: World Scientific Publishing Co. Pte. Ltd. (2008).
- [12] Z.R. Tian, J.A. Voigt, J. Liu, B. Mckenzie, M.J. Mcdermott, M.A. Rodriguez, H. Konishi, H. Xu. *Complex and Oriented ZnO Nanostructures*. *Nature Materials*, 2(2003) 821-826.
- [13] B. Pal, M. Sharon. *Enhanced Photocatalytic Activity of Highly Porous ZnO Thin Films Prepared by Sol-Gel Process*. *Mater. Chem. Phys.*, 76(2002)82-87.
- [14] Z.W. Pan, Z.R. Dai, Z.L. Wang. *Nanobelts of Semiconducting Oxides*. *Science*, 291(2001)1947-1949.

- 
- [15] H. Kind, H. Yan, B. Messer, M. Law, P. Yang. Nanowire Ultraviolet Photodetectors and Optical Switches. *Adv. Mater.*, 14(2002)158-160.
- [16] Y.Q. Huang, M.D. Liu, Y.K. Zeng, S.B. Liu. Progress of Study on ZnO Thin Films and its Properties. *J. Inorg. Mater.*, 16(2001)391-397.
- [17] P.M. Martin, M.S. Good, J.W. Johnston, L.J. Bond, S.L. Crawford. Piezoelectric Films for 100-Mhz Ultrasonic Transducers. *Thin Solid Films*, 379(2000)253-258.
- [18] R. M. Cornell and U. Schwermann, *The Iron Oxides: Structure, Properties, Reactions, Occurrence and uses*, Wiley–VCH, New York, 1996, p. 509.
- [19] N.A. Dhas, A. Gedanken. Sonochemical Synthesis of Molybdenum Oxide– and Molybdenum Carbide–Silica Nanocomposites. *Chem. Mater.* 9 (1997) 3144-3154.
- [20] M. Anpo, M. Kondo, Y. Kubokawa, C. Louis, M. Che. Dynamic Studies of the Photoinduced Metathesis of C<sub>3</sub>H<sub>6</sub> and Photoreduction of Mo with CO on Anchored and Impregnated Mo/SiO<sub>2</sub> Catalyst. *J. Chem. Soc. Faraday Trans.*, 184(1988)2771-2782.
- [21] Y. Liu, Y. Qian, M. Zhang, Z. Chen, C. Wang. Preparation of Nano-Sized Amorphous Molybdenum Dioxide Powders by Use of  $\gamma$ -Ray Radiation Method. *Mater. Res. Bull.* 31 (8) (1996) 1029-1033.
- [22] Jun Zhou, N.S. Xu, S.Z. Deng, Jun Chen, J.C. She. Synthesis of large-scaled MoO<sub>2</sub> nanowire arrays. *Chem. Phys. Lett.*, 382(2003) 443-446.
- [23] A. Gulino, S. Parker, F. H. Jones and R. G. Egdell. Influence of Metal–metal Bonds on Electron Spectra of MoO<sub>2</sub> and WO<sub>2</sub>. *J. Chem. Soc. Faraday Trans.*, 92 (1996)2137-2141.
- [24] Z.L. Wang, *Mater. Nanostructures of Zinc Oxide. Today*, 7(2004)26-33.
- [25] X. Marguetettaz, D. Fitzmaurice . *Heterosupramolecular Chemistry: Long-lived Charge Trapping by Vectorial Electron Flow in a Heterotriad.* *J. Am. Chem. Soc.*, 116(1994)5017.
- [26] M.C. Carotta, V.G. Ferroni , G. Martinelli. Preparation and Characterization of Nanostructured Titania Thick Films. *Advanced Materials*, 11(1999)943-946.
- [27] S.Y.Huang, L. Kavan, I. Exnar, M. Grätzel. Rocking Chair Lithium Battery based on Nanocrystalline TiO<sub>2</sub> (Anatase). *J. Electrochem. Soc.*, 142(1997)L142.
- [28] J. Graetz, C. C. Ahn, R. Yazami, B.Fultz. Highly Reversible Lithium Storage in Nanostructured Silicon. *Electrochem. Solid State Lett.*, 6(9)(2003) A194–A197.
- [29] H. Kim and J. Cho, Superior Lithium Electroactive Mesoporous Si@Carbon Core–Shell Nanowires for Lithium Battery Anode Material. *Nano Lett.*, 8 (11) (2008) 3688–3691.
- [30] S-H. Lee, Y-H. Kim, R. Deshpande, P.A.Parilla, E. Whitney, D.T. Gillaspie, K.M. Jones, A.H. Mahan, Z. Zhang,, and A.C. Dillon. *Adv. Mater.*, 20(2008)3627–3632.
- [31] J.Q. Xu, Q.Y. Pan, Y.A. Shun, Z.Z. Tian. Grain Size Control and Gas Sensing Properties of ZnO Gas Sensor. *Sensors Actuators B: Chem.*, 66(2000)277-279.
- [32] M. Ferroni, V. Guidi, G. Martinelli, P. Nelli, G. Sberveglieri. Gas-sensing Applications of W–Ti–O-based Nanosized Thin Films Prepared by r.f. Reactive Sputtering. *Sens. Actuators B*, 44(1997)499-502.



- 
- [33] D.E. Bergeron, A.W. Castleman Jr., N.O. Jones, S.N. Khanna. Stable Cluster Motifs for Nanoscale Chromium Oxide Materials. *NanoLetters*, 4(2)(2004) 261-265.
- [34] S.K. Singh, R. Chauhan. Study of Optical Properties of Transition Metal Oxides on the Basis of Energy Band and Energy State Analysis. *The International Journal of Engineering And Science (IJES)*, 3(6) (2014) 37-40.
- [35] G-C. Yi, C. Wang, W.II. Park. ZnO Nanorods: Synthesis, Characterization and Applications. *Semicond. Sci. Technol.*, 20(2005)S22-S34.
- [36] L. Tsakalakos. Nanostructures for photovoltaics. *Mater. Sci. Eng. Rep.*, 62 (6)(2008)175-189.
- [37] P.Q. Luo, E. Moulin, J. Sukmanowski, F.X. Royer, X.M. Dou, H. Stiebi. Enhanced Infrared Response of Ultra-Thin Amorphous Silicon Photosensitive Devices with Ag Nanoparticles. *Thin Solid Films* 517(2009) 6256–9.
- [38] E. Moulin, J. Sukmanowski, M. Schulte, A. Gordijn, F.X. Royer, H. Stiebig. Thin-film Silicon Solar Cells with Integrated Silver Nanoparticles. *Thin Solid Films*. 516 (2008) 6813–7.
- [39] J.A. Anta. Electron Transport in Nanostructured Metal-oxide Semiconductors. *Curr. Opin. Coll. Interface Sci.* 17(2012)124-131.
- [40] L. Zhou, C. Zhao, B. Giri, P. Allen, X. Xu, H. Joshi, Y. Fan, L. V. Titova, P. M. Rao. High Light Absorption and Charge Separation Efficiency at Low Applied Voltage from Sb-doped SnO<sub>2</sub>/BiVO<sub>4</sub> Core/Shell Nanorod-Array Photoanodes. *Nano Letters*, 16 (6): (2016) 3463-3474.
- [41] K Ernst, A Belaidi, and R Koenenkamp. Solar cell with extremely thin absorber on highly structured substrate. *Semicond. Sci. Technol.* 18 (2003) 475–479.
- [42] Z. Zhu, S. K. Iyemperumal. K. Kushnir, A. D. Carl, L. Zhou, D.R. Brodeur, R. L. Grimm, L. V. Titova, N. A. Deskins, P. M. Rao. Enhancing the Solar Energy Conversion Efficiency of Solution-deposited Bi<sub>2</sub>S<sub>3</sub> Thin Films by Annealing in Sulfur Vapor at Elevated Temperature. *Sustainable Energy & Fuels*. 1 (2017) 2134-2144.
- [43] T. Dittrich, D. Kieven, A. Belaidi, M. Rusu, J. Tornow, K. Schwarzburg, M. Ch. Lux-Steiner. Formation of the charge selective contact in solar cells with extremely thin absorber based on ZnO-nanorod/In<sub>2</sub>S<sub>3</sub>/CuSCN. *J. Appl. Phys.* 105 (2009) 034509.
- [44] I.A. Kuznetsov, M.J. Greenfield, Y.U. Mehta, W. Merchan-Merchan, G. Salkar, and A.V. Saveliev. Increasing the Solar Cell Power Output by Coating with Transition Metal-Oxide Nanorods. *Applied Energy*, 88(2011)4218–4221.
- [45] P. Ravirajan, A. M. Peiro, M. K. Nazeeruddin, M. Graetzel, D. D. C. Bradley, J. R. Durrant, and J. Nelson. Hybrid Polymer/Zinc Oxide Photovoltaic Devices with Vertically Oriented ZnO Nanorods and an Amphiphilic Molecular Interface Layer. *J. Phys. Chem. B* 110(2006)7635-7639.
- [46] C.G. Granqvist, Electrochromics for Smart Windows: Oxide-Based Thin Films and Devices, *Thin Solid Films*. 564 (2014) 1-38.
- [47] C.G. Granqvist, A. Azens, P. Heszler, L.B. Kish, L. Österlund, Nanomaterials for Benign Indoor Environments: Electrochromics for “Smart Windows”, Sensors for

- 
- Air Quality, and Photo-catalysts for Air Cleaning. *Solar Energy Materials and Solar Cells*, 91(4)(2007)355-365.
- [48] H. Matsuoka, S. Hashimoto, H. Kageshika, Lifetime of Electrochromism of Amorphous WO<sub>3</sub>-TiO<sub>2</sub> Thin Films, *Surf. Technol. (Japan)* 42 (2) (1991) 104-110.
- [49] E. György, A. Pérez del Pinto, Tunable optical and nano-scale electrical properties of WO<sub>3</sub> and Ag-WO<sub>3</sub> nanocomposite thin films. *J. Mater. Sci.* 46 (2011) 3560-3567.
- [50] K.W. Park, Y.-J. Song, J.-M. Lee, S.-B. Han, Influence of Pt and Au Nanoparticles on Electrochromism of WO<sub>3</sub> in Nanostructure thin-film Electrodes. *Electrochem. Commun.* 9 (2007) 2111-2115.
- [51] P.M. Kadam, N.L. Tarwal, P.S. Shinde, S.S. Mali, R.S. Patil, A.K. Bhosale, H.P. Deshmukh, P.S. Patil, Enhanced Optical Modulation due to SPR in Gold Nanoparticles Embedded WO<sub>3</sub> thin films. *J. Alloys Compd.* 509(2011)1729-1733.
- [52] R. Kirchgeorg, S. Berger, P. Schmuki, Ultra Fast Electrochromic Switching of Nanoporous Tungsten-tantalum Oxide Films. *Chem. Commun.* 47(2011)1000-1002.
- [53] V.K. Laurinavichute, S.Yu. Vassiliev, L.M. Plyasova, I.Yu. Molina, A.A. Khokhlov, L.V. Pugolovkin, M.I. Borzenko, G.A. Tsirlina, Cathodic Electrocrystallization and Electrochromic Properties of Doped Rechargeable Oxotungstates. *Electrochim. Acta* 54 (2009)5439-5448.
- [54] K. Sone, M. Yagi, Influencing Factors on Electrochromic Hysteresis Performance of Ruthenium Purple Produced by a WO<sub>3</sub>/Tris (2,2'-bipyridine) Ruthenium (II)/Polymer Hybrid Film. *Electrochim. Acta* 53(2008) 6535-6541.
- [55] S.V. Green, E. Pehlivan, C.G. Granqvist, G.A. Niklasson, Electrochromism in Sputter Deposited Nickel-containing Tungsten Oxide Films. *Sol. Energy Mater. Sol. Cells* 99 (2012)339-344.
- [56] K.M. Karuppasamy, A. Subrahmanyam, The Electrochromic and Photocatalytic Properties of Electron Beam Evaporated Vanadium-doped Tungsten Oxide Thin Films. *Sol. Energy Mater. Sol. Cells* 92(2008)1322-1226.
- [57] F. F. C. Bazito and R. M. Torresi. Cathodes for Lithium Ion Batteries: the Benefits of Using Nanostructured Materials. *J. Braz. Chem. Soc.*, 17(4)(2006)627-642.
- [58] A.C. Dillon, A.H. Mahan, R. Deshpande, P.A. Parilla, K.M. Jones, S-H. Lee. Metal Oxide Nano-particles for Improved Electrochromic and Lithium-ion Battery Technologies. *Thin Solid Films*, 516(2008)794-797.
- [59] S.H. Lee, Y.-H. Kim, R. Deshpande, P.A. Parilla, E. Whitney, D.T. Gillaspie, K.M. Jones, A.H. Mahan, S. Zhang, and A.C. Dillon. Reversible Lithium-Ion Insertion in Molybdenum Oxide Nanoparticles. *Adv. Mater.* 20(2008)3627-3632.
- [60] D. Wang, D. Choi, J. Li, Z. Yang, Z. Nie, R. Kou, D. Hu, C. Wang, L.V. Saraf, J. Zhang, I.A. Aksay, and J. Liu. Self-assembled TiO<sub>2</sub>-graphene Hybrid Nanostructures for Enhanced Li-ion Insertion. *American Chemical Society*, 3(4)(2009)907-914.
- [61] W. Dong, D.R. Rolinson, B. Dunn. Electrochemical Properties of High Surface Area Vanadium Oxide Aerogels. *Electrochem. Solid-State Lett.*, 3(10)(2000)457-459.

- 
- [62] X. Xu, W. Liu, Y. Kim, J. Cho. Nanostructured Transition Metal Sulfides for Lithium Ion Batteries: Progress and challenges. *Nano Today*, 9(2014)604-630.
- [63] J. Zhang, A. Yu. Nanostructured Transition Metal Oxides as Advanced Anodes for Lithium-ion Batteries. *Sci. Bull.*, 60(9)(2015)823-838.
- [64] Y. Wang, J. Guo, T. Wang, J. Shao, D. Wang, Y.W. Yang. Mesoporous Transition Metal Oxides for Supercapacitors. *Nanomaterials*, 5(4)(2015)1667-1689.
- [65] V. Subramanian, S.C. Hall, P.H. Smith, B. Rambabu. Mesoporous Anhydrous RuO<sub>2</sub> as a Supercapacitor Electrode Material. *Solid State Ionics*, 175(2004)511–515.
- [66] E. Comini, C. Baratto, G. Faglia, M. Ferroni, A. Vomiero, G. Sberveglieri, Quasi-one Dimensional Metal Oxide Semiconductors: Preparation, Characterization and Application as Chemical Sensors. *Prog. Mater. Sci.*, 54 (2009) 1-67.
- [67] S. Laurent, S. Boutry, R.N. Muller. Metal Oxide Particles and their Prospects for Applications (Chapter 1). Editors: Morteza Mahmoudi and Sophie Laurent, In *Metal Oxides, Iron Oxide Nanoparticles for Biomedical Applications*, Elsevier, 2018, Pages 3-42, ISBN 9780081019252.
- [68] G. Korotcenkov. Metal Oxides for Solid-State Gas Sensors: What Determines Our Choice? *Mater. Sci. Eng. B*, 139(2007)1- 23.
- [69] C.L. Zhu, Y.J. Chen, R.X. Wang, L.J. Wang, M.S. Cao, X.L. Shi. Synthesis and Enhanced Ethanol Sensing properties of  $\alpha$ -Fe<sub>2</sub>O<sub>3</sub>/ZnO Heteronanostructures. *Sens. Actuat. B* 2009, 140, 185–189.
- [70] T. Ghodselahi, H. Zahrabi, M. Heidari Saani, M. A. Vesaghi. CO Gas Sensor Properties of Cu@CuO Core Shell Nanoparticles Based on Localized Surface Plasmon Resonance. *J. Phys. Chem. C* 115(2011) 22126–22130.
- [71] C. Wang, L. Yin, L. Zhang, D. Xiang, R. Gao. Metal Oxide Gas Sensors: Sensitivity and Influencing Factors. *Sensors*, 10(2010) 2088-2106
- [72] A. Mirzaei, S. Park, H.J. Kheel, G.J. Sun, S. Lee, C. Lee. ZnO-capped Nanorod Gas Sensors. *Ceram. Int.*, 42(2016) 6187-6197.[73] B. Geng, C. Fang, F. Zhan, N. Yu. Synthesis of Polyhedral ZnSnO Microcrystals with Controlled Exposed Facets and their Selective Gas-Sensing Properties. *Small* 4(2008) 1337–1343.
- [74] Y.S. Kim, P. Rai, Y.T. Yu. Microwave Assisted Hydrothermal Synthesis of Au@TiO<sub>2</sub> Core–Shell Nanoparticles for High Temperature CO Sensing Applications. *Sens. Actuators B*, 186(2013)633-639.
- [75] K. Chung, C.-H. Lee, G.-C. Yi. Transferable GaN Layers Grown on ZnO-Coated Graphene Layers for Optoelectronic Devices. *Science*, 330(2010) 655-657.
- [76] D. Choi , M. Y. Choi , W.M. Choi, H. J. Shin, H. K. Park, J. S. Seo, J. Park, S.M. Yoon, S. J. Chae, Y. H. Lee, S.W. Kim, J.Y. Choi, S.Y. Lee, J.M. Kim. Fully Rollable Transparent Nanogenerators Based on Graphene Electrodes. *Adv. Mater.*, 22(19)(2010) 2187-2192.
- [77] J.H. Son, J.U. Kim, YH. Song, et al. Design Rule of Nanostructures in Light-Emitting Diodes for Complete Elimination of Total Internal Reflection. *Adv. Mater.*, 24(2012)2259–2262.

- 
- [78] N.T.S. Phan, C.S. Gill, J.V. Nguyen, Z.J. Zhang, C.W. Jones, Expanding the Utility of One-pot Multistep Reaction Networks Through Compartmentation and Recovery of the Catalyst. *Angew. Chem. Int. Ed.*, 45(2006)2209–2212.
- [79] Y. Li, D. He, Z. Cheng, C. Su, J. Li, Q. Zhu. Effect of Calcium Salts on Isosynthesis over ZrO<sub>2</sub> Catalysts. *J. Mol. Catal. A*, 175(2001)267–275.
- [80] H. Ataee-Esfahani, L. Wang, Y. Nemoto, Y. Yamauchi. Synthesis of Bimetallic Au@Pt Nanoparticles with Au Core and Nanostructured Pt Shell toward Highly Active Electrocatalysts. *Chem. Mater.*, 22(2010)6310-6318.
- [81] L. Wang, Y. Yamauchi. Metallic Nanocages: Synthesis of Bimetallic Pt–Pd Hollow Nanoparticles with Dendritic Shells by Selective Chemical Etching. *J. Am. Chem. Soc.*, 135(2013)16762-16765.
- [82] N. Tsolekile, S. Parani, M.C. Matoetoe, S.P. Songca, O.S. Oluwafemi. Evolution of ternary I–III–VI QDs: Synthesis, characterization and application. *Nano-Struct. Nano-Objects*, 12(2017)46–56.
- [83] N. Arsalani, A. Akbari, M. Amini, E. Jabbari, S. Gautam, K.H. Chae. POSS-Based Covalent Networks: Supporting and Stabilizing Pd for Heck Reaction in Aqueous Media. *Catal. Lett.*, 147(2017)1086–1094.
- [84] E. McFarland and H. Metiu. Catalysis by Doped Oxides. *Chem. Rev.* 2013, 113, 4391–4427.
- [85] J. Qu, L. Shi, C. He, F. Gao, B. Li, Q. Zhou, H. Hu, G. Shao, X. Wang, J. Qiu. Highly Efficient Synthesis of Graphene/MnO<sub>2</sub> Hybrids and their Application for Ultrafast Oxidative Decomposition of Methylene Blue. *Carbon* 66 (2014) 485–492.
- [86] LL. Liu, HX. Li, LM. Wan, et al. A Mn(III)–Superoxo Complex of a Zwitterionic Calix[4]arene with an Unprecedented Linear end-on Mn(III)–O<sub>2</sub> Arrangement and Good Catalytic Performance for Alkene Epoxidation. *Chem. Commun.*, 47(2011)11146-11148.
- [87] H. Rahaman, R. M. Laha, D.K. Maiti, S. K. Ghosh. Fabrication of Mn<sub>2</sub>O<sub>3</sub> Nanorods: an Efficient Catalyst for Selective Transformation of Alcohols to Aldehydes. *RSC Adv.* 5 (2015) 33923–33929.
- [88] A. Askarnejad, M. Bagherzadeh, A. Morsali. Sonochemical Fabrication and Catalytic Properties of  $\alpha$ -Fe<sub>2</sub>O<sub>3</sub> Nanoparticles. *J. Exp. Nanosci.*, 6(3)(2011)217–225.
- [89] D.A. Panayotov, S.P. Burrows, J.R. Morris. Photooxidation Mechanism of Methanol on Rutile TiO<sub>2</sub> Nanoparticles. *J. Phys. Chem. C*, 116(11)(2012)6623–6635.
- [90] C-J Jia, L-D Sun, Z-G Yan, L-P You, F. Luo, X-D Han, Y-C Pang, Z. Zhang and C-H Yan. Single-Crystalline Iron Oxide Nanotubes. *Angew Chem. Int. Ed.*, 44(2005)4328-4333.
- [91] L. Vayssieres, N. Beermann, S. E. Lindquist, A. Hagfeldt. Controlled Aqueous Chemical Growth of Oriented Three-Dimensional Crystalline Nanorod Arrays: Application to Iron(III) Oxides. *Chem. Mater.*, 13(2)(2001)233-235.
- [92] S. Chen, J. Feng, X. Guo, J. Hong and W. Ding. One-step Wet Chemistry for Preparation of Magnetite Nanorods. *Mater. Lett.*, 59(2005)985-988.

- 
- [93] T.A. Crowley, K.J. Ziegler, D.M. Lyons, D. Erts, O. Hakan, M.A. Morris, J.D. Holmes. Synthesis of Metal and Metal Oxide Nanowire and Nanotube Arrays within a Mesoporous Silica Template. *Chem. Mater.* 15(2003)3518-3522.
- [94] D.S. Xue, C.X. Gao, Q.F. Liu and L.Y. Zhang. Preparation and Characterization of Hematite Nanowire Arrays. *J. Phys.: Condens. Matter.*, 15(2003) 1455-1459.
- [95] C. Terrier, M. Abid, C. Arm, S. Serrano-Guisan, L. Gravier, J-P Ansermet. Fe<sub>3</sub>O<sub>4</sub> Nanowires Synthesized by Electroprecipitation in Templates. *J. Appl. Phys.*, 98(2005)086102-1-086102-3.
- [96] Z. Liu, D. Zhang, S. Han, C. Li, B. Lei, W. Lu, J. Fang and C. Zhou. Single Crystalline Magnetite Nanotubes. *J. Am. Chem. Soc.*, 127 (2005) 6-7.
- [97] Y. Ding, J. R. Morber, R.L. Snyder and Z.L. Wang. Nanowire Structural Evolution from Fe<sub>3</sub>O<sub>4</sub> to  $\epsilon$ -Fe<sub>2</sub>O<sub>3</sub>. *Adv. Funct. Mater.*, 17(2007)1172-1178.
- [98] J.R. Morber, Y. Ding, M.S. Haluska, Y. Li, J.P. Liu, Z.L. Wang and R.L. Snyder. PLD-Assisted VLS Growth of Aligned Ferrite Nanorods, Nanowires, and Nanobelts-Synthesis, and Properties. *J. Phys. Chem. B.*, 110 (2006)21672-21679.
- [99] J. Stringer. Oxidation of tantalum in oxygen-nitrogen and oxygen-inert gas mixtures. *Oxidation of Metals*, 11(5)(1977)225-239.
- [100] K. Ogata, K. Maejima, S.Z. Fujita, S.G. Fujita. Growth Mode Control of ZnO toward Nanorod Structures or High-quality Layered Structures by Metal-organic Vapor Phase Epitaxy. *J. Cryst. Growth*, 248(2003)25-30.
- [101] A.Varma, A. S. Mukasyan, A.S. Rogachev, and K. V. Manukyan. Solution Combustion Synthesis of Nanoscale Materials. *Chem. Rev.* 2016, 116, 14493–14586.
- [102] S.E. Pratsinis, “Flame aerosol synthesis of ceramics powders.” *Prog. Energy Combust. Sci.* 24 (1998) 197.
- [103] G.D. Ulrich, “Flame synthesis of fine particles.” *Chem. Eng. News* 62 (1984) 22.
- [104] K.B.K. Teo, C. Singh, M. Chhowalla, W.I. Milne. Catalytic synthesis of carbon nanotubes and nanofibers in: H.S. Nalwa (Ed.) *Encyclopedia of Nanoscience and Nanotechnology*, American Scientific Publishers, 2003 (p.1-22).
- [105] T. Zhang and L. Fu, Controllable Chemical Vapor Deposition Growth of Two-Dimensional Heterostructures, *Chem* 4 (2018) 671-689.
- [106] L.E. Depero, M. Ferroni, V. Guidi, et al., Preparation and micro-structural characterization of nanosized thin film of T02-WO<sub>3</sub> as a novel materials with high sensitivity towards NO<sub>2</sub>, *Sensors and Actuators B* 35-36 (1996) 381-383.
- [107] S.E. Pratsinis, “Flame aerosol synthesis of ceramics powders.” *Prog. Energy Combust. Sci.* 24 (1998) 197.
- [108] G.D. Ulrich, “Flame synthesis of fine particles.” *Chem. Eng. News* 62 (1984) 22.
- [109] W. Merchan-Merchan, A.V. Saveliev, L. Kennedy, W. Cuello Jimenez, “Combustion synthesis of carbon nanotubes and related structures.” *Progress in Energy and Combustion Science* 36 (2010) 696.
- [110] H. K. Kammler, L. Mädler, and S. E. Pratsinis. Flame Synthesis of Nanoparticles. *Chem. Eng. Technol.*, 24(2001)6.

- 
- [111] H. Richter, M. Treska, J.B. Howard, J.Z. Wen, S.B. Thomasson, A.A. Reading, P.M. Jardim, J.B. Vander Sande. Large Scale Combustion Synthesis of Single-walled Carbon Nanotubes. *J Nanosci Nanotechnol*, 8(2008)6065-74.
- [112] T. Tani, L. Mädler, S.E. Pratsinis. Homogeneous ZnO Nanoparticles by Flame Spray Pyrolysis. *J. Nanoparticle Research* 4 (2002) 337-343.
- [113] S.A. O'Neill, I.P. Parkin, R.J.H. Clark, A. Mills, N. Elliott, Atmospheric Pressure Chemical Vapour Deposition of thin Films of Nb<sub>2</sub>O<sub>5</sub> on Glass. *J. Mater. Chem.*, 13 (2003) 2952-2956.
- [114] A. Dabirian, Y. Kuzminykh, S. Harada, et al., in: IOP Conf. Series: Materials Science and Engineering, IOP Publishing, 2010, pp. 012026.
- [115] P-C. Chang, Z. Fan, D. Wang, et al., ZnO Nanowires Synthesized by Vapor Trapping CVD Method. *Chem. Mater.*, 16 (2004) 5133-5137.
- [116] H. Saitoh, M. Satoh, N. Tanaka, Y. Ueda, S. Ohshio, Homogeneous Growth of Zinc Oxide Whiskers. *Jpn. J. Appl. Phys.*, 38 (1999) 6973-6877.
- [117] R. Yang, J. Zheng, W. Li, et al., Low-Temperature Growth of ZnO Nanostructures by Oxygen Plasma Oxidation of ZnCl<sub>2</sub>. *Mater. Chem. Phys.*, 129 (2011) 693-695.
- [118] K.A. Gesheva, T. Ivanova, A Low-temperature Atmospheric Pressure CVD Process for Growing thin Films of MoO<sub>3</sub> and MoO<sub>3</sub>-WO<sub>3</sub> for Electrochromic Device Applications. *Chem. Vap. Deposition*, 12(2006)231-238.
- [119] Y.B. Li, Y. Bando, D. Golberg, K. Karashima, WO<sub>3</sub> nanorods/nanobelts synthesized via physicalvapor deposition process. *Chem. Phys. Lett.*, 367 (2003) 214-218.
- [120] J. Zhou, N.S. Xu, S.Z. Deng, et al., Synthesis of large-scaled MoO<sub>2</sub> nanowire arrays. *Chem. Phys. Lett.*, 382 (2003) 443-446.
- [121] C.O. Avellaneda, A. Pawlicka, M.A. Aegerter, Two Methods of Obtaining Sol-Gel Nb<sub>2</sub>O<sub>5</sub> thin Films for Electrochromic Devices. *J. Mater. Sci.*, 33 (1998) 2181-2185.
- [122] A. Pawlicka, M. Atik, M.A. Aegerter, Synthesis of Nb<sub>2</sub>O<sub>5</sub> thin Films for Electrochromic Devices. *J. Mater. Sci. Lett.*, 15 (1995) 1568-1570.
- [123] L. Znaidi, G.J.A.A.S. Illia, S. Benyahia, et al., Oriented ZnO thin films Synthesis by Sol-Gel Process for Laser Application. *Thin Solid Films*, 428 (2003) 257-262.
- [124] K. Galatsis, Y.X. Li, W. Wlodarski, et al., Comparison of Single and Binary Oxide MoO<sub>3</sub>, TiO<sub>2</sub> and WO<sub>3</sub> Sol-Gel Gas Sensors. *Sensor. Actuat. B*, 83 (2002) 276-280.
- [125] B.C. Satishkumar, A. Govindaraj, M. Nath and C. N. Rao, Synthesis of Metal Oxide Nanorods using Carbon Nanotubes as Templates. *J. Mater. Chem.*, 10(2000)2115-2119.
- [126] J. Jin, K. Hashimoto, S.J. Ohkoshi. Formation of Spherical and Rod-shaped  $\epsilon$ -Fe<sub>2</sub>O<sub>3</sub> Nanocrystals with a Large Coercive Field. *J. Mater. Chem.*, 15 (2005) 1067-1071.
- [127] S. Ohkoshi, S. Sakurai, J. Jin, K. Hashimoto. The Addition Effects of Alkaline Earth Ions in the Chemical Synthesis of  $\epsilon$ -Fe<sub>2</sub>O<sub>3</sub> Nanocrystals that Exhibit a huge Coercive Field. *J. Appl. Phys.*, 97 (2005) 10K312/1-10K312/3.
- [128] M. Gich, C. Frontera, A. Roig, et al., Magnetoelectric coupling in  $\epsilon$ -Fe<sub>2</sub>O<sub>3</sub> Nanoparticles. *Nanotechnology*, 17 (2006) 687-691.

- 
- [129] K. Kelm, W.Z. Mädler. Synthesis and Structural Analysis of  $\epsilon$ -Fe<sub>2</sub>O<sub>3</sub>. *Anorg. Allg. Chem.*, 631 (2005) 2383-2389.
- [130] M. Niederber, F. Krumeich, H. Muhr, et al., Synthesis and Characterization of Novel Nanoscopic Molybdenum Oxide Fibers. *J. Mater. Chem.* 11 (2001) 1941-1945.
- [131] M. Mozetič, U. Cvelbar, M.K. Sunkara, S. Vaddiraju. A method for the Rapid Synthesis of Large Quantities of Metal Oxide Nanowires at Low Temperatures. *Adv. Mater.*, 17 (2005) 2138-2142.
- [132] U. Cvelbar, M. Mozetič. Behaviour of Oxygen Atoms Near the Surface of Nanostructured Nb<sub>2</sub>O<sub>5</sub>. *J. Phys. D: Appl. Phys.*, 40 (2007) 2300-2303.
- [133] I. Sieber, H. Hildebrand, A. Friedrich, P. Schmuki, Formation of Self-Organized Niobium Porous Oxide on Niobium. *Electrochem. Commun.*, 7 (2005) 97-100.
- [134] S. Yang, H. Habazaki, T. Fujii, et al., Control of Morphology and Surface Wettability of Anodic Niobium Oxide Microcones Formed in Hot Phosphate–Glycerol Electrolytes. *Electrochim. Acta.*, 56 (2011) 7446-7453.
- [135] A. Vomiero, G.D. Mea, M. Ferroni, et al., Preparation and Microstructural Characterization of Nanosized Mo-TiO<sub>2</sub> and Mo-W-O thin Films by Sputtering: Tailoring of Composition and Porosity by Thermal Treatment. *Mater. Sci. Eng. B*, 101 (2003) 216-221.
- [136] T.M. McEvoy, K.J. Stevenson. Electrochemical Preparation of Molybdenum Trioxide thin films: Effect of Sintering on Electrochromic and Electroinsertion Properties. *Langmuir*. 19 (2003) 4316-4326.
- [137] W.B. Hu, Y.Q. Zhu, W.K. Hsu, B.H. Chang, M. Terrones, N. Grobert, H. Terrones, J.P. Hare, H.W. Kroto, D.R.M. Walton. Generation of Hollow Crystalline Tungsten Oxide fibres. *Appl. Phys. A*, 70 (2000) 231-233.
- [138] J.R. Morber, Y. Ding, M.S Haluska, et al., PLD-Assisted VLS Growth of Aligned Ferrite Nanorods, Nanowires, and Nanobelts-Synthesis, and Properties. *J. Phys. Chem. B.*, 110 (2006) 21672-21679.
- [139] L. Mädler, H.K. Kammler; R. Mueller, S.E. Pratsinis. Controlled Synthesis of Nanostructured Particles by Flame Spray Pyrolysis. *J. Aerosol Sci.* 33 (2002) 369-389.
- [140] T. Tani, L. Mädler, S.E. Pratsinis. Homogeneous ZnO Nanoparticles by Flame Spray Pyrolysis. *J. Nanoparticle Research* 4 (2002) 337-343.
- [141] M. Abdelbaki, Chapter 10 - Coflow and counterflow burners, Editor(s): Seyed Ehsan Hosseini, *Fundamentals of Low Emission Flameless Combustion and its Applications*, Academic Press, 2022, Pages 311-359,
- [142] P.H. Irace, A. Gopan, R.L. Axelbaum, An investigation of thermal radiation from laminar diffusion flames in a tri-coflow burner with central oxygen, *Combustion and Flame* 242 (2022) 112158-1 – 11.
- [143] M. Shehata, I.A. Ibrahim, H.M. Gad, Combustion Characteristics of Natural Gas/Air Flat Premixed Laminar Flames in a Developed Matrix Burner, *Scientific African* 20 (2023) e01659 1-8.

- 
- [144] H.K. Kammler, L. Mädler, and S.E. Pratsinis. Flame Synthesis of Nanoparticles. *Chemical Engineering Technology* 24 (2001): 583. *Powder Technology*, 135–136(2003) 310-320.
- [145] J.R. Jensen, T. Johannessen, S. Wedel, and H. Livbjerg. Preparation of ZnO–Al<sub>2</sub>O<sub>3</sub> Particles in a Premixed Flame. *J. Nanopart. Res.*, 2(2000) 363-373.
- [146] W.J. Stark, K. Wegner, S.E. Pratsinis, and A. Baiker. Flame Aerosol Synthesis of Vanadia-titania Nanoparticles: Structural and Catalytic Properties in the Selective Catalytic Reduction of NO by NH<sub>3</sub>. *J. Catalysis*, 197(2000)182-191.
- [147] T. Tani, L. Madler, and S.E. Pratsinis. Homogeneous ZnO Nanoparticles by Flame Spray Pyrolysis. *J. Nanopart. Res.*, 4(2002)337-343.
- [148] X. Qin, Y. Ju, S. Bernhard, and N. Yao. Europium-doped Yttrium Silicate Nanophosphors Prepared by Flame Synthesis. *Materials Research Bulletin*, 42(2006)1440-1449.
- [149] P.S. Fennell, J.S. Dennis, and A.N. Hayhurst. The Sampling of Nanoparticles of MgO Formed when Doping an Oxygen-rich Flame with Magnesium: The Measurement of the Concentrations and Size-distributions of these Nanoparticles. *Combustion and Flame*, 151(2007)560-572.
- [150] N. K. Memon, D. H. Anjum, S. H. Chung. Multiple-Diffusion Flame Synthesis of Pure Anatase and Carbon-Coated Titanium Dioxide Nanoparticles. *Combustion and Flame*, 160(2013)1848–1856.
- [151] M.J. Height, L. Mädler, and S. E. Pratsinis. Nanorods of ZnO Made by Flame Spray. Pyrolysis. *Chem. Mater.*, 18(2006)572-578.
- [152] J.J. Thomson, G.P. Thomson. *Conduction of electricity through gases*, vol. 1. Cambridge University Press; 1928. p. 399.
- [153] E. R. Place and F. J. Weinberg. Electrical Control of Flame Carbon. *Proc. Roy. Soc. Lond.* A289, 157(1965).
- [154] J. Lawton, F.J. Weinberg. *Electrical Aspects of Combustion*. Clarendon Press; 1969.
- [155] M. Kono, K. Iinuma and S. Kumagai. Eighteenth Symposium (International) on Combustion. The Combustion Institute, (1981) p. 1167.
- [156] S.K. Dayal and T.P. Pandya. Structure of Counterflow Diffusion Flame in Transverse Electric Fields. *Combustion and Flame*, 35(1979)277-287.
- [157] S. Li, Y. Ren, P. Biswas, S.D. Tse. Flame Aerosol Synthesis of Nanostructured Materials and Functional Devices: Processing, Modeling, and Diagnostics. *Progress in Energy and Combustion Science*, 55(2016)1–59.
- [158] J. L. Katz and C-H Hung. Initial Studies of Electric Field Effects on Ceramic Powder Formation in Flames. Twenty-Third Symposium (International) on Combustion. The Combustion Institute, 1990/pp. 1733-1738.
- [159] H.K. Kammler, R. Jossen, P.W. Jr. Morrison, S.E. Pratsinis, G. Beaucage. The Effect of External Electric Fields during Flame Synthesis of Titania. *Powder Technology*, 135–136(2003)310–320.
- [160] S. Vemury, S.E. Pratsinis. Charging and Coagulation during Flame Synthesis of Silica. *J. Aerosol Sci.*, 27(1996)951–966.



- 
- [161] S. Vemury, S.E. Pratsinis, L. Kibbey. Electrically Controlled Flame Synthesis of Nanophase TiO<sub>2</sub>, SiO<sub>2</sub>, and SnO<sub>2</sub> Powders. *J. Mater. Res.*, 12(1997)1031–1042.
- [162] D.R. Hardesty, F.J. Weinberg. Electrical Control of Particulate Pollutants from Flames. Thirteenth Symposium (International on Combustion). The Combustion Institute, Pittsburgh, 1973, pp. 907–918.
- [163] S. Vemury, S.E. Pratsinis. Corona-assisted Flame Synthesis of Ultrafine Titania Particles. *Appl. Phys. Lett.*, 66(1995)3275–3277.
- [164] H. Zhao, X. Liu, and S.D. Tse. Control of Nanoparticle Size and Agglomeration through Electric-field-enhanced Flame Synthesis. *J. Nanopart. Res.*, 10(2008)907–923.
- [165] R. Strobel, L. Mädler, M. Piacentini, M. Maciejewski, A. Baiker, and S. E. Pratsinis. Two-Nozzle Flame Synthesis of Pt/Ba/Al<sub>2</sub>O<sub>3</sub> for NO<sub>x</sub> Storage. *Chem. Mater.*, 18(2006)2532–2537.
- [166] C-Y Chiang, K. Aroh, S. H. Ehrman. Copper Oxide Nanoparticle made by Flame Spray Pyrolysis for Photoelectrochemical Water Splitting e Part I. CuO Nanoparticle Preparation. *International Journal of Hydrogen Energy*, 37(2012)4871–4879.
- [167] S-H Ng, T. J. Patey, R. Büchel, F. Krumeich, J-Z Wang, H-K Liu, S. E. Pratsinis and P. Novák. Flame Spray-Pyrolyzed Vanadium Oxide Nanoparticles for Lithium Battery Cathodes. *Phys. Chem. Chem. Phys.*, 11(2009)3748–3755.
- [168] S.E. Pratsinis, W. Zhu, S. Vemury. The Role of Gas Mixing in Flame Synthesis of Titania Powders. *Powder Technology*, 86(1996)87–93
- [169] B.M. Kumfer, K. Shinoda, B. Jeyadevan, I.M. Kennedy. Gas-Phase Flame Synthesis and Properties of Magnetic Iron Oxide Nanoparticles with Reduced Oxidation State. *Journal of Aerosol Science*, 41(2010)257–265.
- [170] J. Wang, S. Li, W. Yan, S. D. Tse, Q. Yao. Synthesis of TiO<sub>2</sub> Nanoparticles by Premixed Stagnation Swirl Flames. *Proceedings of the Combustion Institute*, 33(2011)1925–1932.
- [171] F. Xu, S.D. Tse, J.F. Al-Sharab, and B.H. Kear, Flame synthesis of aligned tungsten oxide nanowires, *Appl. Phys. Lett.* 88 (2006) 243115-3.
- [172] S. Tse, B. Kear, F. Cosandey. Flame Synthesis of Metal Oxide Nanostructures. *J Mater Chem.*, 15(2005)1–3.
- [173] P. M. Rao and X. Zheng. Rapid Catalyst-Free Flame Synthesis of Dense, Aligned  $\alpha$ -Fe<sub>2</sub>O<sub>3</sub> Nanoflake and CuO Nanoneedle Arrays. *Nanoletters*, 9 (8) (2009) 3001–3006.
- [174] W. Merchan-Merchan, A. V. Saveliev, L.A. Kennedy. Flame Synthesis of Molybdenum Oxide Whiskers. *Chem. Phys. Lett.*, 422(2006)72–77.
- [175] W. Merchan-Merchan, A.V. Saveliev, V. Nguyen. Opposed Flow Oxy-Flame Synthesis of Carbon and Oxide Nanostructures on Molybdenum Probes. *Proc. Combust. Inst.*, 32(2009)1879–1886.
- [176] W. Merchan-Merchan, A.V. Saveliev, A.M. Taylor. High Rate Flame Synthesis of Highly Crystalline Iron Oxide Nanorods. *Nanotechnology* 19 (2008) 125605–125610.

- 
- [177] M. Suemitsu, T. Abe, H-J. Na, H. Yamane. MoO<sub>2</sub> Hollow Fiber with Rectangular Cross Sections. *Jpn. J. Appl. Phys.*, 44(2005)L449-L450.
- [178] H. K. Kammler, L. Mädler, S.E. Pratsinis. Flame Synthesis of Nanoparticles. *Chemical Engineering Technology*, 24(6)(2001)583-596.
- [179] G.W. Lee, J. Jurng and J. Hwang. Formation of Ni-catalyzed Multiwalled Carbon Nanotubes and Nanofibers on a Substrate using an Ethylene Inverse Diffusion Flame. *Combustion and Flame*, 139 (2004) 167-175.
- [180] F. Xu, X. Liu, S. D. Tse, F. Cosandey, B. H. Kear. Flame Synthesis of Zinc Oxide Nanowires. *Chemical Physics Letters*, 449 (2007) 175–181.
- [181] W. Merchan-Merchan, A.V. Saveliev, V. Nguyen. Opposed Flow Oxy-flame Synthesis of Carbon and Oxide Nanostructures on Molybdenum Probes. *Proc. Combust. Inst.*, 32(2009)1879-1886.
- [182] W. Merchan-Merchan, A.V. Saveliev, A.M. Taylor. High Rate Flame Synthesis of Highly Crystalline Iron Oxide Nanorods. *Nanotechnology*, 19 (2008) 125605-125610.
- [183] W. Merchan-Merchan, A.V. Saveliev, W. Cuello Jimenez, G. Salkar. Flame Synthesis of Hybrid Nanowires with Carbon Shells and Tungsten-oxide Cores. *Carbon*, 48(2010) 4510-4518.
- [184] P.M. Rao and X. Zheng. Flame Synthesis of Tungsten Oxide Nanostructures on Diverse Substrates. *Proceedings of the Combustion Institute*, 33 (2010)1891-1898.
- [185] W. Merchan-Merchan, A. V. Saveliev, and W. Cuello Jimenez. Solid Support Flame Synthesis of 1D and 3D Tungsten-oxide Nanostructures. *Proceedings of the Combustion Institute*, 33(2010)1899-1908.
- [186] P.M. Rao, S.C. In, and X. Zheng. Flame Synthesis of WO<sub>3</sub> Nanotubes and Nanowires for Efficient Photoelectrochemical Water-Splitting. *Proceedings of the Combustion Institute*, 34 (2012)2187-2195.
- [187] P.M. Rao, and X. Zheng. Morphology-Controlled Flame Synthesis of Single, Branched, and Flower-like  $\alpha$ -MoO<sub>3</sub> Nanobelt Arrays. *Nano Letters* 11 (2011): 872-877.
- [188] W. Merchan-Merchan, A.V. Saveliev, and A.M. Taylor. Nucleation and Growth Mechanism for Flame Synthesis of MoO<sub>2</sub> Hollow Microchannels with Nanometer Wall Thickness. *Micron* 40 (8) (2009): 821-826.
- [189] W. Merchan-Merchan and M. Farmahini Farahani. Rapid Catalyst-free Flame Synthesis of  $\alpha$ -Nb<sub>2</sub>O<sub>5</sub> Micro/nanorods. *Materials Chemistry and Physics*, 140(2013)516-521.
- [190] P. Kathirvel, J. Chandrasekaran, D. Manoharan, S. Kumar. Formation and Characterization of Flame Synthesized Hexagonal Zinc Oxide Nanorods for Gas Sensor Applications. *Ceramics International*, 39(2013) 5321-5325.
- [191] F. Xu. Investigating Flame-Based Synthesis of Carbon Nanotubes and Metal-Oxide Nanowires. PhD Thesis. New Brunswick, New Jersey. October 2007.
- [192] Z. Dong, J.F. Al-Sharab, B. H. Kear, and S. D. Tse. Combined Flame and Electrodeposition Synthesis of Energetic Coaxial Tungsten-Oxide/Aluminum Nanowire Arrays. *Nano Lett.*, 13 (2013) 4346–4350.

- 
- [193] S.E. Pratsinis. Structural and Fluorescence Properties of Ni. *Prog. Energy Combust. Sci.*, 24(1998)197-219.
- [194] G. D. Ulrich. Flame Synthesis of Fine Particles. *Chem. Eng. News*, 62(1984) 22-29.
- [195] W. Merchan-Merchan, A.V. Saveliev, M. Desai. Volumetric flame synthesis of well-defined molybdenum oxide nanocrystals. *Nanotechnology*, 20(2009)475601.
- [196] O. Merdrignac-Conanec, P.T. Moseley. Gas Sensing Properties of the Mixed Molybdenum Tungsten Oxide,  $W_{0.9}Mo_{0.1}O_3$ , *J. Mater. Chem.*, 12 (2002) 1779-1781.
- [197] S.H. Baeck, T.F. Jaramillo, D.H. Jeong, E.W. McFarland, Parallel Synthesis and Characterization of Photoelectrochemically and Electrochromically Active Tungsten-Molybdenum Oxides, *Chem. Commun.*, 4(2004) 390-391.
- [198] K. Gesheva, A. Szekeres, T. Ivanova, Optical Properties of Chemical Vapor Deposited Thin Films of Molybdenum and Tungsten Based Metal Oxides, *Sol. Energy Mater. Sol. Cells*, 76 (2003) 563-576.
- [199] L. Kondrachova, B.P. Hahn, G. Vijayaraghavan, R.D. Williams, K.J. Stevenson. Cathodic Electrodeposition of Mixed Molybdenum Tungsten Oxides from Peroxopolymolybdotungstate Solutions. *Langmuir*, 22 (2006) 10490-10498.
- [200] S. Li, M.S. El-Shall, Synthesis and Characterization of Photochromic Molybdenum and Tungsten Oxide Nanoparticles, *Nanostruct. Mater.*, 12 (1999) 215–219.
- [201] L. Zheng, Y. Xu, D. Jin, Y. Xie, Novel Metastable Hexagonal  $MoO_3$  Nanobelts: Synthesis, Photochromic, and Electrochromic Properties. *Chem. Mater.*, 21 (2009) 5681-5690.
- [202] J. Jiang, Y. Li, J. Liu, et al., Recent Advances in Metal Oxide-based Electrode Architecture Design for Electrochemical Energy Storage *Adv. Mater.* 2012, 24, 5166–5180.
- [203] K.A. Gesheva, A. Cziraki, T. Ivanova, A. Szekeres. Crystallization of Chemically Vapor Deposited Molybdenum and Mixed Tungsten/Molybdenum Oxide Films for Electrochromic Application. *Thin Solid Films*, 515(2007) 4609-4613.
- [204] T. Ivanova, K. A. Gesheva, M. Ganchev, E. Tzvetkova. Electrochromic Behavior of CVD Molybdenum Oxide and Mo-W Mixed-Oxide Thin Films, *J. Mater. Sci. Mater. Electron.*, 14(2003)755-758.
- [205] X.L. Sun, A.H. Chen, H.Z. Zhang, H.T. Cao. Optical and Electrochromic Properties of Sol-Gel Deposited Mixed  $MoO_3$ - $WO_3$  Thin Films. *Adv. Mat Res.*, 79-82 (2009) 843-846.
- [206] C.E. Tracy, D.K. Benson. Preparation of Amorphous Electrochromic Tungsten Oxide and Molybdenum Oxide by Plasma Enhanced Chemical Vapour Deposition. *J. Vac. Sci. Technol. A*, 4(1986)2377-2383.
- [207] U. Cvelbar, Z. Chen, I. Levchenko, R.M. Sheetz, J.B. Jasinski, M. Menon, M.K. Sunkara, K.K. Ostrikov. Sub-oxide-to-metallic, Uniformly-nanoporous Crystalline Nanowires by Plasma Oxidation and Electron Reduction. *Chem. Commun.*, 48(2012)11070-11072.
- [208] Y. Feng, I.S. Cho, L. Cai, P.M. Rao, X. Zheng. Sol-flame Synthesis of Hybrid Metal Oxide Nanowires. *Proc. Combust. Inst.*, 34(2013)2179-2186.

- 
- [209] L. Mädler, W.J. Stark, S.E. Pratsinis. Flame-made Ceria Nanoparticles. *J. Mater. Res.*, 17(2002)1356.
- [210] L. Cai, P.M. Rao, Y. Feng, X. Zheng. Flame Synthesis of 1D Complex Metal Oxide Nanomaterials. *Proc. Combust. Inst.*, 34 (2013) 2229-2236.
- [211] M. Farmahini- Farmahini, A. V. Saveliev, W. Merchan-Merchan. Volumetric Flame Synthesis of Mixed Tungsten–Molybdenum Oxide Nanostructures. *Proceedings of the Combustion Institute*, 36(2017)1055–1063.
- [212] M. Farmahini- Farmahini, Investigating the Synthesis of Transition Metal Oxide Nanostructures in a Counter-Flow Flame, PhD Dissertation (2014).
- [213] W.J. Stark, M. Maciejewski, L. Mädler, S. E. Pratsinis, and A. Baiker. Flame-made Nanocrystalline Ceria/Zirconia: Structural Properties and Dynamic Oxygen Exchange Capacity. *Journal of Catalysis*, 220 (2003)35–43.
- [214] M.A. Ismail, N. K. Memon, M. N. Hedhili, D. H. A. Suk Ho Chung. Synthesis of TiO<sub>2</sub> Nanoparticles Containing Fe, Si, and V using Multiple Diffusion Flames and Catalytic Oxidation Capability of Carbon-Coated Nanoparticles. *J. Nanopart Res.*, 18(2016)22.
- [215] X. Zhang, H. Zheng, V. Battaglia, R. L. Axelbaum. Flame Synthesis of 5 V Spinel-LiNi<sub>0.5</sub>Mn<sub>1.5</sub>O<sub>4</sub> Cathode-Materials for Lithium-ion Rechargeable-Batteries. *Proceedings of the Combustion Institute*, 33(2011)1867–1874.
- [216] M. Farmahini- Farmahini, A. V. Saveliev, W. Merchan-Merchan. Volumetric Flame Synthesis of Mixed Tungsten–Molybdenum Oxide Nanostructures. *Proceedings of the Combustion Institute*, 36(2017)1055–1063.
- [217] M. Farmahini- Farmahini, Investigating the Synthesis of Transition Metal Oxide Nanostructures in a Counter-Flow Flame. PhD Dissertation, University of Oklahoma, Norman, OK (2014).
- [218] S.E. Pratsinis. Flame aerosol synthesis of ceramic powders, *Prog. Energy Combust. Sci.* 24 (1998)197-219
- [219] T. Tani, L. Madler, S.E. Pratsinis, Homogeneous ZnO nanoparticles by flame spray pyrolysis, *J. Nanoparticle Research* 4 (2002) 337-343
- [220] S. Li, Y. Ren, P. Biswas, S.D. Tse, Flame aerosol synthesis of nanostructured materials and functional devices: Processing, modeling, and diagnostics, *Prog. Energy and Combust. Sci.* 55 (2016) 1–59.
- [221] W. Merchan-Merchan, W. Cuello Jimenez, O. Rodriguez Coria, et al., Nanomaterial synthesis, design, fabrication and applications, in: Y. Beeran Pottathara, S. Thomas, N. Kalarikkal, et al. (Eds), *Flame synthesis of nanostructured transition metal oxides: trends, developments, and recent advances*, Elsevier 1<sup>st</sup> Edition, 2019, pp. 201-263.
- [222] W. Merchan-Merchan, A.V. Saveliev, W. Cuello Jimenez, G. Salkar, Flame synthesis of hybrid nanowires with carbon shells and tungsten-oxide cores, *Carbon* 48 (2010) 4510-4518.
- [223] Y. Feng, I.S. Cho, L. Cai, et al., Sol-flame synthesis of hybrid metal oxide nanowires, *Proceed. Combust. Institute* 34 (2013) 2179-2186.

- 
- [224] Z. Dong, D. Huo, B. H. Kear, S. D. Tse, Combined flame and solution synthesis of nanoscale tungsten-oxide and zinc/tin-oxide heterostructures, *Nanoscale* 7 (2015) 20510-20520.
- [225] C.J. Sung, J.B. Liu, C.K. Law, Structural response of counterflow diffusion flames to strain rate variations. *Comb. Flame* 100 (1995) 367.
- [226] C.J. Sung, C.K. Law Dominant chemistry and Physical factors affecting NO formation and control in oxy-fuel burning. 27th symposium (Int.) on Comb. (1998) 1411.
- [227] A. Beltrame, P. Porshnev, W. Merchan-Merchan et al. Soot and NO formation in methane-oxygen enriched diffusion flames. *Combust. Flame* 124 (2001) 295.
- [228] M. Silvestrini, W. Merchan-Merchan, H. Richter, et al. Fullerene formation in atmospheric pressure opposed flow oxy-flames. *Proc. Combust. Inst.* 30 (2005) 2545.
- [229] W. Merchan-Merchan, A. V. Saveliev, W.C. Jimenez, G. Salkar. "Flame Synthesis of Hybrid Nanowires with Carbon Shells and Tungsten-Oxide Cores" *Carbon*, 48:4510-4518 (2010).
- [230] W. Merchan-Merchan, A.V. Saveliev, L. Kennedy, W. Cuello Jimenez, et al. Flame synthesis of hybrid nanowires with carbon shells and tungsten-oxide cores. *Carbon* 48 (2010) 4510.
- [231] A. Taylor. Flame synthesis of transition metal oxides. Master Thesis, University of Oklahoma, Normal, OK (2008).
- [232] M. Placzek, M. Kosela, Microscopic methods in analysis of submicron phospholipid dispersions, *Acta Pharm.* 66(2016) 1-22.
- [233] P.A. Skovorodko, O.P. Korobeinichev, A.G. Tereshchenko, D.A. Knyazkov, et al. Experimental and numerical study of thermocouple-induced perturbation of the flame structure. *Proceedings of 4th European Combustion Meeting (ECM 2009)*, 14 - 17 April 2009, Vienna University of Technology, Vienna, Austria.
- [234] J. Zhou, L. Gong, S.Z. Deng, et al. Growth and field-emission property of tungsten oxide nanotip arrays." *Appl. Phys. Lett.* 87 (2005) 223108.
- [235] Y.Z. Jin, Y.Q. Zhu, R.L.D. Whitby, et al. Simple approaches to quality large-scale tungsten oxide nanoneedles. *J. Phys. Chem. B* 108 (2004) 15572.
- [236] Y.B. Li, Y. Bando, D. Golberg, et al. WO<sub>3</sub> nanorods/nanobelts synthesized via physical vapor deposition process. *Chem. Phys. Lett.* 367 (2003) 214.
- [237] W.B. Hu, Y.Q. Zhu, W.K. Hsu, et al. Generation of hollow crystalline tungsten oxide fibres. *Appl. Phys. A* 70 (2000) 231.
- [238] Y. Wu, Z. Xi, G. Zhang, et al. Growth hexagonal tungsten trioxide tubes. *J. Crys. Growth* 292 (2006) 143.
- [239] L.F. Cheng, X.T. Zhang, Y.H. Chen, et al. Template synthesis and characterization of WO<sub>3</sub>/TiO<sub>2</sub> composite nanotubes. *Nanotechnology* 16 (2005) 1341-1345.
- [240] G. Kickelbick, *Hybrid materials synthesis, characterization, and applications.* Wiley VCH (2007).
- [241] F. Xu, S.D. Tse, J.F. Al-Sharab, et al. Flame synthesis of aligned tungsten oxide nanowires. *Appl. Phys. Lett.* 88 (2006) 243115.

- 
- [242] L. Jankovic, D. Gournis, P.N. Trikalitis, et al. Carbon nanotubes encapsulating superconducting single-crystalline tin nanowires. *Nano. Lett.* 6 (2006) 1131.
- [243] C. Arnould, T.U. Korányi, J. Delhalle, et al. Fabrication of tantalum oxide/carbon nanotubes thin film composite on titanium substrate. *J. Colloid. Int. Sci.* 344 (2010) 390.
- [244] W. Merchan-Merchan, A.V. Saveliev, L.A. Kennedy. Flame synthesis of molybdenum oxide whiskers. *Chem. Phys. Lett.* 422 (2006) 72.
- [245] W. Merchan-Merchan, A.V. Saveliev, A. Taylor. Nucleation and growth mechanism for flame synthesis of MoO<sub>2</sub> hollow microchannels with nanometer wall thickness. *Micron* 40 (2009) 821.
- [246] F. Xu, S.D. Tse, J.F. Al-Sharab, et al. Flame synthesis of aligned tungsten oxide nanowires. *Appl. Phys. Lett.* 88 (2006) 243115.
- [247] P.M. Rao, X. Zheng. Rapid catalyst-free flame synthesis of dense, aligned  $\alpha$ -Fe<sub>2</sub>O<sub>3</sub> nanoflakes and CuO nanoneedle arrays. *Nanoletters* 9 (2009) 3001.
- [248] J.S. Jeong, J.Y. Lee, J.H. Cho et al. Single-crystalline ZnO microtubes formed by coalescence of ZnO nanowires using a simple metal-vapor deposition method. *Chem. Mater.* 17 (2005) 2752.
- [249] W. Merchan-Merchan, A.V. Saveliev, L.A. Kennedy. Flame synthesis of molybdenum oxide whiskers. *Chem. Phys. Lett.* 422 (2006) 72.
- [250] I. Sunagawa, *Crystals. Growth, Morphology and Perfection*, Cambridge University Press, Cambridge, 2005, p. 74.
- [251] Y. Wu, Z. Xi, G. Zhang et al. Growth hexagonal tungsten trioxide tubes. *J. Cryst. Growth* 292 (2006) 143.
- [252] M.W. Chase, NIST-JANAF Thermochemical tables. *J Phys Chem Ref Data* 4th Ed. (1998) Monograph 9:1-1951.
- [253] S.E. Pratsinis. Flame aerosol synthesis of ceramic powder. *Prog. Energy Combust. Sci.* 24 (1998) 197.
- [254] G.D. Ulrich. Flame synthesis of fine particles. *Chem. Eng. News* 62 (1984) 22.
- [255] P. Roth, Particle synthesis in flames. *Proceedings of the Combustion Institute* 31 (2007) 1773.
- [256] W. Merchan-Merchan, A.V. Saveliev, L.A. Kennedy. Carbon nanostructures in opposed-flow oxy-flames. *Combust. Sci. and Tech.* 175 (2003) 2217.
- [257] W. Merchan-Merchan, A.V. Saveliev, W. Cuello-Jimenez. Novel flame-gradient method for synthesis of metal-oxides channels, nanowires and nanorods. *J. Experimental Nanoscience* 5 (2010) 199.
- [258] W. Merchan-Merchan, A.V. Saveliev, A.M. Taylor. High-rate flame synthesis of highly crystalline iron oxide nanorods. *Nanotechnology* 19 (2008) 125605.
- [259] E. Comini, C. Baratto, G. Faglia, M. Ferroni, A. Vomiero, G. Sberveglieri, Quasi-one dimensional metal oxide semiconductors: Preparation, characterization and application as chemical sensors, *Prog. Mater. Sci.*, 54 (2009) 1-67.
- [260] N. Baig, I. Kammakakam, W. Falathabe. Nanomaterials: a review of synthesis methods, properties, recent progress, and challenges, *Mater. Adv.* 2 (2021) 1821–1871.

- 
- [261] C-J Jia, L-D Sun, Z-G Yan, et al. Single-Crystalline Iron Oxide Nanotubes. *Angew Chem. Int. Ed.* 44 (2005) 4328-4333.
- [262] L. Vayssieres, N. Beermann, S. E. Lindquist and A. Hagfeldt. Controlled Aqueous Chemical Growth of Oriented Three-Dimensional Crystalline Nanorod Arrays: Application to Iron(III) Oxides. *Chem. Mater.* 13 (2001) 233-235.
- [263] S. Chen, J. Feng, X. Guo, J. Hong and W. Ding. One-step wet chemistry for preparation of magnetite nanorods. *Mater. Lett.* 59 (2005) 985-988.
- [264] T.A. Crowley, K.J. Ziegler, D.M. Lyons, et al. Synthesis of Metal and Metal Oxide Nanowire and Nanotube Arrays within a Mesoporous Silica Template. *Chem. Mater.* 15 (2003) 3518-3522.
- [265] D.S. Xue, C.X. Gao, Q.F. Liu and L.Y. Zhang. Preparation and characterization of haematite nanowire arrays. *J. Phys.: Condens. Matter.* 15 (2003) 1455-1459.
- [266] C. Terrier, M. Abid, C. Arm, et al. Fe<sub>3</sub>O<sub>4</sub> nanowires synthesized by electroprecipitation in templates. *J. Appl. Phys.* 98 (2005) 086102-1 - 086102-3.
- [267] Z. Liu, D. Zhang, S. Han, C. Li, B. Lei, W. Lu, J. Fang and C. Zhou, *J. Am. Chem. Soc.* 127 (2005) 6-7.
- [268] Y. Ding, J. R. Morber, R.L. Snyder and Z.L. Wang. Nanowire Structural Evolution from Fe<sub>3</sub>O<sub>4</sub> to  $\epsilon$ -Fe<sub>2</sub>O<sub>3</sub>. *Adv. Funct. Mater.* 17 (2007) 1172-1178.
- [269] J.R. Morber, Y. Ding, M.S. Haluska, et al. PLD-Assisted VLS Growth of Aligned Ferrite Nanorods, Nanowires, and Nanobelts-Synthesis, and Properties. *J. Phys. Chem. B.* 110 (2006) 21672-21679.
- [270] J. Stringer. Oxidation of tantalum in oxygen-nitrogen and oxygen-inert gas mixtures. *Oxidation of Metals* 11 (1977) 225-239.
- [271] K. Ogata, K. Maejima, S.Z. Fujita, S.G. Fujita. Growth mode control of ZnO toward nanorod structures or high-quality layered structures by metal-organic vapor phase epitaxy. *J. Cryst. Growth* 248 (2003) 25-30.
- [272] S. Kudera, L. Carbone, E. Carlino, et al., Synthesis routes for the growth of complex nanostructures, In *Physica E: Low-dimensional Systems and Nanostructures* 37 (2007) 128-33.
- [273] L. Cai, P.M. Rao, Y. Feng, X. Zheng, Flame synthesis of 1-D complex metal oxide nanomaterials, In *Proceedings of the Combustion Institute* 34 (2013) 2229-36.
- [274] R. Amigo, J. Asenjo, E. Krotenko et al., Electrochemical synthesis of new magnetic mixed oxides of Sr and Fe: Composition, magnetic properties, and microstructure, *Chem. Mater.* 12 (2000), 573-9.
- [275] J.A. Rodriguez, J.C. Hanson, S. Chaturvedi, et al., Phase transformations and electronic properties in mixed metal oxides; experimental and theoretical studies on the behaviour of NiMoO<sub>4</sub> and MgMoO<sub>4</sub>, *J. Chem. Phys.* 112 (2000) 935-45.
- [276] D. Zappa, V. Galstyan, N. Kaur, et al. Metal oxide -based heterostructures for gas sensors- A review, *Analytica Chimica Acta* 1039 (2018) 1-23.
- [277] S.E. Pratsinis. Flame aerosol synthesis of ceramic powders, *Prog. Energy Combust. Sci.* 24 (1998)197-219
- [278] T. Tani, L. Madler, S.E. Pratsinis, Homogeneous ZnO nanoparticles by flame spray pyrolysis, *J. Nanoparticle Research* 4 (2002) 337-343

- 
- [279] L. Cai, P.M. Rao, Y. Feng, X. Zheng, Flame synthesis of 1-D complex metal oxide nanomaterials, *Proceed. Combust. Institute* 34 (2013) 2229-2236.
- [280] S. Li, Y. Ren, P. Biswas, S.D. Tse, Flame aerosol synthesis of nanostructured materials and functional devices: Processing, modeling, and diagnostics, *Prog. Energy and Combust. Sci.* 55 (2016) 1–59.
- [281] W. Merchan-Merchan, W. Cuello Jimenez, O. Rodriguez Coria, et al., Nanomaterial synthesis, design, fabrication and applications, in: Y. Beeran Pottathara, S. Thomas, N. Kalarikkal, et al. (Eds), *Flame synthesis of nanostructured transition metal oxides: trends, developments, and recent advances*, Elsevier 1st Edition, 2019, pp. 201-263.
- [282] W. Merchan-Merchan, A.V. Saveliev, W. Cuello Jimenez, G. Salkar, Flame synthesis of hybrid nanowires with carbon shells and tungsten-oxide cores, *Carbon* 48 (2010) 4510-4518.
- [283] R. Ferrando, J. Jellinek, and R.L. Johnston, Nanoalloys: From Theory to Applications of Alloy Clusters and Nanoparticles, *Chem. Reviews* 2008 108 (3), 845-910.
- [284] D. Shaposhnik, R. Pavelko, E. Llobet, F. Gispert-Guirado, X. Vilanova, Hydrogen sensors on the basis of SnO<sub>2</sub>-TiO<sub>2</sub> systems, *Procedia Eng* 25 (2011) 1133-1136.
- [285] R.B. Vasiliev, M.N. Romyantseva, S.E. Podguzova, A.S. Ryzhikov, L.I. Ryabova, A.M. Gaskov, Effect of interdiffusion on electrical and gas sensor properties of CuO/SnO<sub>2</sub> heterostructure, *Mater. Sci. Eng. B* 57 (1999) 241-246.
- [286] N. Kaur, D. Zappa, M. Ferroni, N. Poli, M. Campanini, R. Negrea, E. Comini, Branch-like NiO/ZnO heterostructures for VOC sensing, *Sensor. Actuator. B Chem.* 262 (2018).
- [287] S.V. Prabhakar Vattikuti, Heterostructure Nanomaterials: Latest Trends in Formation of Inorganic Heterostructures, in: S.M. Bhagyaraj, O.S. Oluwafemi, N. Kalarikkal, et al. (Eds), *Synthesis of Inorganic Nanomaterials*, Woodhead Publishing, 2018, pp. 89-120.
- [288] D. Zappa, V. Galstyan, N. Kaur, et al., Metal oxide-based heterostructures for gas sensors - A review, *Analytica Chimica Acta* 1039 (2018) 1-23.
- [289] D. Barreca, E. Comini, A.P. Ferrucci, et al., First example of ZnO-TiO<sub>2</sub> nanocomposites by chemical vapor Deposition: structure, morphology, composition, and gas sensing performances, *Chem. Mater.* 19 (2007) 5642-5649.
- [290] W.J. Moon, J.H. Yu, G.M. Choi, The CO and H<sub>2</sub> gas selectivity of CuO-doped SnO<sub>2</sub>-ZnO composite gas sensor, *Sens. Actuators B: Chem.* 87 (2002) 464-470.
- [291] R. Liu, Hybrid organic/inorganic nanocomposites for photovoltaic cells, *Materials* 7 (2014) 2747-71.
- [292] S. Li, M. Samy El-Shall, Synthesis and characterization of photochromic molybdenum and tungsten oxide nanoparticles, *Nanostructured Materials* 12 (1999) 215-9.
- [293] T. He, J. Yao, Photochromism in composite and hybrid materials based on transition-metal oxides and polyoxometalates, *Progress in Materials Science* 51 (2006) 810-79.



- 
- [294] J. Wang, Q. Zhang, X. Li, et al., Smart construction of three-dimensional hierarchical tubular transition metal oxide core/shell heterostructures with high-capacity and long-cycle-life lithium storage, *Nano Energy* 12 (2015) 437-446.
- [295] N. Datta, N.S. Ramgir, S. Kumar, et al., Role of various interfaces of CuO/ZnO random nanowire networks in H<sub>2</sub>S sensing: an impedance and Kelvin probe analysis, *Sens. Actuators B: Chem.* 202 (2014) 1270–1280.
- [296] P.M. Rao, L. Cai, C. Liu, et al. Simultaneously Efficient Light Absorption and Charge Separation in WO<sub>3</sub>/BiVO<sub>4</sub> Core/Shell Nanowire Photoanode for Photoelectrochemical Water Oxidation. *Nano Lett.* 14 (2014) 1099–105.
- [297] E.A. Gulbransen, High-temperature oxidation of tungsten, molybdenum and carbon, *Nature* 198 (1963) 82-830.
- [298] N. Zhao, W. Ma, Z. Cui, W. Song, et al., Polyhedral maghemite nanocrystals prepared by a flame synthetic method: preparations, characterizations, and catalytic properties. *ACS Nano* 3 (2009) 1775–1780.
- [299] C. Xiong, T. Zhang, W. Kong, et al., ZIF-67 derived porous Co<sub>3</sub>O<sub>4</sub> hollow nanopolyhedron functionalized solution-gated graphene transistors for simultaneous detection of glucose and uric acid in tears, *Biosensors and Bioelectronics* 101 (2018) 21–28.
- [300] C. Xia, X. Yanjun, W. Ning, Hollow Fe<sub>2</sub>O<sub>3</sub> polyhedrons: One-pot synthesis and their use as electrochemical material for nitrite sensing, *Electrochimica Acta* 59 (2012) 81– 85.
- [301] Y. Zhang, Y. Diao, H. Lee, et al., Intrinsic and extrinsic parameters for controlling the growth of organic single-crystalline nanopillars in photovoltaics. *Nano Letters* 14 (2014) 5547-5554.
- [302] D. Zappa, V. Galstyan, N. Kaur, et al., “Metal oxide -based heterostructures for gas sensors”- A review, *Analytica Chimica Acta* 1039 (2018) 1-23
- [303] M. Farmahini-Farahani, A.V. Saveliev, W. Merchan-Merchan, Volumetric flame synthesis of mixed tungsten-molybdenum oxide nanostructures, *Proceed. Combust. Institute* 36 (2017) 1055-1063.

## **APPENDIX**

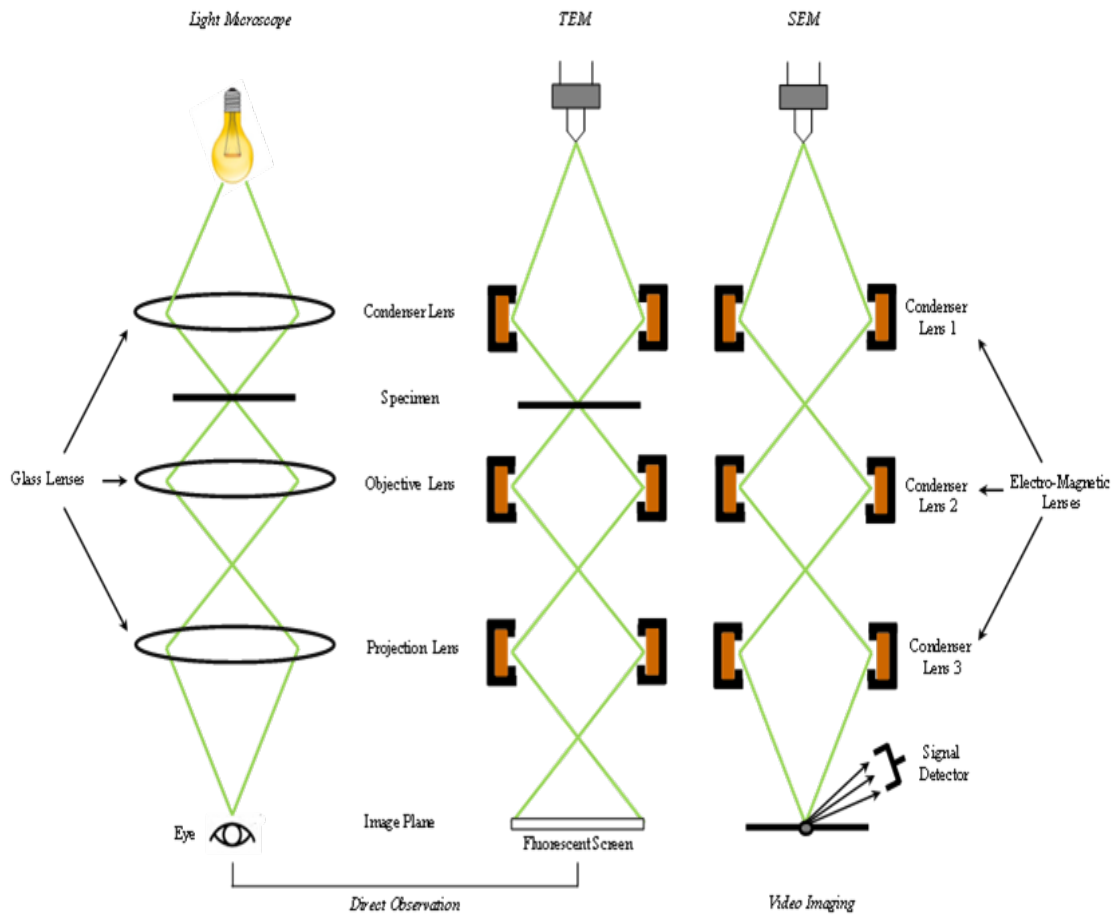
### **Appendix A – Structural and Chemical Characterization of Synthesized Nanostructures by Various Techniques**

#### **A.1 Electron Microscopy**

Electron microscopy is a crucial tool in nanotechnology research. Light microscopes are limited to 2000x magnification; but on the other hand, electronic microscopes can achieve magnifications of up to 2,000,000x. The electron microscopes employ a particle beam of electrons to illuminate the specimen and create a magnified image of it. Electron microscopes have greater resolution than optical microscopes owing to the fact that it utilizes electrons with wavelengths about 100,000 times shorter than photons (visible light), which is why the electron microscopes can achieve much higher magnifications. Table 9 shows a comparison between the light and electron microscopes

Apart from the difference in image producing techniques, the concepts remain the same for both microscope types. Whereas light microscopes use optical lenses to focus the photonic light, electron microscopes employ electro-magnetic lenses to manipulate the electron beam. There are two types of electron microscopes that provide different imaging analyses, TEM and SEM.

**Table 9.** Comparison of light vs. electron microscopes. Adopted from [232]



Light source

Glass lenses

Image formed by transmitted light

Fixed focal length

Light wavefronts move in a straight line

Light bends due to diffraction

2000x of magnification

Electron Source

Electro-magnetic lenses

Image formed by electrons impinging on a phosphor coated screen or by a camera

Variable focal length by varying current through lens

Electrons move in helical orbits

Electrons bend due to magnetic field

2000000x of magnification

## A.2 Transmission Electron Microscopy (TEM)

TEM is a microscopy technique that operates on the same basis as light microscopes but employs electrons rather than light. The fact that TEM employs electrons which have much lower wavelength than light makes possible to get resolutions with light microscopes. The possibility of high magnification imaging has made of this microscopy technique a valuable tool in various scientific research areas such as medical, biological, materials and nanotechnology.

In a TEM a source of electron at the top of the microscope emits the electron that travels through the column of the scopes under vacuum conditions. As it can be observed from **Table 9**, TEM employs electro-magnetic lenses in order to focus the electrons into very narrow beam. The electron beam passes through the specimen that is studied. Depending upon the material density of the specimen, some electrons are scattered and disappear from the beam. A fluorescent screen is positioned at the bottom of the microscope, which is hit by the remaining or unscattered electrons in the beam. This generates a shadow 2-D image of the specimen with all its parts shown in different darkness agreeing with their density [232].

The detailed structural characteristics of the synthesized nanostructures in this investigation were studied employing HR-TEM techniques with a JEOL TEM-3010 electron microscope. The magnification ranges from 50 to  $1.5 \times 10^6$  times. Images were collected on a Gatan digital imaging system and processed by Digital Micrograph software.

In order to gain further insight in the structural and elemental composition of the grown structures, EDX and SAED analyses were performed. It is important to mention that TEM has the potential to perform these analyses. SAED patterns are of excellent

indicators of the crystallographic state of the structures, giving detailed information about the crystalline or amorphous nature of the synthesized materials.

Another remarkable technique that can be applied using TEM is EDX, an analytical method employed to study the elemental or chemical composition of a sample. EDX detector can be attached to both TEM and SEM but in this investigation all the EDX analyses were performed by a TEM. The detectors capture the X-rays emitted from the specimen due to the high energy interaction between the electron beam and the sample. Individual elements in the periodic table have unique atomic structures and generate X-rays particularly of that unique material.

As it was mentioned above, EDX is an analytical technique therefore it has some limitations. Though this technique can provide information of the elements present in the specimen, it cannot precise the specimen's exact chemical composition. Consequently, it is recommended to use this technique in combination with others such as HR-TEM, XRD, XPS, etc. to fully characterize the chemical composition of the formed nanostructures.

### **A.3 Scanning Electron Microscopy (SEM)**

Similar to TEM, SEM employs electrons rather than light to produce an image. SEM generates 3-D appearances that are useful to study the surface structure of any specimen. It has a large depth of field, which allows a large amount of sample to be focus. These electronic microscopes yield high resolution images allowing the examination of closely spaced features at high magnifications. Combination of characteristics such as higher magnifications, large depth of focus, greater resolution, and ease of sample observation make this technique one of the most heavily utilized instruments in today remarkable areas. This microscopy technique provides important information regarding the actual synthesis

of structures on the probe surface exposed to the opposed-flow flame described herein. In this research, SEM essentially indicates whether or not the structures were formed on the surface of the metal probes and also provides information about the nature and morphology of the synthesized materials.

#### **A.4 X-ray Photo-Electron Spectroscopy (XPS)**

In order to characterize the elemental composition of the large cylindrical and polygonal 3-D structures in section 3.2, XPS techniques were employed. TEM analyses were not used considering the large micron-size of these structures.

XPS is a quantitative spectroscopic tool that provides detailed information about the elemental composition, empirical formula, chemical state, and electronic state of the elements that the sample possesses. X-rays irradiates the sample in order to obtain the XPS spectra, the kinetic energy and the number of electrons that scape from the top 1 – 10 nm of the specimen being analyzed are simultaneously measured. Ultrahigh vacuum is required in order to perform this analysis.

#### **A.5 Selected Area Electron Diffraction (SAED)**

SAED is a crystallographic technique performed in employing a TEM device to evaluate crystals orientation, assess the lattices constants, and also important the assessment of atomic defects. This technique is widely employed in material science research since the interpretation of the attained diffraction pattern serves as a source for identifying crystal structures, along with crystal's orientations and defects. In cases where the SAED is taken from a few or a single crystal, the pattern depicted consist of regularly distributed bright spots in a 2D projection of reciprocal crystal lattice, hence allowing the

pattern to be used to determine lattice constants (i.e. angles and distance between crystallographic planes). In other cases where the area selected for evaluation involves many crystallinities of different orientations (i.e. polycrystalline specimens), this results in multiple diffractions patterns being superimposed yielding an image of concentric rings. The diameter of each ring can be used to provide statistical information regarding the overall crystallinity.

## Appendix B – Curriculum Vitae

[wcuelloj@gmail.com](mailto:wcuelloj@gmail.com)

### **EDUCATION:**

#### **University of Oklahoma – Norman, OK**

- PhD in Mechanical Engineering, May 2023
- Coursework: Thermodynamics & Combustion, Combustion Engineering, Introduction to Health Monitoring
- Research: Combustion synthesis of transition metal oxide heterostructures
- Major GPA: 4.0/4.0

#### **University of Oklahoma – Norman, OK**

- Master of Science in Mechanical Engineering, Dec 2010
- Coursework: Combustion Processes II, Finite Element Methods, Transition Electron Microscopy, Guided Individual Studies, Introduction to Natural Gas Engineering, Aero-propulsion Systems, Nanocomposites, Air Conditioning Systems, and Principles of Heat Transfer.
- Research: Combustion synthesis of transition metal oxide nanostructures.
- Major GPA: 4.0/4.0

#### **Universidad Industrial de Santander (UIS) – Bucaramanga, Colombia**

- Bachelor of Science in Mechanical Engineering, Jun 2009
- Electives Coursework: Industrial Automation, Computer Numerical Control, Vibration Systems, Maintenance, and Oleo-Pneumatic Systems.
- Senior Thesis: Diffusion flame synthesis of iron and nickel oxide nanostructures.
- Overall GPA: 4.15/5.0

#### **Texas A&M University – Halliburton Executive Development Program**

- Business Leadership Development Program – Level II, Feb 2022
- Business Leadership Development Program – Level I, Apr 2016
- Financial Leadership for Non-Financial Managers, May 2014

#### **American Society of Mechanical Engineers (ASME)**

- PD442 - BPV Code, Section VIII, Division 1: Design and Fabrication of Pressure Vessels, Oct 2012

#### **Halliburton University and Related Training**

- Advance Business Acquisition Process – May 24, 2019
- WellLife Software
- DeepWater for Engineers, Jul 28-Aug 8, 2014
- Fiber Optics for Oil and Gas Applications – The Light Brigade, Jul 17-19, 2012
- iCem Service Cementing Simulation, May 21-25, 2012
- Corporate Story Telling Workshop – Articulus, Dec 1, 2011



- ANSYS Mechanical Non-Linear Structural Simulation – DRD Technology, Oct 20-21, 2011
- Introduction to ANSYS Mechanical and Design Modeler – DRD Technology, Oct 18-19, 2011
- Acoustic Emission for Scientist and Engineers – MISTRAS, Sept 20-22, 2011
- Cementing for Engineers, Jul 22, 2011
- Cementing I, Jun 30, 2011
- Casing and Cementing, Jun 18, 2011
- Red Book Assessment, Jun 18, 2011
- SolidWorks Essentials, Jun 23, 2011
- Fundamentals for Cementing Laboratory Technicians, May 20, 2011
- LabView Core 1 and 2 – National Instrument, Mar 23-25, 2011
- Oil Field Math, Feb 17, 2011

#### **John Zink Institute**

- Process Burner Theory, Sept 2010
- Process Burner Fundamentals, Sept 2010

#### **EXPERIENCE:**

##### **Halliburton Energy Services – Cementing, Jan 2022–Present    Houston, TX**

###### *Product Champion*

###### Agile Product Development

- AI/ML solutions
- CFD modeling
- Downhole hydraulics
- Product business cases
- Marketing/pricing strategy

##### **Halliburton Energy Services – Cementing, Feb 2020–Dec 2021    Adelaide, Australia**

###### *Pr. Technical Professional & Account Rep*

###### Cementing Engineer & BD Focal Point

- South Australia oil and gas wells
- Northern Territory ERD/unconventional gas wells
- SA clients’ pursuit and tendering initiatives for new work
- West Australia land gas wells
- Revenue and inventory forecast/execution management
- Power BI developer of South Australia Cementing BD and Operational dashboards

###### Major Achievements

- Employee of the month: Australasia Business Development on Aug 21. Collaboration and execution (Santos NT ERD)
- Employee of the month: Australasia CMT PSL on Mar-21. First ever WellLock Circ. Squeeze (WellSafe CO2/Gas remediation)
- CMT focal point for tailoring/execution of deepest ERD Gas Well development for Santos NT – Tanumbirini 2H
- Execution of >110 cement jobs, >56 wells, >17,150 bbl cement pumped for Beach Energy in SA

**Halliburton Energy Services – Cementing, Aug 2016–Feb 2020 Al-Khobar, KSA**

*Sr. Technical Professional*

Cementing Engineer Focal Point

- Integrated Projects (LSTK)
- ERD Wells (>4.3 MD/TVD)
- Bahrain Cementing Operations

Cement Engineer

- Offshore – Oil Wells
- Land operations – Exploration Wells Technology Development Applied to KSA
- High temperature epoxy resins
- Self-healing and flexible cement for casing-in-casing annular pressure prevention/mitigation
- Low-solids-shear dependable cement for lost circulation applications
- Evaluation of multi-morphology LCM for losses applications
- MENA Life of the well modeling SME and trainer
- Development of resin/cement composites for primary cementing applications - annular pressure prevention/mitigation

Major Achievements

- Tailored and designed longest 9-5/8” production ERD casing string in KSA (>20,000 ft MD & >4,500 ft TVD)
- Characterized Low Silica Spacer for KSA
- Advance BAP training

**Halliburton Energy Services – Cementing, Aug 2013–Aug 2016 Houston, TX**

*Sr. Technical Professional – Petro-Physical Applications*

Project Related Activities

- Project Leader – Low ECD Program: Determine engineering and chemical solutions to reduce overall ECDs for narrow margin, extended reach, slim holes and wellbore restrictions field cases
- Support the design of laboratory foam generator device
- Mechanical Properties SME
- Operational Support – First WellLife Job Brazil: Provided WellLife software support to the operations team in Brazil in order to evaluate the performance of conventional vs. elastic cements for the specific fields.
- Customer Support – WellLife Related: Provided support to internal and external customer regarding the capabilities of the software – Chevron & Total
- WellLife Training of MENA, USA, UK, and LA Field Personnel
- Project Lead – Verification plan of in-situ mechanical properties tester

Major Achievements

- Licensed Professional Engineer
- Phase I of Leadership Development Plan – Texas A&M University (Top Performer)
- Financial Leadership for Non-Financial Managers – Texas A&M University
- Completed Verification Plan of In-Situ Mechanical Properties Tester on time and within budget

**Halliburton Energy Services – Cementing, Jan 2011–Aug 2013 Houston, TX**

*Technical Professional – Petro-Physical Applications*

**Project Related Activities**

- Project Leader - Design and manufacturing of cement in-situ mechanical properties tester
- Project Leader - Design equipment and methodology for determining initial stress state of cement
- Project Leader - Design of cement-based systems with various acoustic properties for ultrasonic tools validation
- Provided 3D-modeling support for equipment employ to measure wettability of drilling fluids
- Performed destructive and non-destructive tests to determine mechanical properties of different cement systems
- CT-imaging characterization of cement and rock specimens
- Design and manufacturing of cement laboratory testing equipment

**Major Achievements**

- Out of scope challenge of designing 30'x30'x30' cement blocks with specific acoustic properties for validation/calibration of open hole acoustic tools
- Investigation of Resin-based centralizers bonded to steel pipe and stresses generated in the steel/resin interface as a result of temperature changes

**Combustion, Plasma and Nanoparticle Lab, Fall 2009-Fall 2010 Norman, OK**

*Graduate Research Assistant*

*Undergraduate Research Assistant (January 2008 – December 2008)*

- Research on combustion synthesis of transition metal oxides nanostructures

**School of Aerospace and Mechanical Engineering, Fall 2009 Norman, OK**

*Graduate Teaching Assistant*

- Design of Thermal-Fluid Systems

**Wellbore Stability Research Group (ICP-UIS), Dec 2006-Dec 2007 Bucaramanga, Colombia**

*Research Assistant*

- Developed a re-engineering process along with an adaptive design of a triaxial soil test equipment – Soiltest T-500A

**LEADERSHIP/PROFESSIONAL MEMBERSHIPS:**

- Member of TSPE (Texas Society of Professional Engineers)
- Member of ASME (American Society of Mechanical Engineers)
- Member of SPE (Society of Petroleum Engineers)
- Member of ACIEM (Society of Colombian Engineers)
- President of the Colombian OU Alumni Association (COUAA), Jan 2014 – Aug 2016

**SKILLS:**

- Oil Industry Software's Proficiency: iCem, WellLife, WellPlan and WellCat

- Bilingual: Spanish/English – Portuguese (Limited Working Proficiency)
- Skilled with: SolidWorks, Solid Edge, MS Visio, MS Office/Project.
- Familiar with: Labview, COSMOSWorks, Matlab, ANSYS.
- Power BI

**AWARDS AND HONORS:**

- Australasia employee of the month: CMT PSL on Mar-21 & BD on Aug-21
- Licensed Professional Engineer
- Pi Tau Sigma Member – International Mechanical Engineering Honor Society
- Promising Research Project, President for Research, Universidad Industrial de Santander (UIS), Spring 2009
- Outstanding Senior Thesis, Spring 2009

**PATENTS GRANTED:**

- US10890046B2 “Managed pressure reverse cementing”
- US10753176B2 “Swellable technology for downhole fluids detection”
- US 8794078 B2 “Cement Testing”
- US 8960013 B2 “Cement Testing”
- US 10241086 B2 “Validation of cased-hole acoustic tools”

**PATENTS FILED:**

- US 20150322328 A1 “Colloidal high aspect ratio nanosilica additives in sealants and methods relating thereto”
- US 20190024503 A1 “Ph-sensitive chemicals for downhole fluid sensing and communication with the surface”
- US 20180283165 A1 “Cementing Indication System”
- US 20180245427 A1 “Swellable technology for downhole fluids detection”
- US20190085654 A1 “Managed pressure reverse cementing”
- US20180238139 A1 “Systems and Method for Reverse Cementing”
- US20180363413 A1 “System and method for the detection and transmission of downhole fluid status”
- WO2018156123 A1 “Slurry design process”
- WO2019055043 A1 “Methods and systems for characterizing multiple properties of cement using p-waves of multiple frequencies”
- WO2018156122 A1 “Control heat of hydration by characterizing cementitious components”
- NO20181549 A1 “System and Method of producing foamed cement in a laboratory environment”
- WO2018156124 A1 “Reactivity mapping”

**JOURNAL PUBLICATIONS:**

- “Measuring and modeling cement hydration kinetics at variable temperature conditions” Pang, X., **Cuello Jimenez, W.**, Singh, J. Construction and Building Materials 262 (2020) 120788. **Impact Factor = 7.693.**

- “Evaluation of Epoxy Resin Thermal Degradation and its Effect on Preventing Sustained Casing Pressure in Oil and Gas Wells” Al-Yami, A., Wagle, V., **Cuello Jimenez, W.**, & Jones, P. Arab J Sci Eng (2019) 1-10. **Impact Factor = 2.621.**
- “Enhanced Mechanical-Integrity Characterization of Oilwell Annular Sealants Under In-Situ Downhole Conditions” **Cuello Jimenez, W.**, Darbe, R., Pang X., *SPE J.* 24 (2019) 2308–2319. **Impact Factor = 3.602.**
- “Characterizing gas bubble size distribution of laboratory foamed cement using X-ray micro-CT”, Xueyu Pang, John Singh, **W. Cuello Jimenez**, Construction and Building Materials 167 (2018) 243-252. **Impact Factor = 7.693.**
- “Isothermal Calorimetry Study of the Effect of Chloride Accelerators on the Hydration Kinetics of Oil Well Cement”, Pang, P. Boul, and **W. Cuello Jimenez**, Construction and Building Materials 77 (2015) 260-269. **Impact Factor = 7.693.**
- “Use of Microencapsulated Phase Change Materials to Regulate the Temperature of Oilwell Cement”, X. Pang, V. Goel, and **W. Cuello Jimenez**, SPE-171769, SPE Journal Paper 2014. **Impact Factor = 2.18.**
- “Nanosilicas as Accelerators in Oilwell Cementing at Low Temperatures”, X. Pang, P. Boul, and **W. Cuello Jimenez**, SPEDC 29 (2014) 98-105. **Impact Factor = 1.721.**
- “Hydration kinetics modeling of the effect of curing temperature and pressure on the heat evolution of oil well cement”, X. Pang, **W. Cuello Jimenez**, B. Iverson, Cement and Concrete Research 54 (2013) 69-76. **Impact Factor = 10.933.**
- “Flame synthesis of hybrid nanowires with carbon shells and tungsten oxide cores”, W. Merchan-Merchan, A.V. Saveliev, **W. Cuello Jimenez**, and Gautam Salkar, Carbon 48 (2010) 4510-4518. **Impact Factor = 11.31.**
- “Solid support flame synthesis of 1-D and 3-D tungsten oxide nanostructures”, W. Merchan-Merchan, A.V. Saveliev, and **W. Cuello Jimenez**, Proceedings of the Combustion Institute, 33 (2011) 1899-1908. **Impact Factor = 6.53.**
- “Combustion synthesis of carbon nanotubes and related nanostructures”, W. Merchan-Merchan, A.V. Saveliev, L. Kennedy and **W. Cuello Jimenez**, Progress in Energy and Combustion Science 36 (2010) 696-727. **Impact Factor = 35.34.**
- “Novel flame-gradient method for synthesis of metal-oxide channels, nanowires and nanorods” W. Merchan-Merchan, A.V. Saveliev, and **W. Cuello Jimenez**, Journal of Experimental Nanoscience 5 (2010) 199-212. **Impact Factor = 2.024.**

#### **BOOKS/ CONTRIBUTIONS THEREOF:**

- “Chapter 7 - Flame Synthesis of Nanostructured Transition Metal Oxides: Trends, Developments, and Recent Advances” W. Merchan-Merchan, **W. Cuello Jimenez**, O. Rodriguez Coria, C. Wallis. Editor(s): Y. Beeran Pottathara, S. Thomas, N. Kalarikkal, et al., In Micro and Nano Technologies, Nanomaterials Synthesis, Elsevier (2019) 201-263, ISBN 9780128157510

#### **CONFERENCE PUBLICATIONS:**

- “Thermal Degradation Kinetics of Epoxy Resins and Their Drilling Application.” Al-Yami, A., Wagle, V., **Cuello Jimenez, W.**, & Jones, P. (2018, November 12). Society of Petroleum Engineers. doi:10.2118/192863-MS

- “Thermo-Mechanical Properties of Annular Sealants—A Path to Optimized Wellbore Integrity and Economics” **Cuello Jimenez, W.**, Pang, X., Urdaneta, J. A., Sørensen, E., Lende, G., & Nimane, S. (2017, October 15). Society of Petroleum Engineers. doi:10.2118/187654-MS
- “Microscale Characterization of Field and Laboratory Foamed Cement by Use of X-Ray Microcomputed Tomography”, Pang, X., Maxson, J. K., **Cuello Jimenez, W.**, Singh, J. P., & Morgan, R. G. (2017, October 1). Society of Petroleum Engineers. doi:10.2118/180278-PA
- “Improving Wellbore Economics and Long Term Integrity by Optimizing the Design and Evaluation of Annular Sealants for Hydraulically Fractured Wells: A Case Study”, **Cuello Jimenez, W.**, Pereira, J., & Matzar, L. (2017, June 1). Society of Petroleum Engineers. doi:10.2118/188112-MS
- “Enhanced Mechanical Integrity Characterization of Oilwell Annular Sealants Under In-Situ Downhole Conditions: A Path to Optimized Wellbore Economics”, **Cuello Jimenez, W.**, Pang, X., Bengue, M., Darbe, R., & Meadows, D. L. (2017, April 4). Society of Petroleum Engineers. doi:10.2118/185341-MS
- “Influencing Factors of the Microstructure and Macroscopic Performance of Foamed Cement”, Pang, X., Singh, J. P., **Cuello Jimenez, W.**, & Prince, A. C. (2016, September 26). Society of Petroleum Engineers. doi:10.2118/181364-MS
- “Innovation of Annular Sealants During the Past Decades and Their Direct Relationship with On/Offshore Wellbore Economics”, **W. Cuello Jimenez, J. A.** Urdaneta, X. Pang, J.R. Garzon, G. Nucci, & H. Arias, (2016, April 20), Society of Petroleum Engineers. doi:10.2118/180041-MS
- “Engineered Oilwell-cement-based Systems for Optimum Validation of Cased-hole Ultrasonic Tools”, **W. Cuello Jimenez, X. pang,** and T. Gilstrap, SPE-168038-MS, IADC/SPE Drilling Conference and Exhibition, 4-6 March, Fort Worth, Texas, USA, 2014
- “Nanosilicas as Accelerators in Oilwell Cementing at Low Temperatures”, X. Pang, P. Boul, and **W. Cuello Jimenez**, SPE-168037-MS, IADC/SPE Drilling Conference and Exhibition, 4-6 March, Fort Worth, Texas, USA, 2014
- “Solid support flame synthesis of 1-D and 3-D tungsten oxide nanostructures”, W. Merchan-Merchan, A.V. Saveliev, and **W. Cuello Jimenez**, 33rd International Symposium on Combustion, August 1-6, 2010, Beijing, China
- “Counter-Flow Diffusion Flame Synthesis of Polygonal and Ribbons-Like Tungsten Oxide Nanostructures”, W. Merchan-Merchan, A.V. Saveliev, and **W. Cuello Jimenez**, 55th Annual Pentasectional Meeting of ACS, April 10- 2010, Norman, OK
- “Synthesis of 1-D and 3-D tungsten-oxide nanostructures on solid supports in an opposed flow oxy-fuel flame”, W. Merchan-Merchan, **W. Cuello Jimenez**, and A.V. Saveliev, CSCI 2010 Technical Meeting, March 21-23, 2010, Champaign, IL
- “Flame gradient synthesis of transition metal oxide nanostructures in an opposed flow methane oxy-flame” W. Merchan-Merchan, A.V. Saveliev, and **W. Cuello Jimenez**, 6th U.S. National Combustion Meeting, May 19-2009, Ann Arbor, Michigan